Magnetotransport in Graphene: Gap-Opening and Interaction Effects

THIS IS A TEMPORARY TITLE PAGE
It will be replaced for the final print by a version
provided by the service academique.

PhD thesis
at the faculty of science
in the doctoral program in physics
École Polytechnique Fédérale de Lausanne
presented by

Eva Peters

Max Planck Institute for Solid State Research, Heisenbergstr.1,
70569 Stuttgart, Germany
École Polytechnique Fédérale de Lausanne, Lausanne, Switzerland

Jury de Thèse:
Prof. Romuald Houdré, Jury president
Prof. Klaus Kern, Thesis director
Prof. Jürgen Brugger, Examiner
Dr. Pierangelo Gröning, Examiner
Dr. Jonathan Eroms, Examiner

Stuttgart, August 08, 2013

ECOLE DOCTORALE / DOCTORAL SCHOOL

PROGRAMME DOCTORAL EN PHYSIQUE / DOCTORAL PROGRAM IN PHYSICS

ECOLE POLYTECHNIQUE FÉDÉRALE DE LAUSANNE

Abstract

In this thesis, low temperature magnetotransport measurements are performed to explore the band gap opening and associated interaction effects in graphene. Being an ideally 2D material with carbon atoms hexagonally arranged in two sublattices, graphene comprises charge carriers that are chiral and mass-less, with the two Dirac cones of the valence and conduction band touching at the Dirac point. Owing to its extraordinary charge carrier mobility, superior to that of silicon, graphene is an emerging component of high speed electronic devices. However, as a semi-metal it does not allow for high on/off ratios and hence strategies to introduce a band gap in graphene are highly desirable.
We induce such a gap either in bilayer graphene by application of a vertical electric field, or in graphene antidot lattices (GALs) through spatial confinement associated with an interconnected array of narrow graphene stripes. While for bilayer graphene the gap size scales with the electric field, in case of the GALs the gap size is inversely proportional to the width of the constrictions. Toward gap tuning, we supply the bilayer flakes with bottom and top gates in order to achieve independent control over the carrier concentration and the electric field. In addition to the gap emerging above a certain vertical electrical field, also fingerprints of a spontaneous gap persisting down to zero electric and magnetic field are detected. For the GALs, the strength of spatial confinement was tuned by changing the distance between the nanoholes etched into the graphene sheet. Our data reveal that the charge transport is notably influenced by localized states, which are most likely located at the edges of the nanoholes. This leads to different types of variable range hopping (VRH), namely Efros-Shklovskii (ES VRH) and 2D Mott VRH, which govern the low magnetic field transport. Upon decreasing the nanohole distance, a strongly localized regime is entered, wherein Coulomb interactions between the localized states become increasingly important, as reflected by the emergence of a soft Coulomb gap. Concomitantly, the charge transport mechanism changes from ES VRH to 2D Mott VRH. Only under high magnetic fields the transport assumes the expected activated behavior, due to the emergence of a fundamental band gap. The size of this gap depends linearly on the strength of the applied B-field.

Besides the gap opening as such, the possibility to tune its size is equally important for the device implementation of graphene. While for the bilayer devices, such tuning is limited by the applied top and bottom gate voltages, which determine the electric field, the gap in the GALs is influenced not only by the nanohole spacing and the applied magnetic field, but also by the carrier concentration and the doping level.

Another important factor is the device quality, as quantified by the carrier mobility. Compared to graphene bilayers embedded into gate dielectrics, our freely suspended bilayer devices exhibit increased mobility, which in turn enhances the gap. Similarly, GALs of improved quality (achieved by suspension or thermal annealing) show enhanced Coulomb interactions along with stronger localization and a larger fundamental gap. In the quantum Hall regime, a complete degeneracy lifting of the zero-energy Landau level in both the bilayer and the monolayer devices is observed for high sample quality or strong enough

magnetic fields. By comparison, the additional application of a vertical electric field in the bilayer graphene devices leads to Landau level crossings and the emergence of a layer (valley)-polarized phase. For the GALs, evidence was gained that a band gap separates electrons and holes, corresponding to a valley-first splitting of the quasi-particles, in contrast to the behavior of non-structured graphene. Moreover, GALs of highest quality in addition display signatures of a small spin splitting on top of the valley splitting. Remarkably, the magnetic field dependence of the energy positions of the lowest Landau level in the GALs cannot be explained by a linear energy dispersion like in pristine graphene. Instead, the magneto-transport data is consistent with a parabolic dispersion in vicinity of the gap, while the linear dispersion prevails for higher energies.

Keywords: Graphene
Confinement
Graphene Bilayer
Electric and Magnetic Fields
Quantum Hall Effect
Band Gap
Variable Range Hopping

Zusammenfassung

In dieser Arbeit werden Magnetotransportmessungen bei tiefen Temperaturen durchgeführt, um die Öffnung einer Bandlücke und damit verbundene Wechselwirkungen in Graphen zu erforschen. Als ideales 2D Material, in welchem Kohlenstoffatome hexagonal in zwei Untergittern angeordnet sind, enthält Graphen chirale Ladungsträger, die zudem masselos sind. Die kegelförmigen Leitungs- und Valenzbänder im Graphen berühren sich am Ladungsneutralitäts- (bzw. Dirac-) Punkt. Besonders seine außerordentliche Ladungsträgerbeweglichkeit, welche die von Silizium bei weitem übertrifft, macht Graphen vielversprechend als Komponente von zukünftigen Hochfrequenz-Bauelementen. Als Halbmetall weist es jedoch eine nur geringe An/Aus-Schaltbarkeit auf, weshalb der Entwicklung von Strategien zur Bandlückenöffnung in Graphen große Bedeutung zukommt.
Wir induzieren eine solche Bandlücke sowohl in Doppellagen-Graphen durch Anlegen eines senkrechten elektrischen Feldes, als auch in Graphen-Antidotgittern durch laterale Einschränkung in Form von schmalen Graphenstreifen, welche in Form eines Gitters miteinander verbunden sind. Während die Bandlücke im Doppellagen-Graphen mit der Größe des angelegten elektrischen Feld zunimmt, ist sie in Antidotgittern umgekehrt proportional zur Breite der Streifen zwischen den Löchern mit Durchmessern im Nanometerbereich. Um die Größe der Bandlücke zu kontrollieren, statten wir das Doppellagen-Graphen mit einem darunter und einem darüberliegenden Gate aus, um die Ladungsträgerkonzentration und das vertikale elektrische Feld unabhängig voneinander kontrollieren zu können. Neben der Bandlückenöffnung oberhalb eines kritischen, vertikalen elektrischen Felds, ergaben sich Hinweise auf eine zusätzliche, spontane Bandlücke, welche auch ohne magnetisches und elektrisches Feld bestehen bleibt. In den Antidotgittern wurde das Ausmaß der lateralen Einschränkung über einen veränderlichen Abstand der ins Graphen geätzten Löcher variiert. Unsere Messungen ergaben, dass der Ladungsträgertransport deutlich von lokalisierten Zuständen, welche sich vermutlich an den Rändern der Löcher befinden, beeinflusst wird. Dies führt zu zwei unterschiedlichen Arten von „variable-range hopping"(VRH), nämlich Efros-Shklovskii (ES)-VRH oder 2D Mott VRH, welche den Ladungsträgertransport bei niedrigen Magnetfeldstärken bestimmen. Bei Verringerung des Abstands der Graphenlöcher erfolgt ein Übertritt in ein Regime starker Lokalisierung, in welchem die Coulomb-Wechselwirkungen zwischen den lokalisierten Zuständen verstärkt sind, was zum Auftreten einer weichen Coulomb-Lücke führt. Zugleich ändert sich der Ladungsträgertransportmechanismus von ES VRH zu 2D Mott VRH. Nur unter hohen Magnetfeldern zeigt sich das erwartete Temperaturverhalten für aktivierten Ladungsträgertransport aufgrund der sich öffnenden fundamentalen Bandlücke. Für die Größe dieser Lücke stellte sich heraus, dass sie linear mit dem angelegten Magnetfeld zunimmt.

Neben der Bandlückenöffnung als solche, ist die Möglichkeit deren Größe zu kontrollieren von ebenso großer Bedeutung für die Realisierung der viel versprechenden Anwendungen von Graphen. Während die Bandlücke im Doppellagen-Graphen durch die Gate-Spannungen, welche das elektrische Feld bestimmen, kontrolliert werden konnte, erwies sich die Bandlücke in den Antidotgittern als abhängig nicht nur vom Lochabstand sowie einem

von außen angelegten Magnetfeld, sondern auch von der Ladungsträgerkonzentration und der Dotierung.

Ein weiterer, wichtiger Parameter ist die Probenqualität, welche durch die Ladungsträgerbeweglichkeit angezeigt wird. Im Vergleich zu in Gate-Dielektrika eingebetteten Graphen-Dopellagen zeigen die untersuchten freistehenden Doppellagen eine höhere Ladungsträgerbeweglichkeit, und somit auch eine größere Bandlücke. Ähnlich hierzu weisen Antidotgitter von erhöhter Qualität (erreichbar durch Freilegung oder Ausheizen der Flocke) verstärkte Coulomb-Wechselwirkungen, sowie eine stärkere Lokalisierung und eine Zunahme der Bandlücke auf. Im Quanten Hall-Regime konnte sowohl für Graphen-Doppellagen, als auch Graphen-Monolagen ausreichender Qualität, eine vollständige Aufhebung der Entartung des niedrigsten Landau-Niveaus unter ausreichend hohen Magnetfeldern beobachtet werden. Demgegenüber führt das Anlegen eines vertikalen elektrischen Feldes in den Graphen-Doppellagen zum Kreuzen der Landau-Niveaus sowie zum Auftreten einer Lagen (Pseudospin)-polarisierten Phase. In den Antidotgittern kommt es im Gegensatz zu unstrukturiertem Graphen zu einer Trennung der Elektronen und Löcher durch die Bandlückenöffnung, wodurch die Pseudospin-Entartung der Quasiteilchen aufgehoben wird. Zudem weisen Proben höchster Qualität Anzeichen einer schwächer ausgeprägten Aufhebung der Spin-Entartung zusätzlich zur Pseudospin-Entartung auf. Es ist ferner bemerkenswert, dass die Magnetfeldabhängigkeit der Energie des aufgespaltenen niedrigsten Landau-Niveaus nicht durch eine lineare Dispersion, wie sie in unstrukturierten Graphen-Monolagen vorliegt, erklärt werden kann. Stattdessen deuten die Magnetotransport-Daten auf eine parabolische Dispersion in der Nähe der Lücke hin, während die lineare Dispersion für höhere Energien bestehen bleibt.

Stichwörter: Graphen
Laterale Einschränkung
Graphen Doppellagen
Elektrische und Magnetische Felder
Quanten Hall Effekt
Variable Range Hopping
Bandlücke

Contents

Chapter 1

Introduction

At the beginning of the 20th century, new physical theories had to be developed since it became clear that the laws of the classical mechanics and electrodynamics are not sufficient to explain phenomena occurring when

(i) the physical dimensions approach atomic length scales

or

(ii) the speed of light is approached.

Stimulated by M. Planck, who proposed the quantization of electromagnetic energy when studying black body radiation in 1900 [1], quantum mechanics emerged as a new theory. This theory of light quanta - which later became known as photons - was further advanced by A. Einstein in his work on the photoelectric effect in 1905. In the same year he also published other works including one on special relativity [2], thus reconciling electrodynamics and classical mechanics by extending it to the speed of light limit. The concept of quantization was then used by N. Bohr to predict orbital radii and light emission spectra of hydrogen in 1913 [3]. In 1924, the particle-wave dualism was introduced by L. de Broglie [4]. Subsequently, the theoretical basis of the laws of quantum mechanics was formulated by a matrix description by W. Heisenberg 1925 [5], and the alternative wave mechanics by E. Schrödinger 1926 and P.A.M. Dirac [6], the latter of whom formulated the relativistic equation of motion for the electron wavefunction. These theories provided the basis for the subsequent experimental research into these phenomena, either by going to high energies or smaller and smaller dimensions. After the fabrication of the first transistor by W.B. Shockley, J. Bardeen and W.H. Brattain in 1947 [7], improved fabrication techniques in semiconductor physics such as molecular beam epitaxy (MBE) [8] and lithography techniques provided access to highly crystalline, defect-free and small structures. These experimental activities were aided by the development of novel technologies in vacuum- and low-temperature science and led to the discovery of novel quantum phenomena, like the quantum Hall effect (QHE) by K. v. Klitzing in 1980 [9, 10]. These new theories and technological advances did not only radically change our understanding of the physical world, but also have an impact on our modern daily life, as exemplified by the development of integrated circuits and fast electronics.

Graphene is a highly intriguing material which has been studied by theory since 1947 [11]. This interest arises since graphene represents an ultimately thin, truly 2D layer, and at the same time possesses quasi-particles that behave in a relativistic manner. Thus, it combines both aforementioned aspects that are incompatible with classical mechanics and electrodynamics. Furthermore, graphene represents the basic building block of other carbon allotropes. Although it is likely to have been encountered already in the stone age in the form of char coal drawings on cave walls, and even today it is (unwittingly) manipulated by every school child using a pencil, graphene has not been experimentally studied until 2004 [12–14]. Following the vast research conducted in the decades before on the other carbon allotropes such as fullerenes [15] and carbon nanotubes [16], the most recently discovered graphene received even greater attention in the scientific world. This is largely due to the fact that it suddenly became possible to study quantum electrodynamics in a condensed matter system experimentally, a task which previously had been restricted to high energy physics. Thus new phenomena could be expected and for instance the QHE in graphene indeed turned out be special compared to conventional 2DEGs. This difference arises from the unique mass-less character of graphene's quasi-particles, which is imparted by its linear low-energy dispersion. Moreover, due to its hexagonal lattice structure composed of two sublattices whose carbon atoms are non-equivalent, graphene mono- and bilayers exhibit, besides the spin degree of freedom (an angular momentum associated with elementary or quasi-particles, being a pure quantum-mechanical phenomenon), also a pseudo-spin (valley) degree of freedom, which can alternatively be described as so-called chirality [17] of the quasi-particles. The resulting Landau level (LL) structure comprises a unique zero-energy level equally shared between electron and holes, as well as a shift of the LL structure compared to the usually observed one, giving rise to the so-called half-integer QHE. Owing to the special nature of its quasi-particles and its extremely high carrier mobility which depends only weakly on temperature, the QHE in graphene can be observed even at room temperature, much higher than the previous temperatures below $\approx 30\ K$ [18]. The very high carrier mobility of graphene (intrinsic mobility $\mu \approx 200,000\ cm^2(Vs)^{-1}$ at room temperature [19]) compared to silicon ($\mu \approx 15,000\ cm^2(Vs)^{-1}$ at room temperature) renders it not only interesting for fundamental research in physics, but also opens new application perspectives for high speed electronics. However, to reach this challenging goal three major obstacles have to be overcome, specifically:

(1) introduction of a band gap in the semi-metal graphene, which is required for effective
current switching in field-effect devices;
(2) development of large-scale, low-cost production methods;
(3) achievement of high carrier mobility after device fabrication, which typically introduces a significant amount of contamination.

One major focus of the present thesis is to explore the introduction of a band gap in graphene or its bilayer, the possibility of tuning the gap, and the influence of improved carrier mobility. In addition, novel phenomena such as interaction effects of the involved quasi-particles in such devices are addressed. The topic of graphene devices obtainable by

large-scale production methods will be touched upon in the outlook section in the form of graphene on SiC. With the exception of this part, this thesis deals with micrometer-scale graphene structures obtained by mechanical exfoliation, which most reliably yields sheets of high carrier mobility. In order to improve the quality of the devices, the sheets are freely suspended and/or thermally annealed. The experimental studies of the gap opening characteristics of graphene involve two model systems, namely bilayer graphene (subjected to a vertical electric field) and graphene antidot lattices (GALs).

The first possibility to introduce a band gap in graphene, investigated in this thesis, is to apply an electric potential difference between the two layers in bilayer graphene [20]. This potential difference induces a band gap whose magnitude depends on the vertical electric field strength. By suspending the flake between a top and bottom gate, we are able to tune the electric field and carrier concentration in the sheet independently. Compared to graphene bilayers embedded into bottom and top gate dielectrics [21], the present suspended bilayers exhibit higher carrier mobility and accordingly larger gap sizes [22]. We are also able to fabricate high quality multi-terminal suspended devices, for which a complete splitting of the quasi-particle degrees of freedom can be observed already at low external magnetic fields. We show that the vertical electric field also influences the Landau level structure, leading to Landau level crossings. Furthermore, at low electric and magnetic fields, an unexpected spontaneous gap opening, which manifests itself by an increased resistance, is detected.

For the GALs, theory predicts a fundamental band gap that scales inversely with the neck width between the nanoholes [23], akin to graphene nanoribbons [24]. While experimental studies have provided hints for the opening of a band gap in GALs with neck widths of the order of 20 nm [25], a systematic understanding of the connection between their electronic structure and the geometry of the antidot lattice has not yet been attained. Moreover, a direct proof for the presence of a fundamental band gap in such samples has remained elusive so far. We demonstrate that the electronic transport in our GAL structures is governed by the presence of localized states within a transport gap. The interactions between these states lead to a soft Coulomb gap and associated Efros-Shklovskii variable range hopping (ES-VRH) in case of small nanohole spacing, whereas 2D Mott VRH emerges for larger nanohole spacing. In the former case, ES VRH is preserved upon application of magnetic fields of up to 1 Tesla, above which a transition to Mott VRH occurs due to decreased Coulomb interaction between the localized states which leads to weaker localization. At intermediate magnetic fields, the hopping exponent assumes a value of 2/3, which had previously been obscured by the dominance of Mott VRH. The crossover between the hopping regimes can alternatively be induced at zero magnetic field by increasing the gate-controlled carrier concentration. We observe stronger localization and an enhanced gap also for suspended or annealed GALs, in which furthermore interference effects become observable as a consequence of the improved quality and larger phase coherence lengths. At elevated magnetic fields, we observe a transition from hopping conduction to activated transport due to the presence of a band gap under these conditions, which in turn can be traced back to a small zero-field gap. In addition, we find that the gap formation is associated with a splitting of electrons and holes in the lowest LL, which in a simple par-

ticle picture corresponds to valley-first polarization. Hall bar measurements under high magnetic fields furthermore indicate that the gap-opening by the spatial confinement is accompanied by a band structure modification, involving the transformation from linear to parabolic dispersion in the vicinity of the gap, while the higher LLs remain unaffected.

The fundamental physics underlying the magnetotransport phenomena, which is essential for understanding the experimental results in this thesis, is described in **chapter 2**. This chapter also gives an overview of graphene's peculiar band structure, complemented by the basics of low temperature charge transport under applied magnetic field in general and specifically for mono- and bilayer graphene. Details on the sample fabrication and contact configuration of the investigated devices are provided in **chapter 3**. Here, also technical details about the ^3He-system that has been set up in the framework of this research are given. The possibility to rotate the sample in an external magnetic field enables to differentiate between effects depending on the total magnetic field vs. the out- or in plane B-field component. This is exploited to identify the origin of interaction effects. The integration of a confocal microscopy setup into a cryostat system, furthermore, enables scanning photocurrent microscopy (SPCM) measurements which can provide valuable information about contact effects, potential distributions and Landau levels in graphene devices. First SPCM test measurements on GAL devices are described in the outlook. The effect of a vertical electric field on multi-terminal bilayer graphene devices is the topic of **chapter 4**. **Chapter 5** deals with the gap opening induced by spatial confinement in the GALs, and the magnetotransport properties of GALs of different geometries. On this basis, a detailed understanding of the relationship between the electronic structure and geometry of the GALs is developed. The effect of an applied magnetic field provides a more complete picture of the hopping conduction regimes in the GALs, as discussed in **chapter 6**. Evidence for the presence of a fundamental band gap, which is associated with valley splitting and a transformation to a parabolic dispersion in the GALs, is given in **chapter 7**. Finally, **chapter 8** summarizes the obtained results and major conclusions, and provides an outlook on future possible directions, such as gap opening by hydrogenation of epitaxial graphene on SiC, or measurements using low temperature SPCM. Moreover, first promising results on the magnetic properties of hydrogenated epitaxial graphene are presented.

Chapter 2

Electronic Properties of Graphene in Magnetic Fields

The electronic properties of graphene are remarkable in many respects [26–28]. One example is the anomalous Landau level sequence of the QHE, which is a direct consequence of the graphene lattice. Owing to the mass-less, chiral Dirac fermions, the quantum Hall effect in graphene displays a shift of the Hall resistance by a half-integer compared to the conventional integer QHE [29, 30]. This anomalous QHE arises from a Landau level at zero-energy which is shared equally between electrons and holes [31]. The peculiar lattice structure of graphene renders its charge carriers chiral [17] and the carriers possess a pseudospin that is directly related to the two different sublattices A and B which correspond to valleys K and K' at the Brillouin zone boundary, where the valence and conduction band meet. Here, the dispersion relation is linear instead of parabolic as in conventional semiconductor two-dimensional electron gases (2DEGs). In contrast to conventional semiconductors, the QHE in graphene is measurable up to room temperature [18] since the edge modes are topologically protected. The charge carrier mobility is only weakly dependent on temperature, and extremely high intrinsic mobilities have been reported [19].
A short introduction to graphene and its experimental discovery is given in section 2.1. Section 2.2 deals with the magnetotransport properties in conventional semiconductor 2DEGs such as the integer quantum Hall effect, including the influence of disorder and broadening as well as the edge channel picture. The band structure of graphene along with the implications for its quasi-particles is discussed in section 2.3. The band structure also has direct consequences for the LL spectrum, which is described in section 2.4 for monolayer and bilayer graphene.

2.1 Introduction

Graphene consists of a honeycomb lattice of carbon atoms. It is a purely two-dimensional material, were the sp^2-bonds between the carbon atoms [11] are responsible for the high mechanical strength of the sheet. The binding between different graphene layers, in mul-

tilayer graphene or graphite is much weaker, since it is mostly due to van der Waals interactions. The π-conjugate system, constituted by the carbon p_z-orbitals, is responsible for electrical conductivity of the graphene layer. Since it can be seen as the basic building block for other carbon allotropes such as fullerenes [15], carbon nanotubes [16], or graphite, its band structure has been intensively studied theoretically [32–36]. Tight binding calculation of graphene's band structure reveals an unusual semi-metallic behavior with a linear dispersion around the meeting points of the conduction and valance band. Here, the charge carriers are mass-less and mimic relativistic particles, such as photons. This makes it possible to study quantum electrodynamics in a solid state material. However, until 2004 [12, 13], studies of graphene were limited to theoretical work. Indeed, since purely two-dimensional crystals are predicted to be thermodynamically unstable [37], graphene was for a long time thought not to exist in a freestanding form. Monolayer graphene proved to be stable even without the support of a substrate due to the formation of ripples and corrugations [38]. Furthermore, the visualization and identification of monolayer graphene was a major hurdle for its discovery, since as a single atom-thick layer it is transparent for visible light. This problem can be overcome by exploiting interference effects by depositing graphene on a Si substrate with a SiO_2 layer of suitable thickness (300 nm). The optical path contributed by the graphene layer changes the interference color, which can be detected by an optical microscope [39].

2.2 Low Temperature Magnetotransport in 2D Electron Gases

2.2.1 Quantum Hall Effect

If a magnetic field B is applied perpendicular to a two-dimensional electron gas (2DEG), the Lorentz force acts on the charge carriers perpendicular to their direction of motion. This results in charge accumulation at the edges of the electron gas, perpendicular to the current direction. Under equilibrium, the electric field due to the accumulated charges exactly balances the Lorentz force, which results in the Hall resistance $R_{xy} = B/en$ (with electron density n and electron charge e) that depends linearly on the magnetic field. Figure 2.1(a) shows the contact configuration for measuring the Hall resistance with a magnetic field applied to the sample in z-direction, while a current is passed from one main contact (1) to the adjacent contact (4). For a 2DEG patterned in Hall bar geometry, the Hall voltage V_{xy} is measured between two adjacent Hall probe contacts, for instance (3) and (5). The longitudinal voltage V_{xx} is measured between two neighboring contacts in x-direction, e.g. (2) and (3).
While the Hall effect can be explained semi-classically, the Quantum Hall effect can only be explained by quantization of the charge carrier energy into so-called Landau levels. For a conventional 2DEG the energy of the electrons

$$E = \frac{\hbar^2}{2em_{eff}}(k_x^2 + k_y^2) \tag{2.1}$$

is continuous with a parabolic dispersion if no magnetic field is applied. Here, $k_{x,y}$ are the wavenumbers in reciprocal space and m_{eff} is the effective electron mass under the influence of the lattice. In an applied magnetic field, discrete energy levels of equal spacing are formed. They can be derived from the Schrödinger equation as

$$E_N = (N + \frac{1}{2})\hbar\omega_c, \;\; N = 0, 1, 2, ... \tag{2.2}$$

where $\omega_c = eB/m_{eff}$ is the cyclotron frequency and N the Landau level index. Here, the spin degree of freedom has been neglected.

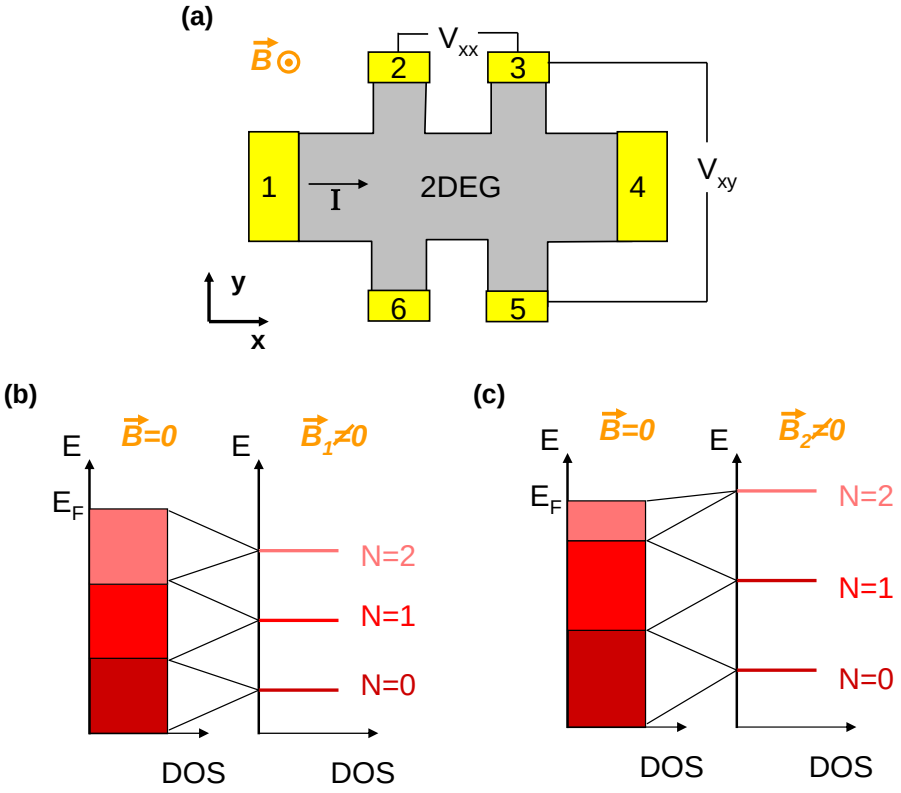

Figure 2.1: Quantum Hall effect in a classical 2DEG. (a) 2DEG in form of a Hall bar with an applied current I and measurement of the longitudinal V_{xx} and Hall voltage V_{xy} in applied magnetic field $\vec{B}$. (b) Landau level quantization with three LLs completely filled at a magnetic field B_1.(c) Landau level quantization with the third LL only half filled at $B_2 > B_1$.

Each LL can accommodate a certain number of states and, hence, possesses a degeneracy, which increases with magnetic field $n_L = eB/h$, with $\Phi_0 = h/e$ the magnetic flux quantum. The filling factor

$$\nu = \frac{n}{n_L} = \frac{nh}{eB} \tag{2.3}$$

assumes integer values and denotes the number of filled LLs ($\nu = 1, 2, 3...$). The energy quantization, correspondingly leads to a quantized Hall resistance

$$R_{xy} = \frac{h}{\nu e^2}. \tag{2.4}$$

The condensation of the density of states into LLs is illustrated in figure 2.1(b) and (c) for two different magnetic fields $B_2 > B_1$. Without magnetic field the energy distribution is continuous and the density of states (DOS) is constant up to the Fermi energy E_F. In an applied magnetic field all states condense into discrete LLs. In a situation, where the LLs are filled completely, as depicted in figure 2.1(b) for three filled LLs, the Hall resistance assumes the quantized value. Since the electrons move in cyclotron orbits, the longitudinal resistance is zero. Upon increasing the magnetic field, the highest occupied LL is depopulated since the LL degeneracy increases with field. This situation is shown in figure 2.1(c), where the third LL is only half filled. In this case, charge transport in the longitudinal direction can occur, and the Hall resistance jumps to the next plateau. In real samples, however, extended regions of zero longitudinal resistance are observed [40,41]. To understand this behavior, it is necessary to take disorder and defects into account.

2.2.2 Disorder and Broadening

Disorder and defects in the sample lead to spatial potential fluctuations, which broadens the LLs in non-ideal samples, as shown in figure 2.2(a).

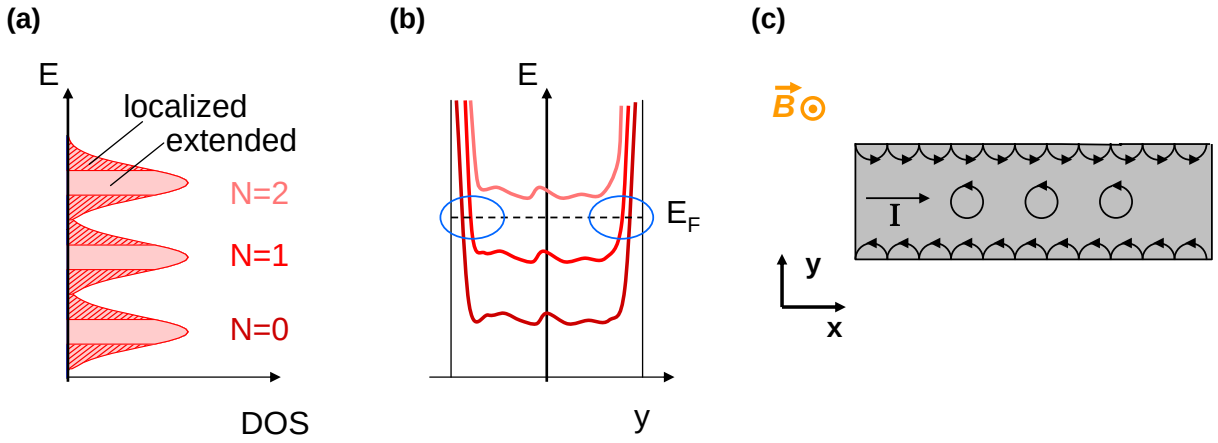

Figure 2.2: Broadening and potential distribution for non-ideal 2DEGs. (a) Broadening of the LLs due to scattering generates extended and localized states. (b) Energy profile due to disorder and finite width in y-direction, resulting in edge channel conduction. (c) Electron transport in the edge channel picture.

The states can be distinguished into extended states at the LL centers and localized states in the LL tails. As the localized states do not contribute to the conduction the resistance

remains constant. Only when the Fermi energy enters the region of the extended states, the Hall resistance changes and the longitudinal resistance becomes finite. The energy profiles along the y-direction of the sample in figure 2.2(b) reveals that the energy fluctuates around the LL energies. The LL energies are bent upwards at the edges of the 2DEG. Intersection of the Fermi energy with the LLs leads to 1D edge channels at the edges of the 2DEG (regions indicated by blue circles) [42]. In this edge channel picture, the electrons are reflected elastically at the edges, and forced to move along the original direction of motion by the magnetic field [43]. At the opposite edge, the electrons are forced to move in reverse direction, while electrons circling in the bulk are not available for conduction. The electrons in the edge channel move quasi-ballistically since back-scattering is suppressed, with each channel contributing one conductance quantum e^2/h to the conduction.

2.2.3 Potential Distribution and Edge State Transport

If the Fermi level is located between two LLs (i.e. within the localized states), only the edge channels contribute to carrier transport, which is quasi-ballistic. Decreasing or increasing the Fermi level to coincide with one of the LL energies, where extended states are present, induces bulk conduction with backscattering rendering the transport non-ballistic. These two cases are illustrated in figure 2.3.

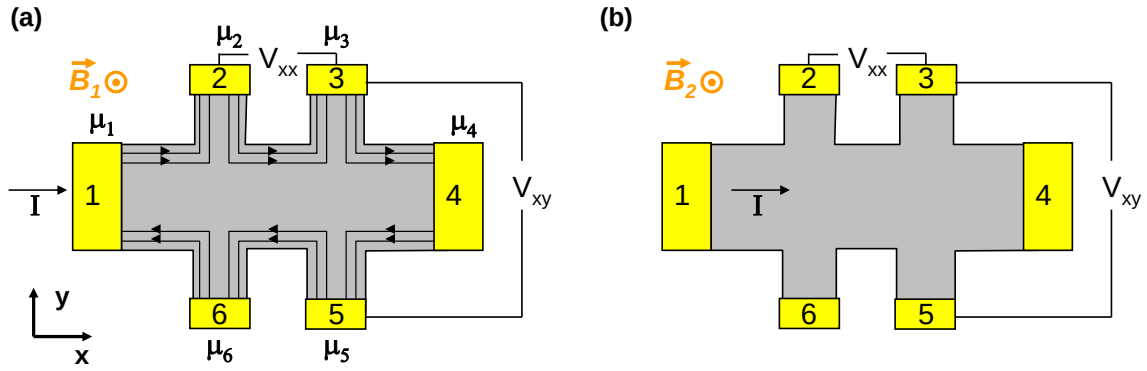

Figure 2.3: Conduction in the quantum Hall regime in a 2DEG Hall bar for two different magnetic fields ($B_1 \neq B_2$). (a) Conduction via edge channels (E_F between LLs). (b) Conduction via bulk transport (E_F in one of the LLs).

For the former case of edge channel conduction, the potential at each of the contacts μ_i ($i = 1 - 6$) can be used to derive the longitudinal and Hall resistances. For this purpose, ideal contacts and no reflection of charge carriers at the 2DEG/contact interfaces are assumed. Charge carriers injected through contact (1) with potential μ_1 move to contact (4) via (2) and (3). Since no current is extracted at contacts (2) and (3), the potential remains unchanged ($\mu_1 = \mu_2 = \mu_3$). The same holds for the other edge of the 2DEG ($\mu_4 = \mu_5 = \mu_6$). Thus, there is one high and one low potential edge of the 2DEG, and the

current is given by

$$I = \frac{e}{h}\nu(\mu_1 - \mu_4), \tag{2.5}$$

where ν is the filling factor, which corresponds to the number of edge channels. Since electrons injected via (1) do not reach (5) or (6), the longitudinal and Hall voltage assume values of

$$eV_{xx} = \mu_3 - \mu_2 = 0, \ and \ \ eV_{xy} = \mu_3 - \mu_5. \tag{2.6}$$

Hence, the corresponding resistances are

$$R_{xx} = 0, \ and \ R_{xy} = \frac{h}{e^2\nu}. \tag{2.7}$$

2.3 Quantum Electrodynamics in Carbon

Graphene consists of a two-dimensional hexagonal lattice of carbon atoms as shown in figure 2.4(a). The two sublattices consisting of atoms A and B can be distinguished. Figure 2.4(b) displays the band structure of graphene calculated by a nearest-neighbor tight-binding approach, which takes only the p_z orbitals that are responsible for the delocalized π-electron system into account. The hexagonal Brillouin zone possesses the high symmetry points Γ, M, K and K', where K and K' are inequivalent since they correspond to the two sublattices A and B. The dispersion relation is given by [33]

$$E(k_x, k_y) = \pm\gamma_0 \left(1 + 4cos\left(\frac{\sqrt{3}k_x a}{2}\right) cos\left(\frac{k_y a}{2}\right) + 4cos^2\left(\frac{k_y a}{2}\right)\right)^{1/2}. \tag{2.8}$$

Here, $\gamma_0 \approx 3.2\ eV$ is the nearest neighbor interaction. The carbon-carbon bond length of $a' = 1.42\ \mathring{A}$ determines the magnitude of the lattice vector $a = \sqrt{3}a'$. Since the valence and conduction bands form conically shaped valleys that meet at the K and K' points, graphene is a semi-metal and exhibits an ambipolar field effect. If the Fermi level lies below the Dirac point, the unoccupied states in the valence band can be described as positively charged holes that contribute to conduction. For undoped graphene, the Fermi level lies at $E = 0$ with a completely filled valence band and empty conduction band. The charge carrier concentration thus equals zero. Upon raising the Fermi energy, electrons in the conduction band become available for conduction (see figure 2.4(c)). In the vicinity of the K and K' points (displacement from the K and K' points in reciprocal space: $\delta\vec{k}$), the dispersion relation can be approximated as [44]

$$E(\delta\vec{k}) = \hbar\nu_F \left|\delta\vec{k}\right|, \tag{2.9}$$

with the Fermi velocity $\nu_F = \frac{\sqrt{3}\gamma_0 a}{2\hbar} \approx 10^6\ m/s$. The Fermi energy depends on the electron density n according to $E_F = \sqrt{\pi n}\hbar\nu_F$.The K and K' points are also called Dirac points since in the vicinity of these points, at low energies, the dispersion is linear rendering the

charge carriers mass-less. Due to the linear dispersion, all charge carriers below the Fermi energy have the same constant velocity in contrast to conventional semiconductors, where the parabolic dispersion causes a rapid carrier velocity decrease away from the band edge. The mass-less carriers in graphene are to be described by the 2D-Dirac equation instead of the Schrödinger equation.

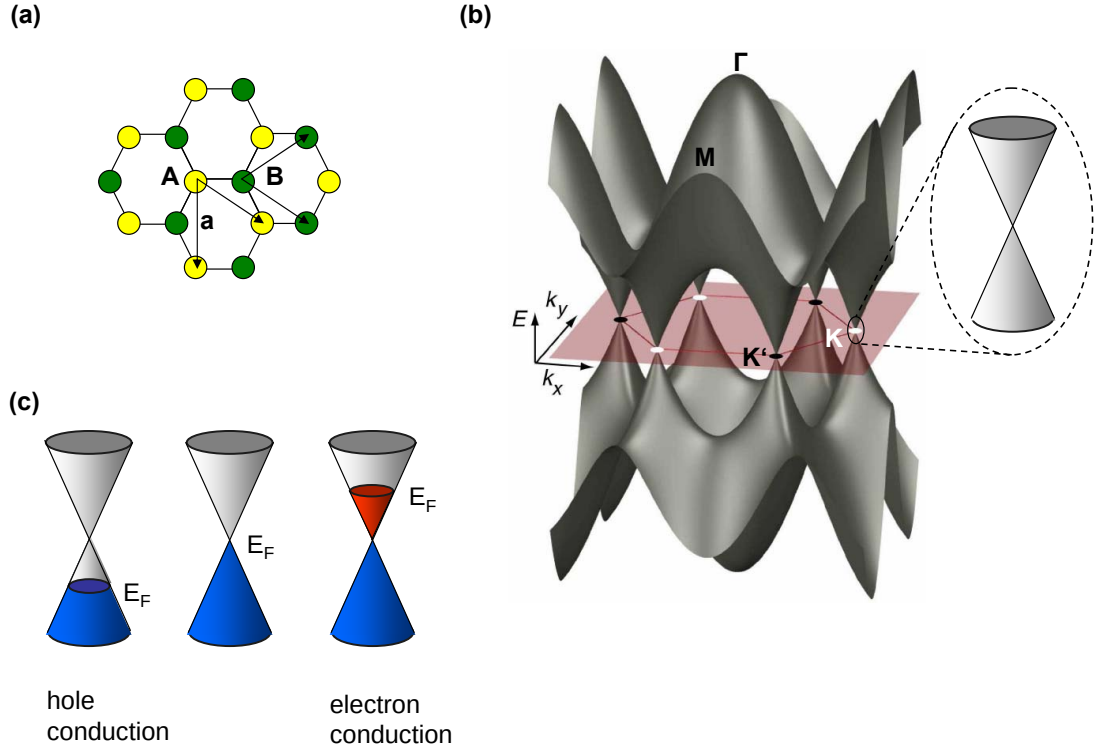

Figure 2.4: Electronic structure of monolayer graphene. (a) Hexagonal lattice with atoms A and B and lattice constant a. (b) Band structure derived from tight binding model with valleys K and K' (adapted from [44]). (b) Ambipolar conduction by electrons or holes, depending on the Fermi level position.

In the 2D-Dirac equation [32, 45]

$$\pm \nu_F \begin{pmatrix} 0 & p_x - ip_y \\ p_x + ip_y & 0 \end{pmatrix} \begin{pmatrix} \Psi_A(r) \\ \Psi_B(r) \end{pmatrix} = E \begin{pmatrix} \Psi_A(r) \\ \Psi_B(r) \end{pmatrix} \tag{2.10}$$

p is the momentum, while $\Psi_A(r)$ and $\Psi_B(r)$ represent the two different carrier wavefunctions on the the sublattices A and B. Thus, instead of using two separate Schrödinger equations for the two charge carrier types, as common practice for 2DEGs, the Dirac equation is used for the charge carriers with an additional degree of freedom. In particular, additionally to the spin, the carriers also posses a so-called valley or pseudo-spin degree of freedom (associated with the sublattices A and B). Within one band, corresponding to

one of the sublattices, the direction of motion for electrons (positive energy E) is opposite to the direction of motion for holes (negative energy $-E$). Since the pseudo-spin is the same for both carrier types in the band, it is parallel to the electron momentum and antiparallel to the hole momentum in the band. In the other band the opposite applies. Defining chirality [17] as the projection of the pseudo-spin onto the direction of motion of the charge carrier leads to electrons with positive and holes with negative chirality in the first energy band and vice versa in the other band.

2.4 Landau Level Structure in Monolayer and Bilayer Graphene

The Landau level spectrum of conventional 2DEGs, monolayer and bilayer graphene is compared in figure 2.5.

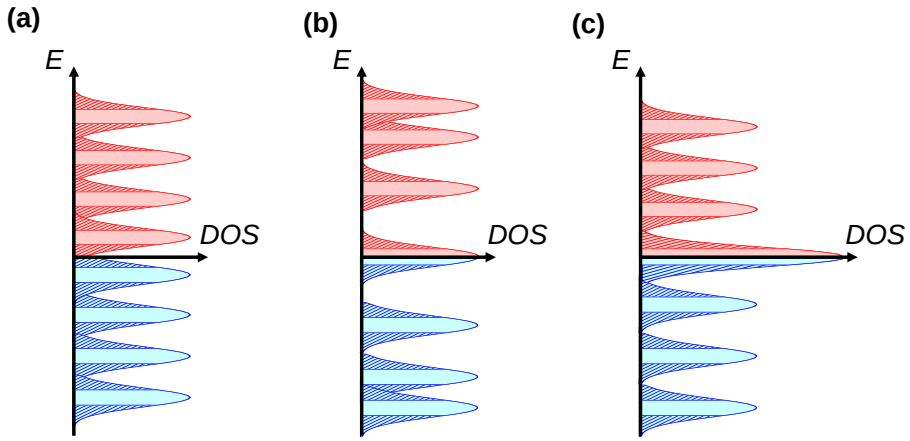

Figure 2.5: Comparison of the LL spectrum for different 2DEGs. Localized states are indicated by shaded regions, while extended states correspond to filled regions. (a) Equidistant LLs for conventional 2DEGs with separated electron (red) and hole (blue) levels. (b) For monolayer graphene the LL energy follows a square-root behavior. The zero-energy LL is equally shared between electrons and holes. (b) Bilayer graphene exhibits LLs of approximately equal spacing, similar to conventional semiconductors, but also the unusual zero-energy LL as in monolayer graphene.

For conventional semiconductor 2DEGs, separate electron and hole LL form, that are equally spaced. For monolayer graphene the LL energy follows a square-root behavior and a zero-energy level appears that is shared equally by electrons and holes. Such a level is also present in bilayer graphene, although a close to equidistant LL structure is present. The difference between the conventional LL structure and that in monolayer and bilayer graphene is a direct consequence of the chirality of the charge carriers. Carrier movement on cyclotron orbits in a magnetic field results in an accumulation of a phase shift - the

Berry's phase - of π for the wavefunction of the chiral mass-less quasi-particles in graphene, and 2π for the wavefunction of the chiral massive quasi-particles in bilayer graphene [30]. This explains the unusual LL at zero energy [46]. Furthermore, backscattering is suppressed for the chiral charge carriers [47], which leads to protected edge states and the possibility to observe the quantum Hall effect up to room temperature [18].

2.4.1 Monolayer Graphene

As shown above, the charge carriers in graphene can be described by the 2D-Dirac equation (equation 2.10). In an applied magnetic field the resulting Landau level energies are given by

$$E_N = sgn(N)\sqrt{2e\hbar\nu_F^2 B\,|N|}, \tag{2.11}$$

with the LL index $N = \pm 0, \pm 1, \pm 2, ...$ The sign of N refers to the charge carrier type and is positive for electrons and negative for holes. As a direct consequence of the pseudospin degree of freedom, a zero-energy LL emerges, which is equally shared between electrons and holes of opposite pseudospin. Thus, while in the conventional quantum Hall effect the Hall conductivity is quantized to values of $\sigma_{xy} = \nu\frac{e^2}{h}$ with $\nu = 1, 2, ...,$ the plateaus in graphene are shifted by 1/2:

$$\sigma_{xy} = \nu\frac{e^2}{h};\ \nu = \pm\xi\left(N + \frac{1}{2}\right) = \pm 2, \pm 6, \pm 10, ... \tag{2.12}$$

with LL index $N = 0, 1, 2...,$ and ξ accounting for the valley and spin degeneracy of the charge carriers ($\xi = 4$ in monolayer graphene). This is the reason why the quantum Hall effect in graphene is also called the half-integer quantum Hall effect, with the first σ_{xy} plateau already appearing when the zeroth energy level is half filled with electrons or holes. From equation 2.11 it is apparent that in contrast to conventional 2DEGs, the energy spacing of the LLs is not equidistant due to the linear bandstructure.

2.4.2 Bilayer Graphene

In contrast to monolayer graphene, in bilayer graphene with so-called Bernal (AB) stacking, the dispersion relation is parabolic at the meeting points of the valence and conduction band. Thus, the charge carriers are no longer mass-less but possesses a finite mass of $m \approx 0.05 m_e$, with the electron mass m_e and the Landau level energy given by

$$E_N = \pm\hbar\omega_c\sqrt{N\,(N-1)}, \tag{2.13}$$

with LL index $N = 0, 1, 2...,$ and the cyclotron frequency $\omega_c = eB/m$. The Hall conductivity exhibits plateaus at

$$\sigma_{xy} = \nu\frac{e^2}{h};\ \nu = \pm\xi N = \pm 4, \pm 8, \pm 12, ... \tag{2.14}$$

The charge carriers in bilayer graphene possess spin and valley degeneracy which leads to a 4-fold degeneracy of each LL ($\xi = 4$) except for the lowest LL. The zero energy LL $E_{0,1}$ with LL indices $N = 0$ and 1 exhibits an additional degeneracy due to the orbital degree of freedom and is thus 8-fold degenerate.

Chapter 3

Magnetotransport and Confocal Microscopy

As seen in the previous chapter 2, the features of the QHE are characteristic for the investigated system. For graphene, it does not only provide unequivocal prove of the number of layers but also provides information about the sample doping and shape, as well as interaction effects of the quasi-particles present. The QHE is commonly investigated in Hall bar geometry which allows to determine both longitudinal and transverse conductivities. For simplicity other geometries like lateral two- or four-terminal or van-der-Pauw geometries can be applied. Sample fabrication (section 3.1) and device aspects such as mobility, cleaning and different device geometries (section 3.2) are discussed in this chapter. Besides Hall bar and lateral contact configuration, another useful geometry, especially with regard to the edge modes, is the Corbino geometry, which contains no edges at all. Charge transport data gained with such structures are presented in section 3.2.
For combined low temperature magnetotransport and scanning confocal microscopy a ^3He-system is built up. It comprises a transport insert with a rotatable sample holder and an insert with a fiber-based confocal system mounted on a piezo-positioner and scanner stack. The setup is described in section 3.3.
To establish the function, hold time and base temperature of the rotator insert, monolayer graphene Hall bar devices are used for low temperature angle-dependent measurements. The performance of the confocal microscopy (CFM) insert, including the spatial resolution, hold time and base temperature under scanning and laser illumination, is tested with a modified marker substrate, specifically designed for a search-and-find routine for the navigation between individual nanostructures at fixed, defined positions on a macroscopic chip.

3.1 Sample Fabrication

Depending on the type of device, the fabrication process includes exfoliation, identification and contacting of graphene bi- or mono-layers, followed by etching of a desired structure

or pattern into the flake and finally suspension with subsequent current annealing or the structuring of additional air bridge contacts.

Exfoliation and Contacting

In graphene research different methods are pursued to optimize sample production in terms of quality, scalability and reliability. Besides mechanical exfoliation [12, 13], these methods range from chemical exfoliation [48, 49], chemical vapor deposition (CVD) [50–54] to epitaxially grown graphene on SiC [55–57]. Most of these methods, however, have the disadvantage of notably reducing charge carrier mobility. This is partially due to more complicated processing or additional fabrication steps such as the transfer onto the desired substrate in case of CVD graphene on copper or nickel foils [53, 54]. For epitaxial graphene on SiC further treatment is necessary. Here the substrate is conductive if doped, which is advantageous for scanning tunneling microscopy (STM) or angle-resolved photoemission spectroscopy (ARPES). For magnetotransport measurements, decoupling from the substrate and further modification such as the addition of gate dielectrics and gates for charge carrier modulation are necessary. Thus far the most successful and also simplest way to produce isolated graphene layers of high quality is mechanical exfoliation. This method is used for the samples in chapters 3-7, whereas in chapter 8 also epitaxially grown graphene on SiC is investigated and will be discussed more closely there.
Mechanical exfoliation of graphene onto silicon substrates covered with 300 nm of thermally grown SiO_2 layer is carried out similar to literature [12, 13]. Starting from a crystal of highly ordered pyrolytic graphite (HOPG), by repetitiously pealing using Scotch tape, thin graphite layers are gained that stick to the tape. Alternatively, Kish-graphite or natural graphite may be used for this purpose. The graphite layers can then be transferred from the tape to a substrate. To improve the yield of monolayers, the substrate is heated to 160°C and subsequently cooled down to about 50°C just before exfoliation. Graphene is then deposited onto the substrate by gently pressing the Scotch tape onto the substrate. In general, the deposition temperature determines the deposition yield and can be adjusted as desired.
After exfoliation onto a Si/SiO_2 substrate, monolayer-, bilayer- and multilayer graphene flakes are located and distinguished by optical microscopy. Although it is only one layer thick, interference effects make monolayer graphene visible on a 300 nm thick SiO_2 surface [39]. Flakes with different numbers of layers can be distinguished by their gray scale contrast with respect to the bare substrate. The layer number and doping can be further confirmed by Raman spectroscopy [58–61] or magnetotransport measurements.
In order to improve their quality, the samples can be annealed under argon at 250°C. Although this improves the flake quality through the removal of adsorbates and contaminants, the latter are, however, again introduced when the sample is exposed to atmospheric conditions as well as PMMA resist in the following processing steps. This exposure to the ambient is avoided if the sample is annealed under vacuum, when already mounted in the transport setup.
For charge transport measurements, electrical contacts are defined on the selected sheets

via standard e-beam lithography (EBL). This technique makes use of a positive polymer resist, specifically a double layer of poly(methyl methacrylate) (PMMA) ($\approx 200\ nm$), which is spin-coated onto the sample and exposed in the EBL step. Subsequent development in a $1:3$ mixture of methyl isobutyl ketone (MIBK) and isopropanol (IPA) dissolves the exposed parts of the PMMA. The process is stopped by immersing the substrate in pure IPA. Subsequently, thermal evaporation of the contact metals (Ti/Au or Cr/Au) is performed in vacuum ($p \approx 1 \cdot 10^{-6}\ mbar$). Subsequent lift-off in N-methylpyrrolidone (NMP), removes the resist in the non-exposed areas together with the metal film on top. The result is a graphene field-effect transistor with ambipolar transfer characteristic (figure 3.1).

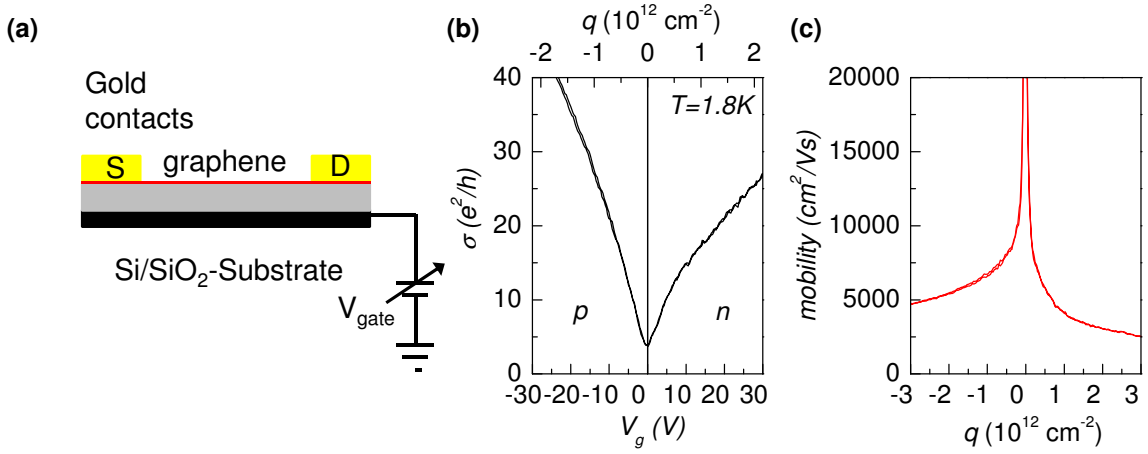

Figure 3.1: Monolayer graphene FET (sample 8855_D2a).(a) Schematic of the device configuration. The carrier density is induced via the field-effect by an applied back gate voltage. (b) Gate sweep characteristic with hole conduction for negative voltages and electron conduction for positive voltages. (c) Dependence of mobility on carrier concentration. The high concentration mobility is about $5,000\ cm^2(Vs)^{-1}$.

The charge carrier density is induced by a gate voltage $V_g = V_{gate} - V_{CNP}$ and, in a simple capacitor model, is given by:

$$q = \alpha V_g, \tag{3.1}$$

with gate coupling factor α:

$$\alpha = \frac{\epsilon_0 \epsilon_r}{ed}. \tag{3.2}$$

Here, the V_{CNP} is the CNP position of the flake, which is usually shifted to positive gate voltages V_{gate} due to unintentional doping of the device. For a $d = 300\ nm\ SiO_2$ gate dielectric with a permittivity of $\epsilon_r = 3.9$, $\alpha \approx 7 \cdot 10^{14}\ m^{-2}V^{-1}$, such that concentrations of up to $q \approx 1 \cdot 10^{17}\ m^{-2}$ can be induced before the break down of the gate dielectric.
For increasing gate voltage (positive or negative), either electrons or holes contribute to the conduction, which results in typical resistances on the order of 1 $k\Omega$ depending on the contacts and the device dimensions. Upon decreasing the charge carrier densities the

resistance increases and directly at zero carrier density, at the charge neutrality point (CNP), infinite resistance would be expected. In reality, however, only the total charge carrier density is exactly zero at the CNP since electron and hole puddles [62] are still present and hence the resistance remains finite. Experimentally, a resistivity of $\approx h/4e^2$ [29] has been found which deviates from the theoretical predicted value of $h\pi/4e^2$ [63–65] by the factor of π. Due to residues of the e-beam resist and other contaminants the CNP of the devices is usually not located at zero back gate voltage, but shifted to positive gate voltages. The carrier mobility is accessible from the gate dependent resistivity ρ and the electron n or hole p concentration by applying the semi-classical Drude model via

$$\mu_{n,p} = \frac{1}{(n,p)e\rho}, \tag{3.3}$$

where the resistivity depends on the flake length l and width w: $\rho = Rl/w$. Due to the failure of the Drude model near the CNP, the mobility cannot be reliably determined from equation 3.3 for low carrier concentration ($\mu \to \infty$ for $n, p \to 0$). Instead, it is usually calculated for the large carrier concentration range, where $n, p \cong 2 \cdot 10^{16}\ m^{-2}$, or derived from the conductivity σ: $\mu_{n,p} = \frac{1}{e}\frac{d\sigma}{d(n,p)}$.
After glueing the sample into a chip carrier and bonding of the bond pads to the chip carrier contacts, the devices can optionally be annealed under argon at $\approx 120°C$ in order to remove doping by adsorbed water molecules. A better method, however, is to anneal the sample in the measurement setup since in this case exposure to the atmosphere can be avoided (see chapter 5).

Reactive Ion Etching (RIE)

For structuring the graphene flakes into Hall bar structures, Corbino disks or antidot lattices, reactive ion etching (RIE) in combination with a PMMA mask pre-structured via EBL is used. The PMMA etch mask is obtained via EBL as described above. Here, a single thin layer PMMA ($\approx 50\ nm$) and an increased acceleration voltage ($30\ kV$) are used to minimize proximity effects and help to pattern small features ($\leq 30\ nm$). To avoid overheating and hardening of the resist, a low plasma power in the RIE step is necessary. In general, 46 $Watt$ at 0.05 $mbar$ with 100 $sccm$ Ar and 11 $sccm$ O_2 for 5 s is sufficient to etch exposed monolayer and bilayer graphene completely. The process is completed by dissolving the resist like in the lift-off process with NMP, acetone and IPA.

Suspension and Current Annealing

One efficient way to improve the sample quality of micrometer-size graphene sheets is to render them freely suspended [66]. This is achievable by partial etching of the underlying SiO_2 dielectric, such that the impact of surface roughness of the SiO_2 or trapped charges between the surface and the flake is avoided [67,68].
For the suspension the device is contacted as described above and subsequently etched in buffered oxide etch (BOE). A 5 : 1 aqueous dilution etches 150 nm SiO_2 in $\approx 90\ s$

at room temperature. Since the etching occurs faster for areas which are not covered by metal contacts, the SiO_2 underneath the graphene is fully etched while the contacts remain supported by a SiO_2 column if they are broad enough. To ensure a good stability of the structures, a contact thickness of $\geq 100\ nm$ and Cr as adhesion layer metal is required. The etching is stopped with methanol and the sample is dried in a critical point drier using methanol, acetone or IPA. This step is critical to prevent the sheet from attaching to the back gate.

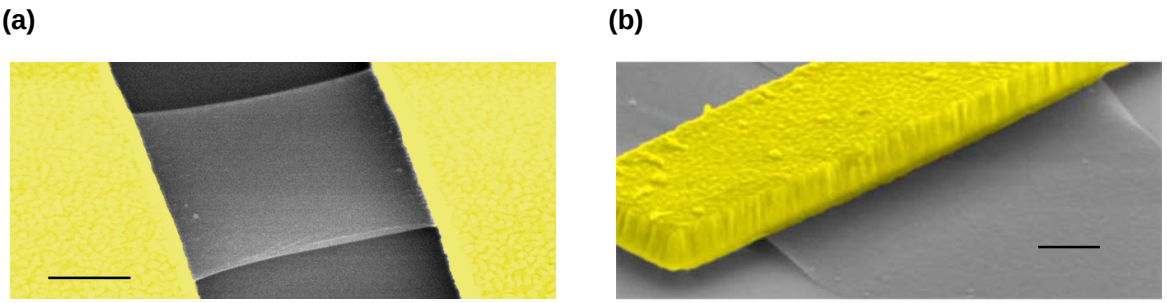

Figure 3.2: SEM images of suspended graphene. The scale bar is 400 nm and the gold contacts are colorized yellow. (a) Suspended monolayer graphene between two gold contacts (Inlens detector). (b) The suspended bilayer is pinned to the contacts and falls onto the substrate unless there is a second nearby contact to hold it up (SE2 detector).

Figure 3.2(a) displays a suspended device supported by gold contacts. The zoom of figure 3.2(b) highlights the attachment of the graphene flake in the contact region. On the contact side where there is no close-by neighboring contact, the flake falls down on the substrate. The distance between two neighboring contacts can be maximally a few micrometers for suspending the flake in between and maintaining a good mechanical stability of the device. The gate coupling to the back gate can be estimated by the simple capacitor model with capacitors in series:

$$\frac{1}{\alpha} = \frac{1}{\alpha_1} + \frac{1}{\alpha_2} = \frac{e}{\epsilon_0}\left(\frac{d_1}{\epsilon_{r1}} + \frac{d_2}{\epsilon_{r2}}\right) \tag{3.4}$$

with $d_1 = d - a$ and $d_2 = a$, where d is the original gate dielectric thickness and a the thickness of the air layer from the substrate to the flake. With the permittivity of air being close to the vacuum permittivity ($\epsilon_{r2} \approx 1$) and $\epsilon_{r1} = 3.9$ the gate dielectric of SiO_2, the gate coupling factor for the back gate is around $2.9 \cdot 10^{14}\ m^{-2}V^{-1}$. However, the concentration range is limited, since for gate voltages $V \geq 10\ V$ ($q \approx 3.5 \cdot 10^{15} m^{-2}$) the flake bends towards the gate due to electrostatic attraction, which can lead to the flake sticking to the back or top gate, rendering the device useless. Similarly to non-suspended devices, the CNP of as-fabricated suspended graphene devices is commonly located at positive gate voltages, and lies outside the accessible gate voltage range if the doping is too strong. Thus, the charge carrier density is to be calculated as $q = \alpha(V_{gate} - V_{CNP})$ with $V_g = V_{gate} - V_{CNP}$. Nonetheless, current annealing [69], a cleaning method especially

useful for suspended samples, can be used to shift the CNP close to zero back gate voltage and to improve the device quality substantially. For this purpose, a large current is passed through the device to induce Joule heating, which similarly to thermal annealing removes adsorbates [69, 70]. Figure 3.3(a) shows the effect of current annealing for a monolayer graphene flake at $T = 40\ K$. The initial decrease in resistance upon ramping the bias voltage can be ascribed to temperature effects. Around $I_{sd} \approx 0.3 - 0.5\ mA$ the resistance increases slightly since the CNP is shifted toward zero. When the bias is ramped back to zero, the low-bias resistance has significantly increased compared to the initial value.

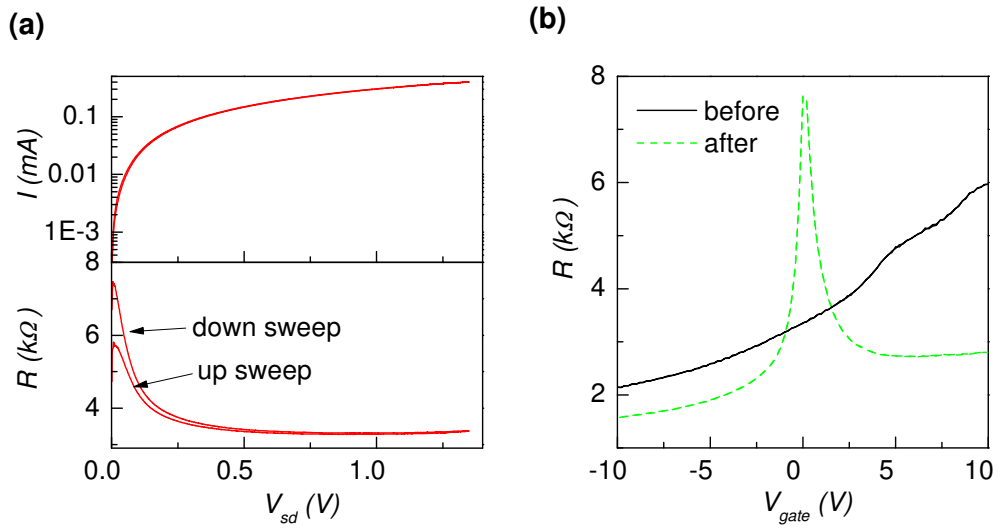

Figure 3.3: Current annealing procedure for a suspended monolayer graphene device. (a) Resistance and current of sample 9139_*D2b* during the up and down ramping of the bias voltage. (b) Gate sweeps before and after annealing of the sample in panel (a).

Figure 3.3(b) compares gate sweeps of the resistance at $T = 40\ K$ before and after current annealing. Before annealing the flake is highly doped. Only after current annealing, the CNP is located in the accessible gate voltage range. Furthermore, the mobility of the device has been improved, which manifests itself in a decreased width of the CNP-peak. While suspended graphene can exhibit mobilities up to $\mu \approx 200,000\ cm^2(Vs)^{-1}$ at low temperatures [66, 71], for graphene devices on Si/SiO_2 typical values of $\mu \approx 5,000 - 10,000\ cm^2(Vs)^{-1}$ have been found, limited due to scattering by charged impurities [72,73], substrate roughness [68, 74], SiO_2 surface optical phonons [75, 76] and substrate induced electron-hole puddles [62,67,77]. For graphene on hexagonal boron nitride (hBN) similar high mobilities as for suspended graphene have been reported [78, 79].

Air-bridge Contacts

One way of connecting a contact with its lead without a short-circuit to a second underlying contact is the structuring of air-bridge contacts [80–82]. These are especially relevant for

micrometer-scale Corbino structures where the inner contact, which is surrounded by an outer contact, is too small to be contacted via non-lithographic methods.

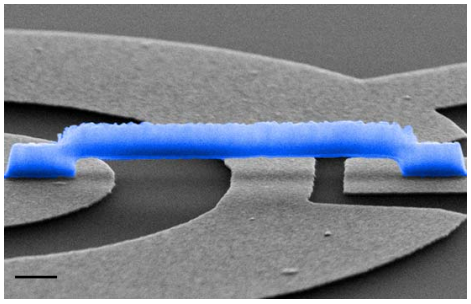

Figure 3.4: SEM image of an air-bridge (colorized blue) connecting two metal contacts without short-circuit to the third contact in between. The scale bar is 300 nm.

The electron micrograph in figure 3.4 depicts such an air-bridge which connects the two ends of the current leads by bridging a third contact. The air bridge can be defined in a single EBL step following the definition of the contacts as described above. To this end, a double layer PMMA and co-polymer P(MMA-MAA) resist system is used, which possess different sensitivity to e-beam exposure. A third layer of PMMA improves the undercut. For defining the bridge region, a low exposure dose is used, such that only the upper two resist layers are developed, while the bottom layer is not affected. A higher e-beam dose is used for the pillar regions (support posts of the bridge) to develop all of the resist layers. The distance of the bridge region to the substrate is controlled via the thickness of the first PMMA resist layer, which is ≈ 250 nm for the resist system used here. To ensure a good stability of the bridge 300 nm gold is used as bridge material. No adhesion layer is necessary, since the pillars of the bridge are defined directly on the pre-structured gold contacts.

3.2 Measurement Geometry

Contact Configuration

For electrical measurements the arrangement of the contacts on a graphene sheet with length l (measured between the two voltage probes) and width w determines which transport properties are directly accessible. Figure 3.5 illustrates different, commonly used device geometries. The current flowing from the source to the drain contact as well as the measured voltage is indicated. A two- or four-terminal lateral contact configuration (figure 3.5(a) and (b)), where the contacts are directly patterned in a single EBL step, is most straightforward and reliable, due to the low number of contacts and since no etching step is necessary. In contrast to the two-terminal configuration, a four-terminal measurement

eliminates contact resistance contributions. The resistivity ρ of the device

$$\rho = R\frac{w}{l} \tag{3.5}$$

can be directly calculated from the resistance as well as the conductivity, which is the inverse resistivity.

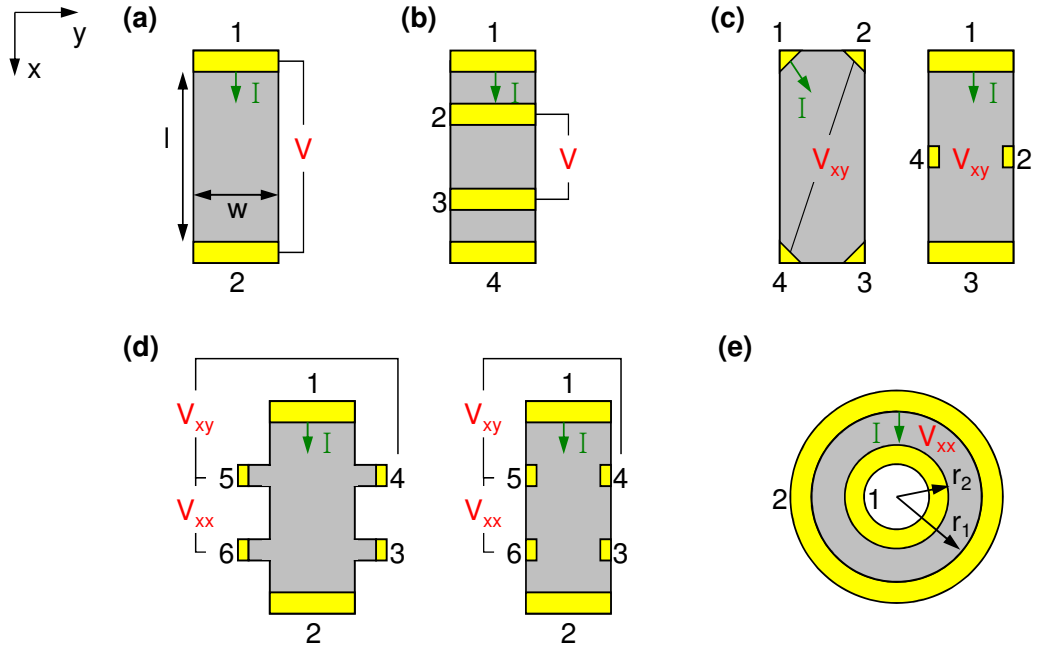

Figure 3.5: Different contact configurations for a graphene flake of width w and length l. (a) Lateral two-terminal contacts. (b) Lateral four-terminal contacts. (c) Van der Pauw geometry with either ideal contacts at the edges (left) or at the sides (right) of the flake. (d) Hall bar geometry ideally with an etched flake (left), or alternatively a non-etched flake (right). (e) Corbino geometry with inner radius r_2 and outer radius r_1 of the flake.

Another widely used contact configuration in graphene research is the van der Pauw geometry (figure 3.5(c)) [83,84], where two pairs of opposing contacts are placed on the sample corners. As an advantage over the lateral configuration, it enables measurement of the Hall resistance $R_{xy} = V_{xy}/I$. Since it is applicable to arbitrarily shaped samples, etching of the sample is avoided. For homogeneous samples, admixtures of the longitudinal voltage contributions due to non-ideal contact size or configuration, can be compensated by performing several measurements of the Hall resistance in different contact orientations. As one possibility, measurements with permuted voltage and current contacts are performed to measure the voltages: $V_{ij,kl}$ (voltage measurement between contact i and j with a current flowing from contact k to l with $V_{ij,kl} = -V_{ij,lk} = -V_{kl,ij}$). Alternatively, the magnetic field direction is reversed instead of the current direction. As the Hall voltage is antisymmetric in magnetic field, it changes its sign (but not the absolute value) upon reversal of

the magnetic field ($V_{ij,kl}(B) = -V_{ij,kl}(-B) = V_{kl,ij}(-B)$). The longitudinal resistance can be measured in a separate measurement by using adjacent contacts for the voltage and current probes, respectively. Similarly to the methods described above, admixtures of the Hall voltage can be minimized by a combination of several measurements of the longitudinal resistance. In contrast to the Hall voltage, the longitudinal voltage is symmetric in magnetic field and, hence, remains unchanged upon reversal of the magnetic field.

3.2.1 Graphene Hall bars

The ideal contact geometry for separate measurements of the longitudinal and transverse resistivity of a 2DEG as present in graphene is the Hall bar geometry (figure 3.5(d)). Here, two contacts serve as source and drain electrodes, while two pairs of adjacent or opposing contacts between them are used for the voltage measurements (V_{xx} and V_{xy}). In figure 3.6 a graphene Hall bar device is displayed.

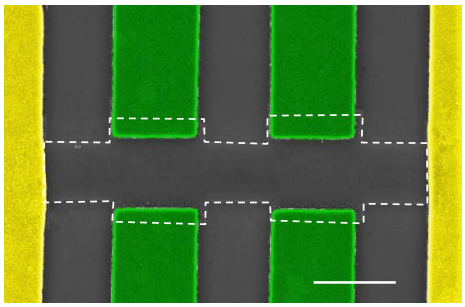

Figure 3.6: Scanning electron microscopy (SEM) images of a graphene Hall bar device. The scale bar is 1 μm and the current contacts are colorized yellow while the Hall probes are colorized green. The circumference of the graphene flake is indicated by the white dashed line.

The longitudinal ρ_{xx} and transverse ρ_{xy} resistivity are given by the following respective equations:

$$\rho_{xx} = R_{xx}\frac{w}{l},\ \rho_{xy} = -R_{xy}. \tag{3.6}$$

The corresponding conductivities are accessible via tensor inversion of the resistivity tensor $\boldsymbol{\rho}$. Applying the symmetry relations ($\rho_{xx} = \rho_{yy}$ and $\rho_{xy} = -\rho_{yx}$) valid for a uniform (isotropic) sample, the following relations for the respective conductivities are obtained:

$$\sigma_{xx} = \frac{\rho_{xx}}{\rho_{xx}^2 + \rho_{xy}^2},\ \sigma_{xy} = -\frac{\rho_{xy}}{\rho_{xx}^2 + \rho_{xy}^2}. \tag{3.7}$$

Figure 3.7(a) and (b) display the longitudinal and Hall resistance of a representative graphene Hall bar device (sample 10268_$D2$) at $T = 1.6\ K$ and magnetic fields $B = 12\ T$, $B = 6\ T$, $B = -12\ T$ and $B = -6\ T$. As already mentioned the Hall resistance changes its

sign but not its magnitude upon reversal of the magnetic field direction or carrier density (gate voltage), while the longitudinal resistance remains the same.

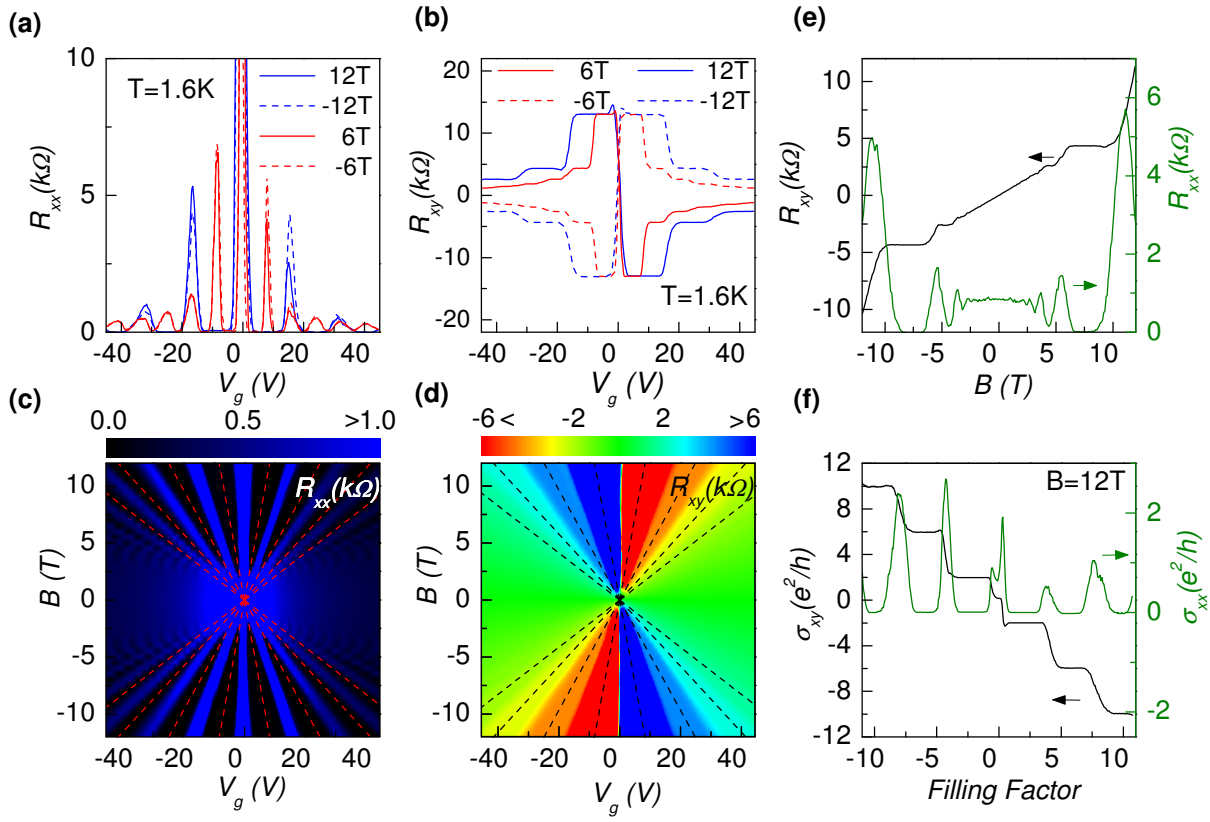

Figure 3.7: Longitudinal and transverse resistances and conductivities of the graphene Hall bar device 10268_D2 at $T = 1.6\ K$. (a) Longitudinal resistance at $B = 12\ T$, $B = 6\ T$, $B = -12\ T$ and $B = -12\ T$. (b) Hall resistance at $B = 12\ T$, $B = 6\ T$, $B = -12\ T$ and $B = -12\ T$. (c) Fan diagram of the longitudinal resistance. (d) Fan diagram of the Hall resistance. (e) Longitudinal and transverse resistances as a function of magnetic field at a carrier density of $q = -1.085 \cdot 10^{12}\ cm^{-2}$. (f) Longitudinal and transverse conductivities at $B = 12\ T$.

Corresponding fan diagrams of the resistances in panel (a) and (b) are given in figure 3.7(c) and (d), respectively, where the resistances are plotted as a function of both magnetic field and gate voltage. In these fan diagrams the B-field dependent filling factor positions are indicated by dashed red and black lines for filling factors up to $\nu = 14$. Shubnikov de Haas oscillations are observable in panel (e), where the resistances are plotted as a function of magnetic field at carrier density $q = -1.085 \cdot 10^{12}\ cm^{-2}$. The respective conductivities derived by the tensor inversion (equation 3.7) are shown in figure 3.7(f). Plateaus in the Hall conductivity, which are accompanied by zero longitudinal conductivity, occur at the usual graphene filling factors $\nu = \pm 2, \pm 6, ...$

3.2.2 Graphene Corbino Disks

Another useful measurement configuration is the Corbino geometry (figure 3.5(e)). It consists of a central contact that is connected via the actual device with an outer ring contact. This geometry eliminates any Hall voltage contribution such that only the longitudinal contribution V_{xx} is measured. Thus, the longitudinal resistivity is directly accessible and no tensor inversion, which is only valid for homogeneous 2DEGs (see above), is necessary. This allows a more accurate measurement of small conductivities and renders the configuration interesting in view of the edge channel picture. As another advantage the device comprises no edges but is only framed by the contacts, thus avoiding effects due to different edge configurations and chemical terminations.

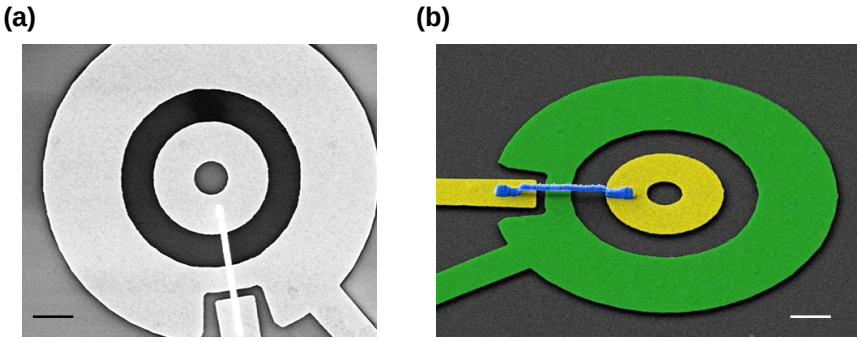

Figure 3.8: Top- and side-view SEM images of Corbino devices. The scale bar is 1 μm. (a) The graphene around the outer and within the inner ring has been etched away so that outer and inner contact are only connected by the graphene layer in between. (b) The air-bridge (colorized blue) connects the inner ring to its lead (both colorized yellow). The outer contact is colorized green.

Figure 3.8(a) shows the top view of a graphene flake contacted in the above described Corbino geometry. The graphene in the center of the inner contact and around the outer contact has been etched away by RIE to avoid short-circuiting. Imaging at an angle provides a three-dimensional impression of the device (figure 3.8(b)). The inner contact is connected to its lead by an air bridge.
The resistivity can be calculated from:

$$\rho_{xx} = \frac{2\pi R_{xx}}{ln\left(\frac{r_1}{r_2}\right)}, \tag{3.8}$$

where r_1 is the outer and r_2 the inner radius of the graphene disk. Since there is no transverse contribution, the conductivity is the inverse of the resistivity. Figure 3.9 exemplifies the longitudinal conductivity of a graphene Corbino device (8818_$D3$), as derived from the measured resistance via equation 3.8. As expected, the filling factors $\nu = \pm 2, \pm 6, ...$ characteristic for monolayer graphene can be observed.

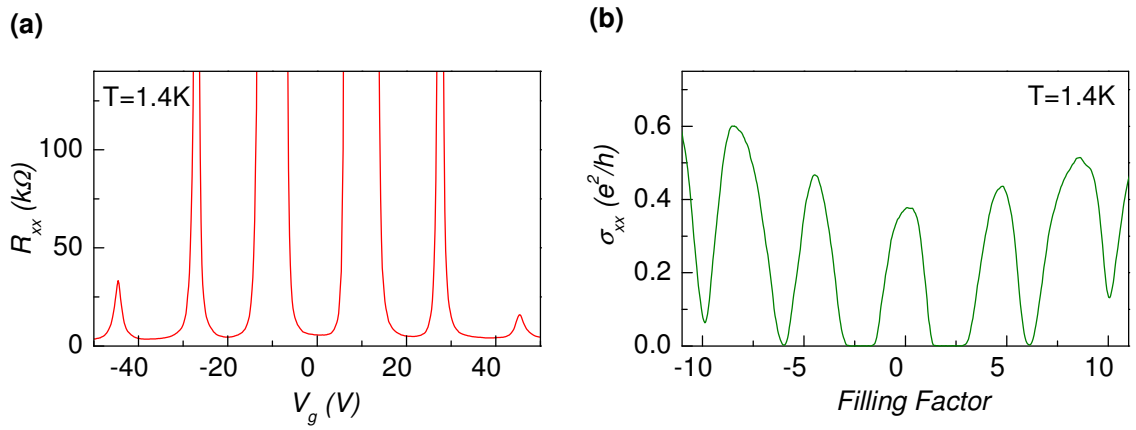

Figure 3.9: Direct measurement of the longitudinal resistance in Corbino sample 8818_$D3$. The outer radius of the flake is 2.5 μm and the inner radius 1.5 μm. (a) Longitudinal resistance R_{xx} at $B = 12\ T$ and $T = 1.4\ K$. (b) Corresponding longitudinal conductivity.

3.3 Combined Low Temperature Magnetotransport and Confocal Microscopy

For combined low temperature magnetotransport and confocal microscopy experiments, a ^3He-system is built up. It comprises two different inserts, one with a rotatable sample holder (rotator insert), and the other with a fiber-based confocal microscope (CFM insert). The custom-made chip carrier sockets are equipped with a 20 pin twisted pair electrical measurement wiring for simultaneous bonding of multiple devices on one chip. One of the pins is used to apply a back gate voltage to tune the charge carrier density of the device (equation 3.1).
The common equipment for measurements with the rotator insert and the CFM insert is shown in figure 3.10. It consists of the Dewar (figure 3.10(a)) with a 66 l liquid nitrogen shield and a 70 l liquid helium main bath. For better isolation the nitrogen shield is surrounded by an outer vacuum chamber (OVC), which has to be evacuated before cool down of the Dewar ($p < 1 \cdot 10^{-5}\ mbar$; leakage rate $< 1 \cdot 10^{-8}\ mbar \cdot l/s$). The standard cool down procedure of the Dewar from room temperature to liquid helium temperature is described in appendix B. The superconducting magnet consists of a Nb_3Sn solenoid, arranged such that the magnetic field is maximal at the sample position (for complete insertion of the inserts). It can be operated at magnetic fields up to 15 T with a maximum B-field sweep rate of 1.0 T/min (conversion factor 6.82 A/T) and a minimum distance of the Dewar bottom to the ground of 20 cm (necessary to limit the forces from the steel grid in the floor on the magnet). Pumping on the main bath via the lambda fridge port cools it to 2.2 K and allows operation of the magnet up to 17 T with a B-field sweep rate of 0.5 T/min. The rotary pumps for pumping on the 1K-pot line of the insert and the lambda fridge port of the Dewar are placed in a pump box, and the pump lines are

embedded in a sand box to minimize vibrational noise. Figure 3.10(b) shows the rack with the measurement computer as well as the piezo- and temperature control units.

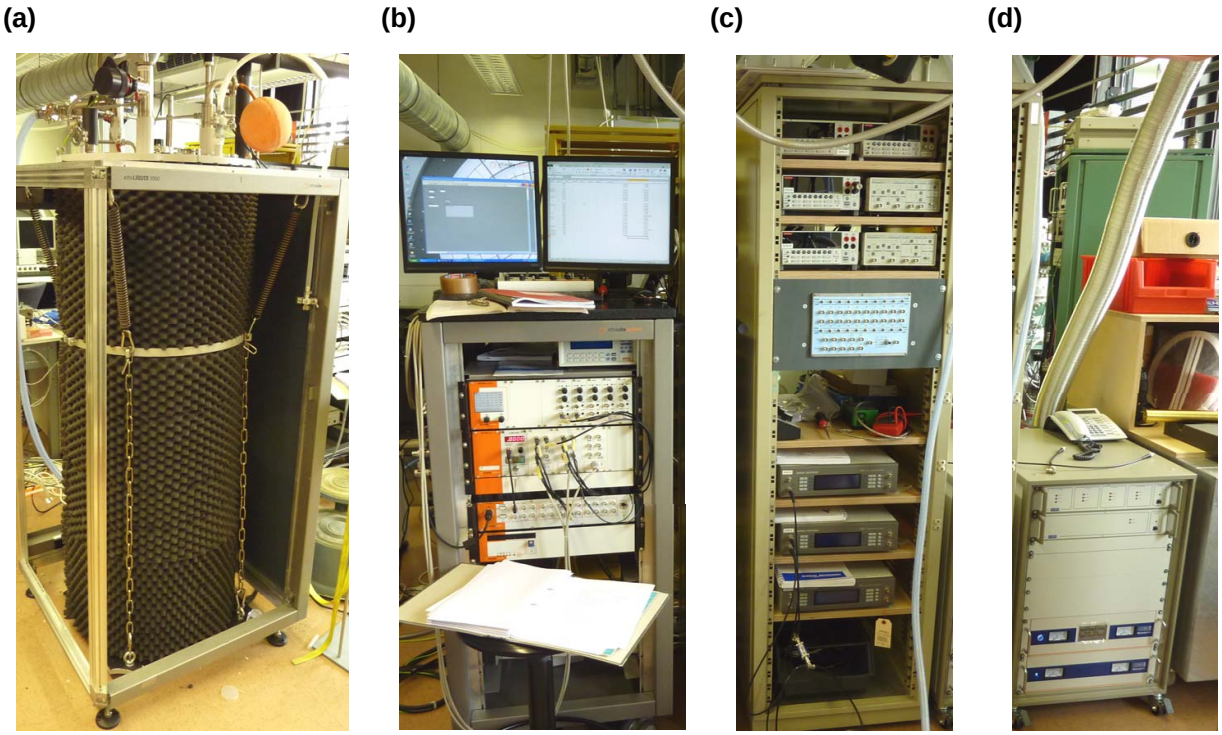

Figure 3.10: Dewar and auxiliary components of the combined magnetotransport and confocal microscopy ^{3}He-cryostat setup. (a) Dewar suspended in a rack by springs. (b) Rack computer, piezo control unit and temperature control units. (c) Rack with hardware for electrical transport measurements. (d) Control unit (power supply) for the magnet, lambda fridge control and stepper motor control for the sample rotation.

For temperature measurement, both the inserts are equipped with sensors at the sorb, the ^{3}He-pot and the 1 K-pot (for a complete list of sensors including their ranges and locations, see appendix B). The ITC has to be calibrated each time for the respective Cernox sensor, either of the rotator or the CFM insert (see appendix B). The hardware for the electrical characterization is shown in figure 3.10(c). In order to eliminate grounding problems, the power supplied to the measurement equipment is provided by transformers, and the connection via GPIB to the measurement computer is made via a galvanic decoupled USB isolator. A filter box with low pass filters (pi-filters) can be added to the measurement connection at the top of the insert. The magnet control unit is shown in figure 3.10(d). The system furthermore comprises a turbo pump to evacuate the inner vacuum chamber (IVC) and a crane system for lifting the two inserts. Both inserts are provided with a ^{3}He reservoir. Upon loading of the insert, the insert is first cooled to liquid ^{4}He temperature followed by operation of the 1 K-pot. Pumping at the 1 K-pot (with open needle valve) further reduces the temperature of the insert. This initiates the condensation process of

the ^{3}He gas as soon as the ^{3}He-pot temperature falls below the 1 K-pot temperature. For this process the sorb is heated by the sorb heater to $\approx 35\ K$ and the needle valve is gradually closed till the minimum condensation temperature of $\approx 1.4 - 1.6\ K$ is reached. After condensation, the base temperature ($\approx 250\ mK$) can be reached within $\approx 30\ min$ and kept for the hold time of the insert, which depends on the heat load (introduced by ramping of the magnet, sample rotation, scanning of the sample, or general movement of the piezos). The coldest part of the insert at this instance is the ^{3}He-pot, which is thermally well coupled to the sample. The temperature can be raised by a combination of the sorb and ^{3}He-pot heater up to 100 K, with the insert completely submerged in the Dewar. The CFM insert comprises a RuO and $PT1000$ sensor near the sample space for accurate measurement of temperatures below 1.4 K and above room temperature, respectively. A heater coil ($d = 0.2\ mm$ manganin with $l = 3.5\ m$, $R = 50\ \Omega$; maximum current $I \leq 0.58\ A$), triggered by a Lakeshore temperature controller, is used for sample annealing in vacuum up to 105 $°C$ before inserting the CFM insert into the Dewar. The rotator insert by comparison, can only be heated externally via a heater strip.

3.3.1 Magnetotransport in Tilted Magnetic Fields

The low temperature part of the rotator insert is shown in figure 3.11(a). It allows out-of-plane rotation of the sample in an external magnetic field. Without any applied heat load, the base temperature of 225 mK at the ^{3}He-pot can be maintained for $t = 140\ h$. The sample rotation is tested with a graphene Hall bar device (see figure 3.11(b) and (c)). In the longitudinal resistance Shubnikov de Haas oscillations are observed, while plateaus characteristic of graphene are visible in the Hall resistance. The latter occur at the usual graphene filling factors (see chapter 2; filling factors 6, 10, 14 and 18 are indicated in the graph). The measurement is performed at a charge carrier density of $q = -2.14 \cdot 10^{12}\ cm^{-2}$. The signal is strongest at $\theta = 180°$ (defined as the angle between the surface normal and the magnetic field) and decreases upon rotation to 90°. Here, the sample is in plane with the applied magnetic field and the Hall resistance is zero. Upon further rotation the Hall resistance changes its sign.

3.3.2 Low Temperature Confocal Microscopy (CFM)

The low temperature part of the CFM insert is shown in figure 3.12(a). It comprises three positioners and an x, y-scanner. On top of the piezo stack, the low temperature objective is mounted and can thus be moved in x, y and z direction to scan and focus the sample. The optical fiber is coupled into the ferrule on top of the objective. It is optimized for the laser wavelength of the diode laser ($\lambda = 635\ nm$). The housing is thermally anchored at the ^{3}He-pot in order to efficiently cool the sample on top of the cold finger. The chip carrier socket holds the chip carrier with the sample. At room temperature the range of the piezo voltage is 4 V, while at low temperatures it is 10 V. The voltages are amplified by a factor of 15, which results in 60 V and 150 V, respectively.

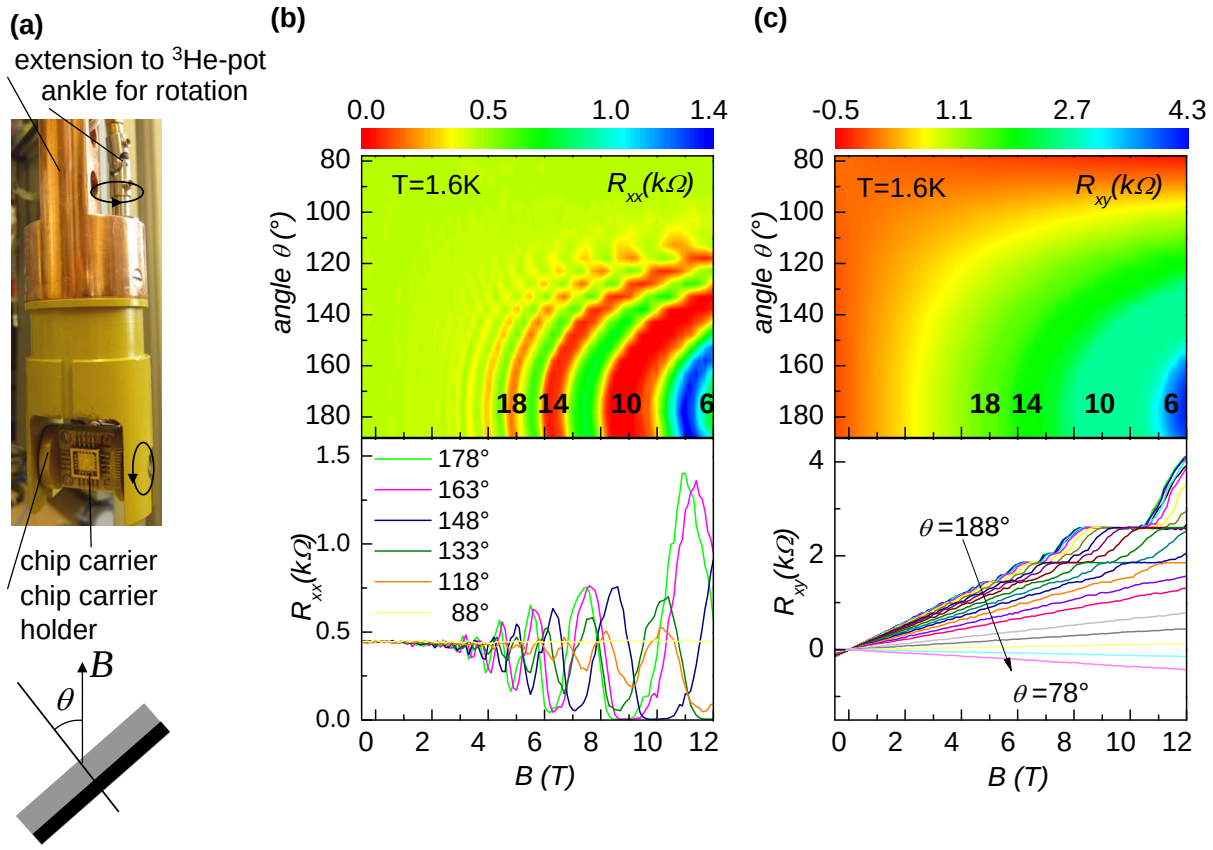

Figure 3.11: Low temperature part of the rotator insert and measurements of the longitudinal and transverse resistance of graphene Hall bar sample (10268_$D2$) at $T = 1.6\ K$ and $q = -2.14 \cdot 10^{12}\ cm^{-2}$, recorded by rotating the sample in the magnetic field. The angle is measured between the surface normal of the sample and the magnetic field direction. (a) Low temperature part of the rotator insert for out-of-plane rotation of the sample in an external magnetic field. The sample wiring is in the back, which prevents full rotation by 360°. (b) B-field dependent longitudinal resistance, and (c) Hall resistance, both measured at $T = 1.6\ K$.

For positioning the sample at room temperature the positioners are operated at $\approx 40\ V$ and 200 Hz. Their capacity in this temperature range is 1.04 μF. At low temperatures, the operation voltage of the positioners should be increased to $\approx 60\ V$ with a capacity of 180 nF. A nominal laser power of 40 μW gives a good reflection signal from the Si/SiO_2 substrates. How to convert the nominal laser power to the measured power is described in appendix B. A test sample with a 5 μm grid is used for the fine calibration of the lateral dimensions, which yields the output limits at the respective temperature. At room temperature the maximum scan range corresponds to 40 μm, and at 300 mK (sample temperature) to 34 μm. The scale in between these temperatures has to be extrapolated.

For navigation on a substrate a marker system has been developed with numbered markers spaced 50 μm from each other (see appendix B). The test grid sample can also be used to determine the lateral resolution. Figure 3.12(b) shows a scan of the test grid at 300 mK sample temperature (20 $\mu m \times 20$ μm scan range; 1 $\mu m/s$ scan velocity; 0.04 mW nominal laser power; $t \approx 18$ h hold time). Assuming a rectangular cross-section of the grid lines, the resolution obtained from the slope between grid bottom and grid top is $FWHM = 505 \pm 51$ nm. Under such scanning and laser illumination conditions the hold time is 18 h.

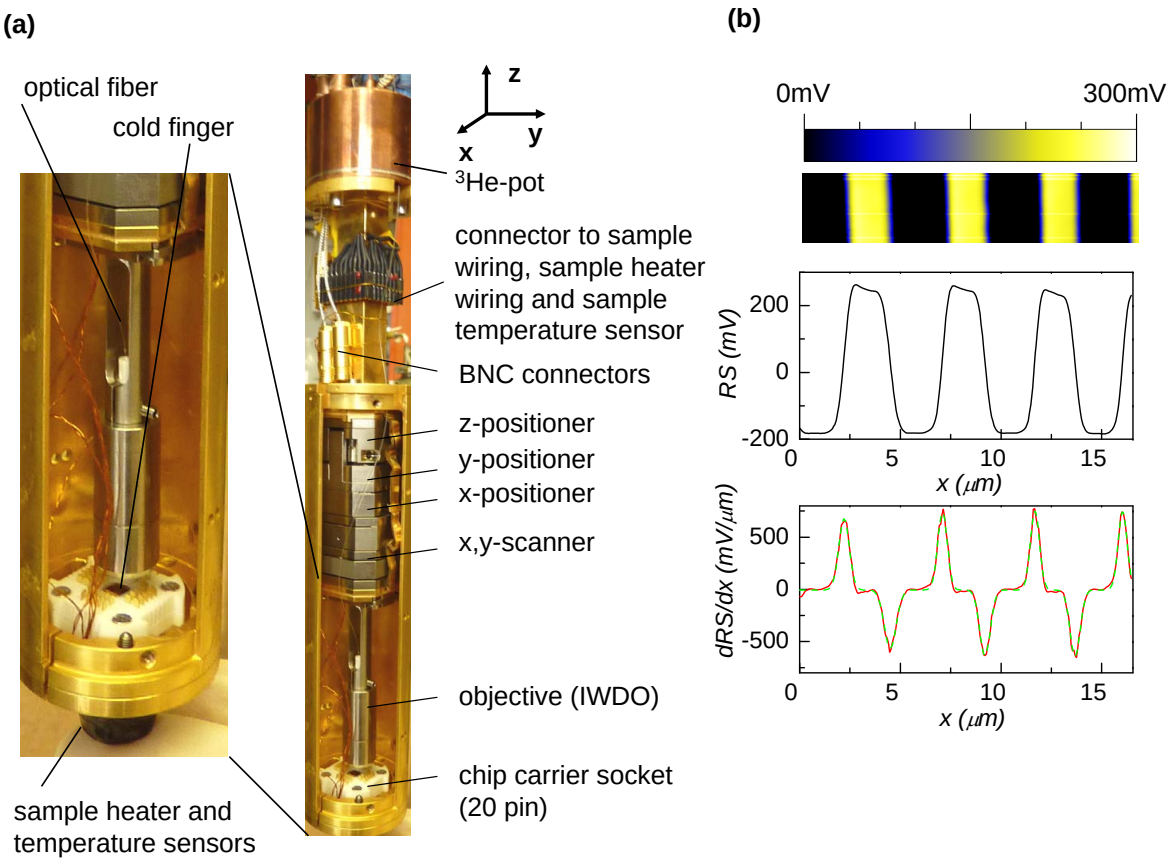

Figure 3.12: Low temperature part of the CFM insert (a) and scan of the test grid sample at 300 mK (b). From a multiple peak fit (dashed green line in lower panel) of the derivative (solid red line in lower panel) of the line profile, the lateral resolution is determined.

Chapter 4

Bilayer Graphene in Electric and Magnetic Fields

Introduction

In this chapter, the opening of a band gap in bilayer graphene in magnetic and electric fields is investigated. Theoretical studies have shown that an electric potential difference between the upper and lower graphene layer of Bernal stacked bilayer graphene introduces a gap opening with the gap size depending on the applied electric field [20]. The electric field breaks the symmetry of the upper and lower layer, which introduces a polarization of the valley degree of freedom in the lowest LL, since here the layer degree of freedom is associated with the valley degree of freedom. At the same time, the band structure at low energies, close to the opened gap, is transformed from the parabolic dispersion typical of bilayer graphene to a so-called Mexican hat-shaped dispersion [20, 85, 86]. Experimentally, this band structure modulation has been confirmed by angle-resolved photoemission spectroscopy (ARPES) [87], and the expected band gap size could be verified by optical spectroscopy [88–90]. Electrical transport measurements have also enabled measurement of the gap size [21]. In such experiments, the electrical field can be controlled independently of the carrier concentration via a top gate in addition to the Si/SiO_2 back gate. The top gate fabrication requires the addition of a gate dielectric on top of the bilayer flake. Similarly to the influence of the SiO_2 back gate dielectric, the quality of the bilayer graphene flake, being inferior to monolayer graphene subjected to the same treatment and measurement conditions [91], is usually further decreased by such a structure. The increased disorder is likely to prevent the observation of an exponential temperature dependence expected for a gap opening and results in an experimental gap size that is smaller than expected by theory. One strategy to overcome this problem is to suspend the flake between the top and the bottom gate using the air space between the flake and the gate as dielectric [22]. This method enables evaluation of the interdependence of the gap properties and the Landau level structure, including the gap influence on degeneracy-lifted levels in electric and magnetic field. However, the accessible electric field range and the device geometry options are limited due to the mechanical fragility of the suspended graphene sheets. A too small size

of the suspended sheets can quench the Quantum Hall effect, especially in multi-terminal devices [66].

Experiment

Here, we investigate the behavior of suspended bilayer graphene in vertical electric and magnetic fields. For separate measurement of the longitudinal and Hall resistance, the contacts of the devices are structured in Hall bar geometry without etching of the flake. Figure 4.1(a) displays the device configuration and measurement setup used for acquisition of the Hall (V_{xy}) and the longitudinal (V_{xx}) voltage. An applied potential difference between the top and the back gate generates an electric field $\vec{E}$ between the gates, where the bilayer graphene device is located as shown in 4.1(b). The induced charge carrier density depends on $V_t = V_{top} - V_{CNP}$ and $V_b = V_{back} - V_{CNP}$.

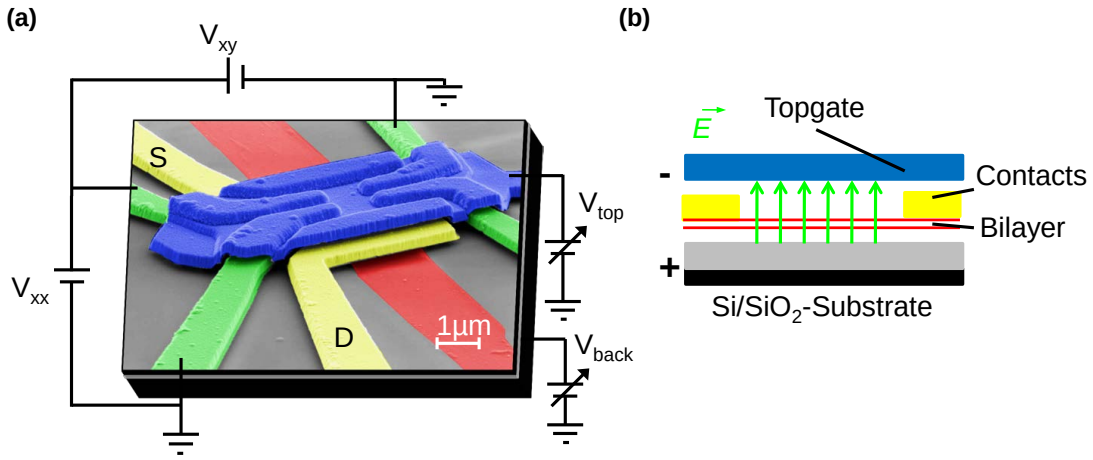

Figure 4.1: Device configuration for Hall bar measurements on bilayer graphene in electric and magnetic fields. (a) SEM image of a Hall bar device with a schematic depiction of the electrical circuit setup for acquiring lateral and transverse resistances. The source (S) and drain (D) contacts are colorized yellow, the Hall probes green, the top gate blue and the graphene bilayer flake red. (b) Schematic cross-section of a graphene bilayer suspended between a top- and bottom gate. A potential difference between the gates results in an electric field perpendicular to the sheet.

The measurements are performed with standard lock-in amplifier techniques at temperatures between 50 mK and 4 K under magnetic fields of up to 12 T and at low enough currents to prevent heating effects. All of the devices have been current-annealed before measurement (up to ≈ 1 mA). After this cleaning step typical device mobilities are $\mu \approx 15,000\ cm^2(Vs)^{-1}$.
The degeneracy lifting of the lowest LL of the bilayer graphene devices in magnetic field is investigated in section 4.1. In section 4.2, the effect of combined magnetic and electric field, as well as the independent control of electric field and carrier concentration is

demonstrated. A discussion of the observed splitting is given in section 4.3, while section 4.4 deals with the emergence of a spontaneous gap at low electric and magnetic fields.

Devices

The suspended bilayer graphene devices are fabricated from mechanically exfoliated graphene (see chapter 3). The top gate is structured after definition of the contacts in Hall bar geometry. Here, the flake is not etched into an ideal Hall bar shape, but the contacts are patterned directly on a bilayer stripe in order to attain sufficient mechanical stability for the suspension. A spacer layer of 150 nm SiO_x is deposited via e-beam evaporation on top of the device prior to definition of the metal top gate (3 nm Cr/ 150 nm Au). This layer is etched away completely in the suspension step and thus determines the distance from the flake to the top gate, while only half of the back gate dielectric is removed (see chapter 3).

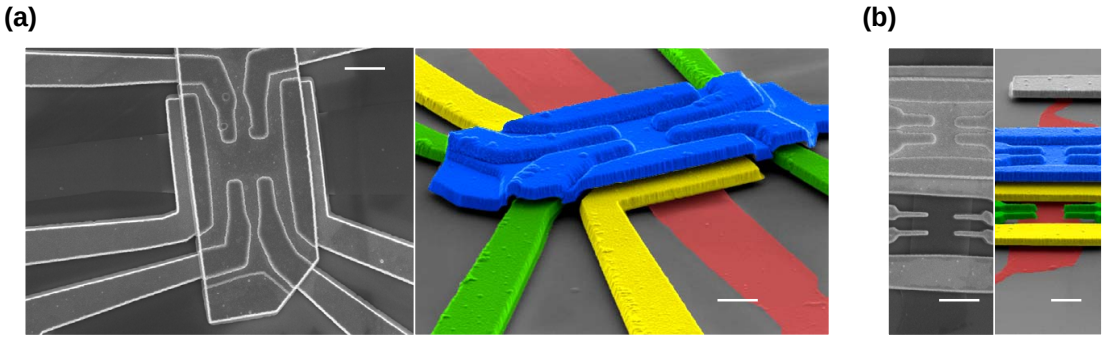

Figure 4.2: Bilayer graphene devices in Hall bar geometry with and without top gate. The scale bar is 1 μm. In the side view images the top gate is colorized blue, the graphene bilayer red, the Hall probes green and the current contacts yellow. (a) Top- (Inlens detector) and side view (SE2 detector) SEM image of a Hall bar device. (b) Top- (Inlens detector) and side view (SE2 detector) SEM image of another sample with and without topgate.

Figure 4.2 shows scanning electron microscopy (SEM) images of different graphene bilayer devices with or without top gate. Detection by the Inlens detector, as shown on the left side of the panels, reveals the contours of the structured devices. The edges of the bilayer flake appear bright near the main current contacts since there the flake is pinned to the contacts but lies on the substrate if the neighboring contact is too far away. Detection by the SE2 detector, as shown on the right side of the panels, provides a three-dimensional impression of the devices. In these images, the main current contacts are colorized yellow, the Hall probes green and the top gate blue. The bilayer flake itself is shown in red. The device dimensions cannot exceed a few micrometers, since larger flakes bend towards the substrate and do not remain properly suspended. Care must be taken not to place the Hall probes closer to the main current contacts than ≈ 500 nm, since this would shorten the potential lines between the two opposing sides of the flakes (see chapter 2). These

lines meet meet at points at the current contact, so-called hot spots. If the Hall probes are patterned in this area, the QHE is quenched [92, 93].

4.1 Degeneracy Lifting of the Lowest Landau Level in Magnetic Field

As described in chapter 2, the LLs of bilayer graphene occur at $\nu = \pm 4N = \pm 4, \pm 8, \pm 12, ...$, where the lowest LL comprises a spin, valley (layer) and orbital degeneracy. Similar to monolayer graphene, lifting of these degeneracies can be observed for sufficient sample quality in high magnetic fields [94, 95].

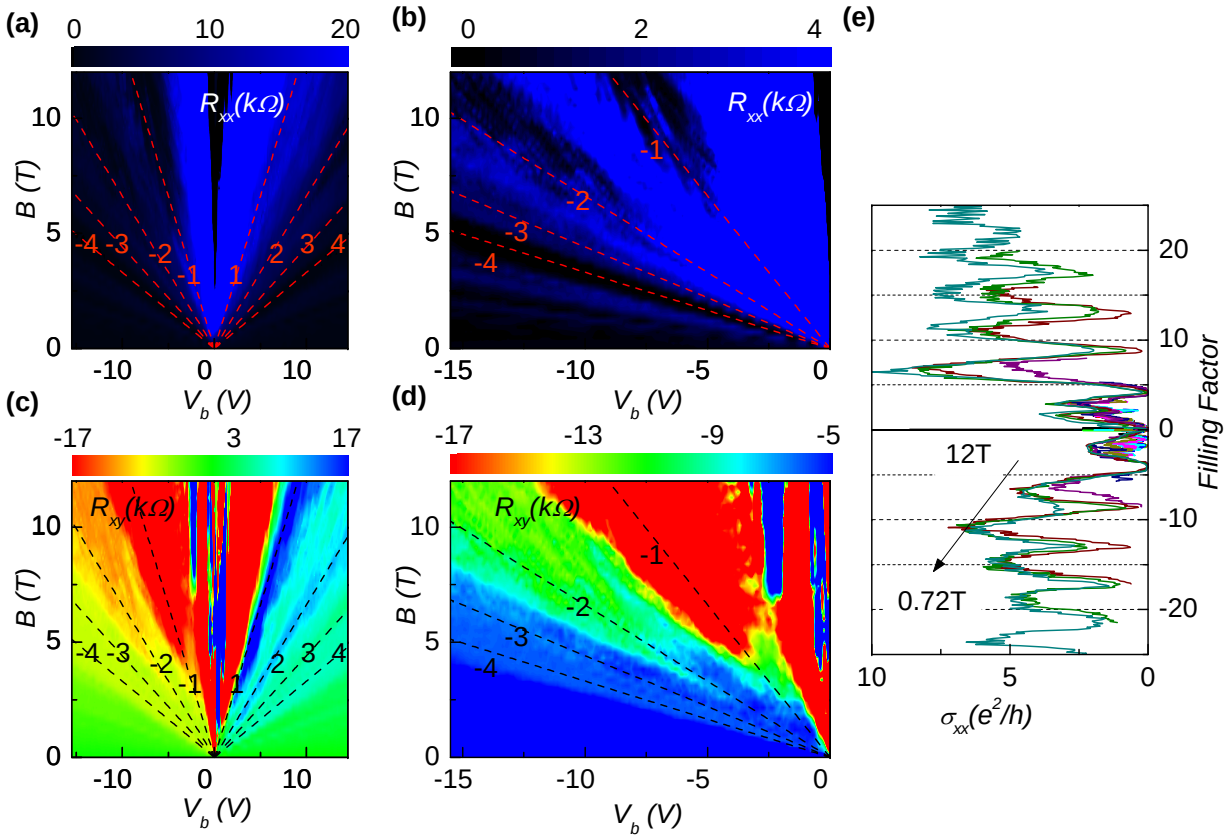

Figure 4.3: Hall bar measurements on bilayer graphene in a magnetic field at $T = 70\ mK$ (sample $EP707010a\_D5$). (a) Fan diagram of the longitudinal resistance. The Landau level positions are indicated by the red dashed lines. (b) Zoom of the longitudinal resistance within the hole region. (c) Fan diagram of the Hall resistance. (d) Zoom of the Hall resistance within the hole region. (e) Longitudinal conductivity under magnetic fields between 0.72 T and 12 T.

Figure 4.3(a)-(d) shows the longitudinal and Hall resistances of a suspended bilayer graphene Hall bar device ($EP070710a\_D5$) at 70 mK. The gate coupling factor is determined from

the filling factor positions in the fan diagrams to $3.2 \cdot 10^{14}\ m^{-2}V^{-1}$. The CNP position is moved to $V_b = 0.55\ V$ after current annealing, which indicates, along with the narrow peak width, a high quality of the device. Besides the usual bilayer graphene filling factors, plateaus (and corresponding zero longitudinal conductivity regions) at additional filling factors are observed. For the shown device the longitudinal resistance at the CNP diverges for increasing magnetic field and at fields as low as $\approx 0.5\ T$ the filling factors ± 2 appear. Due to the non-ideal Hall bar geometry admixtures of the longitudinal and transverse voltages are present, which are most pronounced at filling factor 0 at the CNP, due to the divergence of the longitudinal resistance. The Hall resistance also increases close to the CNP and reaches a value of 12.9 $k\Omega$ which corresponds to filling factor 2 (conductivity 2 e^2/h). For higher magnetic fields, the Hall resistance close to the CNP assumes even higher values of $\pm 25.8\ k\Omega$ (corresponding to filling factor ± 1), although, it still crosses zero at the CNP. The novel filling factors are best visible in the longitudinal conductivity, which is derived by tensor inversion of the resistance (see chapter 3). In figure 4.3(e) this conductivity is plotted for different magnetic fields (ranging from 0.72 T to 12 T). At low magnetic fields, the filling factors for the higher LLs are observed, whereas for higher B-fields they are moved out of the accessible carrier concentration range due to their magnetic field dependence ($\nu = qh/eB$). Figure 4.4(a) and (b) show a zoom into the lowest LL region of the longitudinal and transverse conductivities, as derived from the fan diagrams in figure 4.3 for magnetic fields between 4.8 T and 12 T. In this magnetic field range the degeneracy lifting of the lowest LL is complete, with all integer filling factors visible. The filling factors $\nu = \pm 1$ and $\nu = \pm 3$ start to become observable at $\approx 4\ T$.

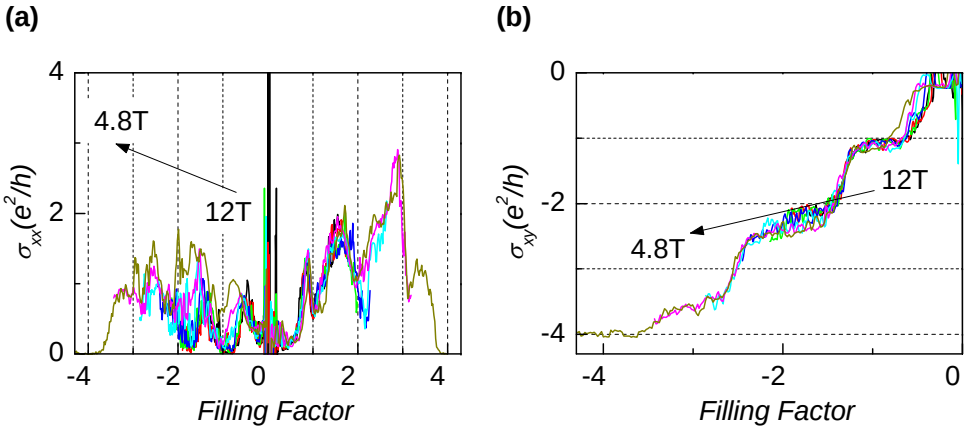

Figure 4.4: Longitudinal and Hall conductivity of bilayer graphene at $T = 70\ mK$ (sample $EP707010a\_D5$). (a) Zoom of the longitudinal conductivity in the lowest LL region. (b) Zoom of the Hall conductivity of the hole side in the lowest LL region.

Similar observations have also been made on monolayer graphene, where filling factor 0 followed by ± 1 appear [96–98]. In this case, the lowest LL, which only possesses spin and valley degeneracy, also assumes all integer values. In a similar way, the higher LLs

can be subject to degeneracy lifting in high magnetic fields. However, since in this field range, these LLs appear at high carrier concentrations, they are not visible in the limited concentration range accessible for suspended graphene.

4.2 Independent Control of Electric Field and Carrier Concentration

The vertical electric field within the bilayer device can be controlled by the combination of top and bottom gate. It depends on the respective gate coupling factors α_t and α_b [88] as follows:

$$E = \frac{e\alpha_b V_b - e\alpha_t V_t}{2\epsilon_0}, \tag{4.1}$$

based upon the capacitances in the simple capacitor model $C_t = e\alpha_t$ and $C_b = e\alpha_b$, and with ϵ_0 as the vacuum permittivity. The gate coupling to the top gate is similar to the back gate, if the distance of the flake to the remaining back gate oxide layer is identical to the distance to the top gate, since the second term in the sum of equation 3.4 dominates due to the involved permittivities. The total carrier concentration is given by the sum of the concentrations induced by the two gates [88]:

$$q = \alpha_b V_b + \alpha_t V_t. \tag{4.2}$$

Figure 4.5(a) displays the transverse resistance of a suspended bilayer ($EP082910a\_D6$) as a function of top and bottom gate voltages. The directions of the electric field and density axis are also indicated. The plot evidences that the conversion from gate to electric field and carrier density dependence corresponds to a matrix rotation by an angle θ with subsequent scaling of the axis. The angle can be derived from the ratio of the two gate coupling factors, or the electric field values in the coordinate system of the gate voltages $V_t(q = 0)$ and $V_b(q = 0)$ as $tan(\theta) = \frac{|V_b(q=0)|}{|V_t(q=0)|} = \frac{\alpha_t}{\alpha_b}$. For the device in figure 4.5(a) one obtains $\theta = 28°$. The back gate coupling factor, determined from the fan diagrams similarly to monolayer graphene (see chapter 3), is $\alpha_b = 3.0 \cdot 10^{14}\ m^{-2}V^{-1}$. With the angle θ a top gate coupling factor of $\alpha_b = 1.6 \cdot 10^{14}\ m^{-2}V^{-1}$ follows. The gate coupling factor demonstrates that while only slightly less SiO_2 ($\approx 90\ nm$) was etched below the flake than the targeted 150 nm, the top gate distance from the flake is around 340 nm for this device. In figure 4.5(b), equation 4.1 and 4.2 have been used to plot the transverse resistance in the coordinate system of electric field and carrier concentration. Regions of high resistance are shown in red and appear on the electric field axis for small electric fields, which is followed by a minimum and an increase at sufficiently high positive (or negative) electric fields. While the exponential resistance increase in the high field region is expected due to the gap opening, the low-field, highly resistive region must have a different origin. For more details on this spontaneous low-field gap, see section 4.4. The high field gap depends on the applied electric field and has been theoretically predicted to be as large as 10 meV at electric fields of $\approx 0.1\ V/nm$ [20]. In experiment, however, even in suspended bilayers with

lateral two-terminal contacts, a significantly smaller gap of $\approx 0.6\ meV$ at $80\ mV/nm$ [22] has been found. This discrepancy might be ascribed to remnant disorder, or non-uniform and rough edges of the sheet.

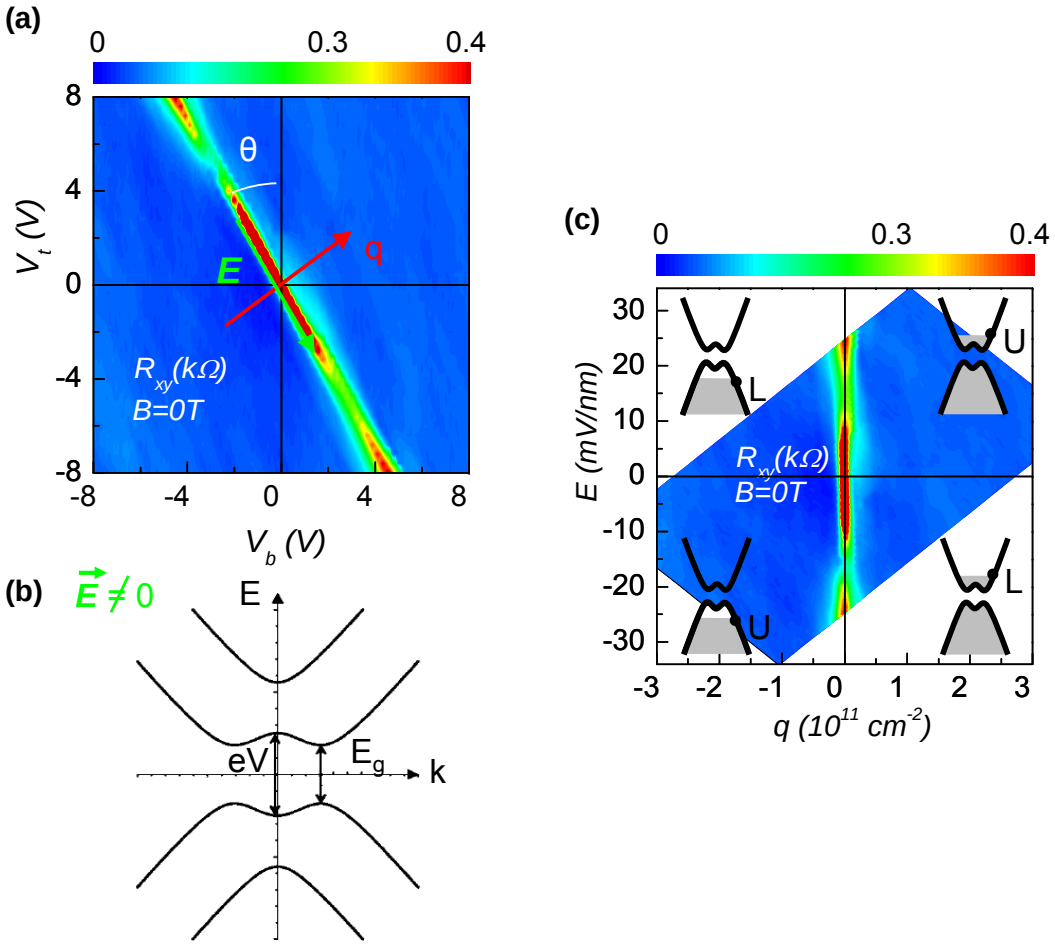

Figure 4.5: Control of electric field and carrier density in bilayer graphene (sample $EP082910a\_D6$). (a) Transverse resistance at $B = 0\ T$ as a function of bottom (V_b) and top (V_t) gate voltage. (b) The potential difference between the two layers introduced by the gates opens a gap and alters the low-energy band structure (adapted from [20]). (c) By a matrix rotation and scaling, the electric field E and charge carrier concentration q axes can be obtained. The potential difference leads to a polarization of the valley degree of freedom depending on the sign of the electric field and the carrier type. The conduction is p-type for negative concentration (hole conduction) and n-type for positive concentration (electron conduction).

Figure 4.5(b) illustrates the influence of finite electric field on the parabolic low energy band structure of bilayer graphene. A finite electric field opens up a band gap. Conduction occurs via holes for negative densities and electrons for positive densities q, respectively. The

electric field furthermore breaks the inversion symmetry by imposing a different potential on the upper and lower layer of the flake, and thus separates the charge carriers in valley K' and K in the lowest LL, as the valley degree of freedom can be associated with the two layers [99]. Furthermore, for the lowest LL the two charge carrier types possess different chirality (valley degree of freedom). This is highlighted in figure 4.5(c), where for positive electric fields, electrons are assumed to be associated with the upper layer U, and for negative electric fields with the lower layer L. Correspondingly, holes are associated with L for positive electric fields and with U for negative electric fields.

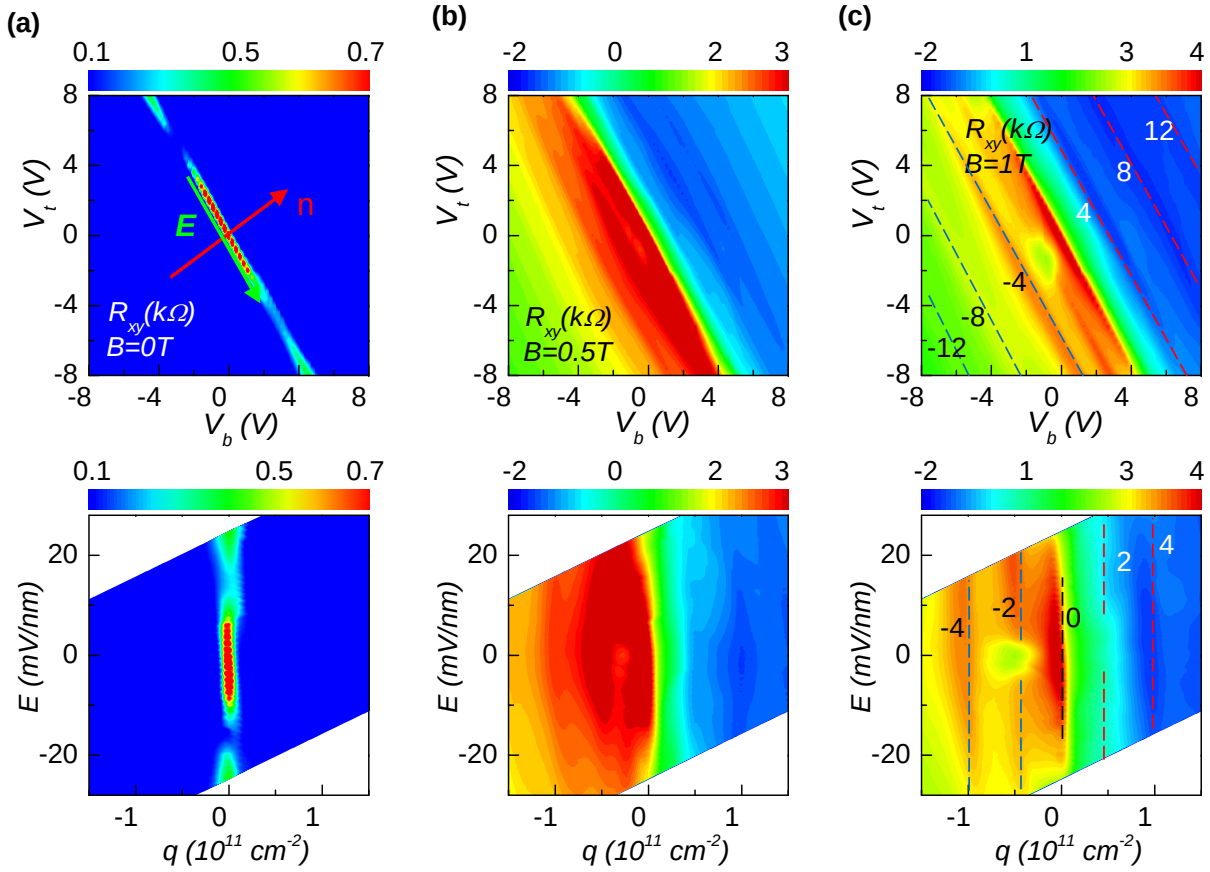

Figure 4.6: Transverse resistance of bilayer graphene as a function of bottom (V_b) and top (V_t) gate voltage (upper panels) and in electric and magnetic field (lower panels) (sample $EP082910a\_D6$). (a) Transverse resistance at $B = 0\ T$. Before the gap due to the electric field opens up, the resistance drops at both negative and positive electric field. (b) The transverse resistance at $B = 0.5\ T$. It is asymmetric in charge carrier density. (c) At higher magnetic fields of $B = 1\ T$ the QHE becomes observable in the transverse resistance. Filling factors ± 4, ± 8 and ± 12 appear. The ± 2 filling factor is devided by a resistance drop on the electric field axis due to LL crossings.

If additionally to the electric field, a magnetic field is applied, Landau levels are formed. In figure 4.6, the transverse resistance is plotted for magnetic fields $B = 0\ T$, $B = 0.5\ T$ and $B = 1.0\ T$ as a function of top and bottom gate in the upper, and as a function of electric field and carrier concentration in the lower panel. At the latter magnetic field, filling factor $\nu = \pm 2$ emerges, although it is separated into two regions by a resistance dip towards zero on the carrier concentration axis ($E = 0$), such that the region of $\nu = 0$ is directly connected with the region of $\nu = \pm 4$ without crossing $\nu = \pm 2$. On the electric field axis ($q = 0$), the zeroth filling factor is separated into one region at small fields and one at higher fields, where $\nu = 0$ reappears, as already observed for the high resistive regions at zero magnetic field. For increasing magnetic field, the transition points move to higher absolute electric field. This behavior has been explained by LL crossings in electric field [22] and will be further discussed in the next section.

4.3 Splitting Models

In high quality monolayer and bilayer graphene in elevated magnetic fields, splitting of the $N = 0$ LL is well-documented. While the lowest LL is only 4-fold degenerate in monolayer graphene with spin and valley degeneracy, in bilayer graphene, it is 8-fold degenerate due to the additional orbital degeneracy [99]. For both, monolayer and bilayer graphene with increasing magnetic field, the filling factor $\nu = 0$ appears as the first filling factor that arises from degeneracy lifting. Similar to monolayer graphene, where it has been ascribed to the Zeeman effect [98], either pure or with a correction due to electron-electron interactions [96], also for bilayer graphene a spin-related origin has been predicted theoretically [100, 101] and is in accordance with experiment [94, 95]. Thus, the hierarchy of the degeneracy lifting should involve first lifting of the spin degeneracy, followed by splitting of the valley degree of freedom. On this basis, the appearance of the filling factors ± 1 is ascribable to lifting of the valley degeneracy lifting which occurs at higher magnetic fields compared to the spin degeneracy lifting. In bilayer graphene, however, the interaction energy due to Coulomb effects is expected to exceed the splitting due to the Zeeman effect [100, 102]. Accordingly, interaction effects should play a dominant role govern the spin, valley and orbital degeneracy lifting, which are theoretically predicted to occur in this order with the exchange energy being largest for the spin degree of freedom, followed by that of the valley and finally the orbital degree of freedom [100]. This splitting scenario is summarized in figure 4.7(a).
Under applied electric field the inversion symmetry of the two layers is broken, which corresponds to a separation of the charge carriers in the two valleys, which implies lifting of the valley degeneracy in the lowest LL [99]. As a function of electric field, LLs with different layer (valley) polarization are expected to have slopes of opposite sign, such that they cross at certain points on the concentration and electric field axis. The transition points of decreased resistance might be interpreted in the framework of this model of crossing LLs as the crossing points [22]. The LL crossing model is explained as follows: Figure 4.7(b) shows the situation, where spin degeneracy lifting is present due to a finite

magnetic field with additional application of an electric field (while orbital degeneracy lifting is neglected). Thus, in both applied electric field and magnetic field, the $\nu = 0$ region is segregated into three regions. In accordance with theory [101, 103], this can be rationalized as one state at low electric field and two layer (valley) polarized states at higher positive and negative electric fields with opposite layer (valley) polarization. Upon crossing the concentration or electric field axis, the layer (valley) polarization changes. On the concentration axis, additional crossings appear, where a decreased resistance is observed within filling factors $\nu = \pm 2$. Here, LLs with the same spin polarization but opposite layer polarization cross if the low field state is assumed to be spin polarized. Thus, the $\nu = 0$ region at low concentration enters directly into a $\nu = \pm 4$ region, without passing $\nu = \pm 2$. At the transitions points, a decreased resistance is observed. Recent measurements indicate, however, that the low electric field state is a canted antiferromagnetic (CAF) state [104], which is dominant for high magnetic fields with a transition to a spin-polarized state only at elevated magnetic fields, while the layer (valley) polarized states are dominant for high electric fields.

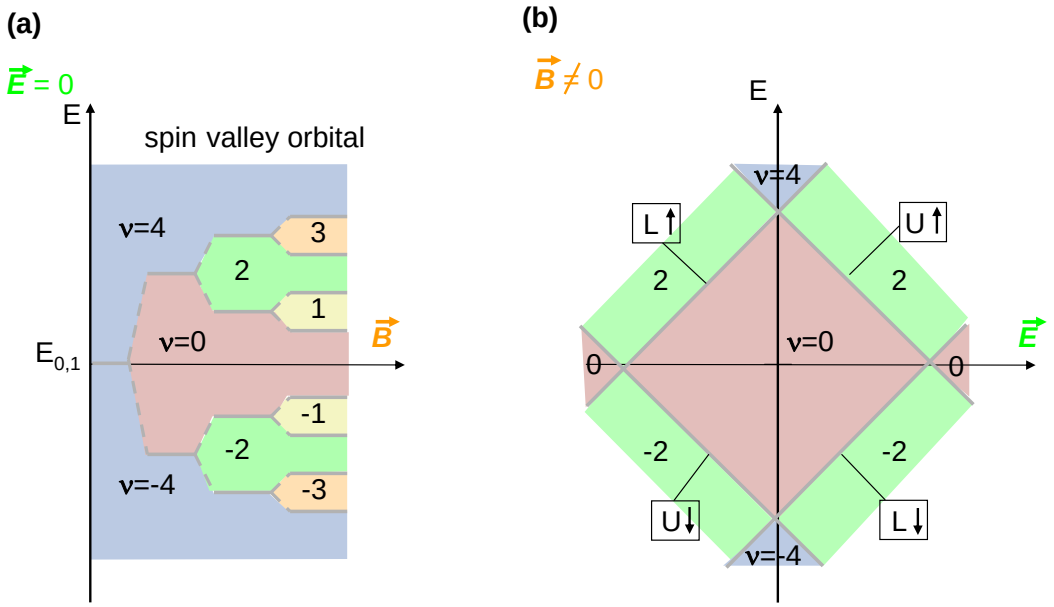

Figure 4.7: Models of the Landau level splitting in magnetic and electric field applied to bilayer graphene. (a) Schematic representation of the LL splitting for the lowest LL (adapted from [95]). With increasing magnetic field splitting occurs due to spin degeneracy lifting, followed by valley and orbital degeneracy lifting. Additional filling factors appear due to the splitting. (b) Landau level splitting in electric field (adapted from [22]).

4.4 Spontaneous Low Field Gap

Besides the spin or layer (valley) polarized states of the lowest LL, an additional spontaneous gap is observed, which persists down to zero electric and magnetic field, but is quenched by the application of higher fields. This phase is exemplified in figure 4.8, where the transverse resistance of a bilayer sample ($EP707010a\_P5$ with gate coupling factor $\alpha_b = 3.2 \cdot 10^{14}\ 1/m^2$) is plotted as a function of back gate voltage (density) and magnetic field at zero electric field (panel (a)) or as a function of density and electric field at zero magnetic field (panel (b)). For B-fields above $B_c = \pm 50\ mT$, the spin polarized $\nu = 0$ state appears. At lower fields, the resistance drops and rises again towards zero magnetic field. The same trend is observed for low electric fields with a transition occurring at $E_c = \pm 15\ mV/nm$ at zero magnetic field for another sample ($082910a\_D6$ with $\alpha_b = 3.0 \cdot 10^{14}\ 1/m^2$ and $\alpha_t = 1.6 \cdot 10^{14}\ 1/m^2$). Above these fields, the gap due to the layer (valley) polarization occurs.

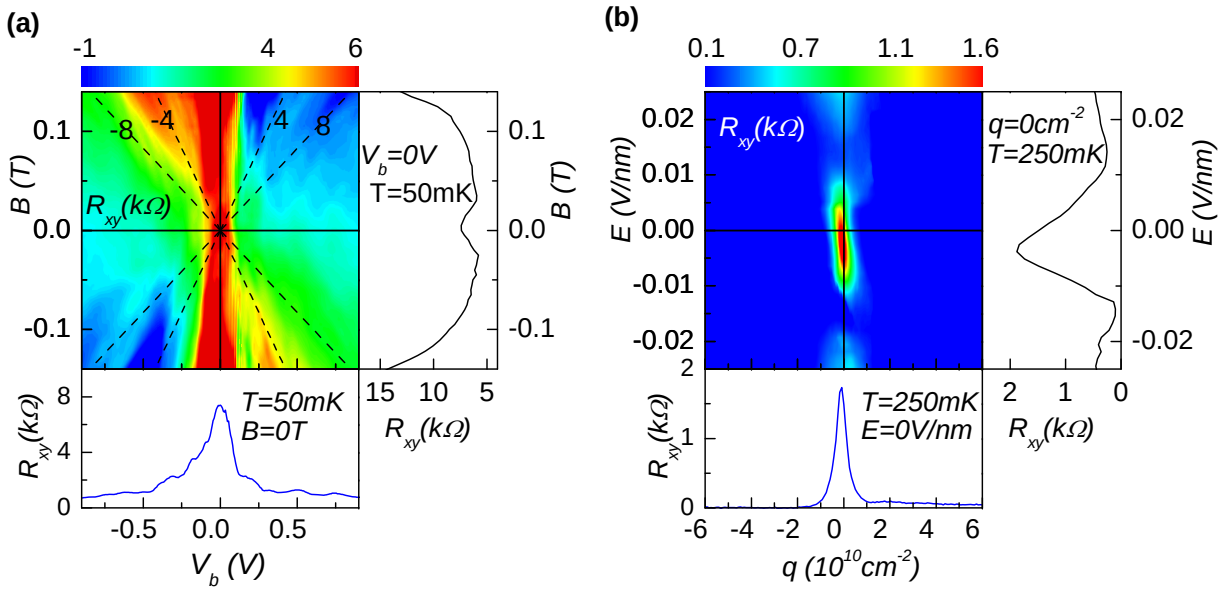

Figure 4.8: High resistive phase observed for low magnetic and electric fields, as well as low gate voltages (charge carrier densities q). (a) Plot of the transverse resistance measured at low magnetic fields and $T = 50\ mK$. The critical magnetic field is $B_c \approx 50\ mT$. (b) Plot of the transverse resistance measured at low electric fields and $T = 250\ mK$. The critical electric field is $E_c \approx 15\ mT$.

Such electric-field dependent transition is in accordance with theoretical predictions [101, 103]. However, these models cannot account for the transition observed in magnetic field. The latter signifies a new phase since neither the spin-polarized nor the layer-polarized phases persist down to zero magnetic and electric field. This new phase is hence different from the spin-polarized phase under higher magnetic fields and also from the layer

(valley)-polarized phase under higher electric fields. Besides its instability to applied external fields, the highly resistive phase is also unstable towards increased charge carrier concentration, and is only observed close to the CNP. The observed opening of a spontaneous gap at zero electric and magnetic field in bilayer graphene may originate from electron-electron interactions predicted by various theories [17, 101, 105–110]. One of these models [101, 107] predicts the formation of an anomalous Hall insulating state in which time reversal symmetry is spontaneously broken and layer (valley) polarization is present, while an alternative model attributes the increased resistance to the formation of two Dirac cones at the CNP due to breaking of rotational symmetry [109, 110]. In accordance with the first model [101, 107], the present devices exhibit a non-divergent, finite resistance in the spontaneous gap region, with a transition occurring at lower magnetic field ($\approx 50\ mT$) than predicted ($\approx 500\ mT$). The second scenario would also be consistent with the experimentally observed conductivity decrease, since it predicts a decreased density of states at the Dirac point due to the broken rotational symmetry. Since both models are consistent with the magnetotransport data, further experiments are necessary to confirm one of these models. To this end, Kerr effect measurements have been suggested [111].

Chapter 5

Graphene Antidot Lattices

Introduction

In the following three chapters (chapter 5, 6 and 7), spatial confinement is investigated as another approach towards band gap-opening in graphene. Since graphene is by definition a material already confined to two dimensions, further confinement results in quasi $1D$ stripes called graphene nanoribbons (GNRs). Theoretical studies, using tight binding (TB) theory or density functional theory (DFT) calculations, have predicted that the band structure of such ribbons depends on the edge structure and the ribbon width [24, 112, 113]. In particular, TB theory predicts that GNRs with pure zig-zag edges are metallic, while armchair edges result in either semiconducting or metallic behavior of the GNR depending on its width. The ribbon width also influences the gap size, specifically the gap size scales inversely with the width.
For networks of such GNRs, called graphene antidot lattices (GALs), similar predictions have been obtained [23, 114–116]. These GALs can also be described as an arrangement of nanoholes. Since in the case of GALs, the band gap depends on the size and separation of the nanoholes, they represent an interesting platform for band gap engineering in graphene. Experimentally, hints for the opening of such a band gap have been obtained for GNRs [117–119] as well as GALs [25], with most of the studies reporting a transport gap. The latter manifests itself by a high resistive region in the transport characteristics of the device, which is observable even if localized states exist inside the gap. Such localized states can originate from impurities or adsorbates and impart hopping conduction of charge carriers. In devices structured on Si/SiO_2 with standard lithography methods, impurities or adsorbates are easily introduced by resist residues from the patterning process, imperfections of the substrate, or contaminations adsorbed from the ambient onto the substrate or the device surface. Rough edges and varying ribbon width furthermore lead to so-called Coulomb blockade (CB) behavior. GNR devices [117, 120] have been reported to often behave like a series of quantum dots connected by tunneling barriers.

Part of this chapter was published in: A. J. M. Giesbers, E. C. Peters et al., Charge transport gap in graphene antidot lattices. Phys. Rev. B **86**, 045445 (2012) and E. C. Peters et al., Variable range hopping in graphene antidot lattices. Phys. Status Solidi B **249**, 2522 (2012).

Experiment

Here, we address the connection between the electronic structure and the geometry of the GALs by studying the AC and DC charge transport characteristics of samples with different arrangement, size and separation of the nanoholes, as well as different doping level. The GAL devices investigated consist of $d = 50\ nm$ diameter nanoholes with center-to-center spacings of $s = 80$, 100, or 200 nm in either a square or a hexagonal nanohole arrangement (figure 5.1). This corresponds to a spatial confinement ("neck width") of 30, 50, and 150 nm, respectively.

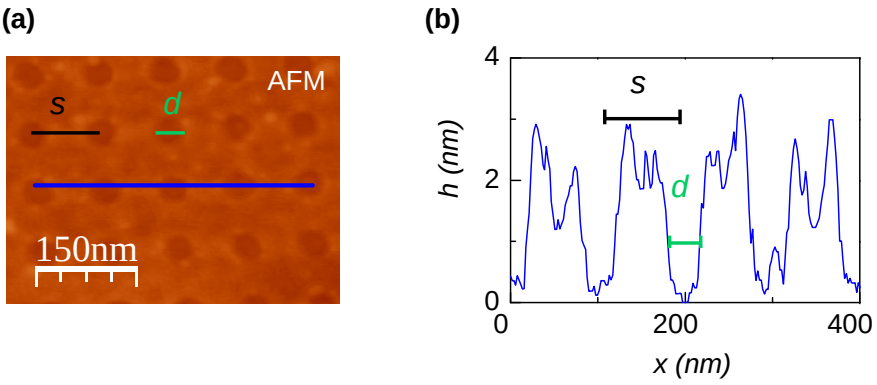

Figure 5.1: Atomic force microscopy (AFM) image of a GAL with nanoholes arranged in a square pattern. (a) The spacing between the nanoholes is $s = 100\ nm$ and their diameter is $d = 50\ nm$. (b) Height profile along the blue line in panel (a).

The measurements are performed with standard lock-in amplifier techniques at temperatures between 1.4 K and 100 K at low enough currents to prevent heating effects. A negligible bias voltage influence is confirmed in complementary DC measurements. In order to investigate doping effects, some of the samples are annealed in-situ under vacuum ($p \approx 1 \cdot 10^{-5}\ mbar$).
The influence of the nanohole pattern on the transport characteristics is investigated in section 5.1. Section 5.2 provides a closer look on localization and interaction effects of the system and the relevant length and energy scales are discussed. Moreover, the role of the sample quality and tuning of the charge carrier density by an external back gate is addressed in section 5.3.

Devices

The GAL devices are fabricated from mechanically exfoliated graphene (see chapter 3). Figure 5.2 shows a GAL device structured in four-terminal lateral geometry patterned with a square lattice of nanoholes with 100 nm spacing. As described in chapter 3, this device geometry offers the advantage of eliminating the contact resistance. The Cr/Au contacts are colorized yellow in the scanning electron micrograph (SEM) image. For patterning the

GAL devices, graphene flakes are mechanically exfoliated onto a Si substrate covered with 300 nm thick SiO_2 layer, as described in chapter 3. Details on the samples investigated in this thesis are provided in Appendix A. For four-terminal measurements, four Cr/Au (2/100 nm) electrical contacts are defined by standard EBL using a double layer PMMA resist. The etch mask for the antidot lattice is defined in the following EBL step. After the lift-off step, the exposed graphene is etched by RIE (see chapter 3). The samples, are designed to have similar flake sizes, the same contact material and positions, and the same antidot lattice dimensions, in order to minimize size effects. In general, samples fabricated on the same chip (undergoing the same treatment and processing) are compared in order to minimize variations due to the processing conditions.
To improve the sample quality, after completing all lithography steps some of the samples are annealed at 250°C in a furnace under Argon flow to remove surface contaminants. This shifts the CNP closer towards zero, although, due to subsequent exposure to the atmosphere, the final position of the CNP typically lies around 10 V to 20 V. This exposure to the ambient can be avoided if the sample is annealed in vacuum, already mounted in the cryostat insert. It also allows to compare the device behavior before and after annealing (see sample 9249_$D3a$/9249_$aD3a$ and 9249_$D2$/9249_$aD2$). The field-effect mobility of the GAL devices is found to reach values up to 5000 cm^2/Vs at 4 K even without annealing.

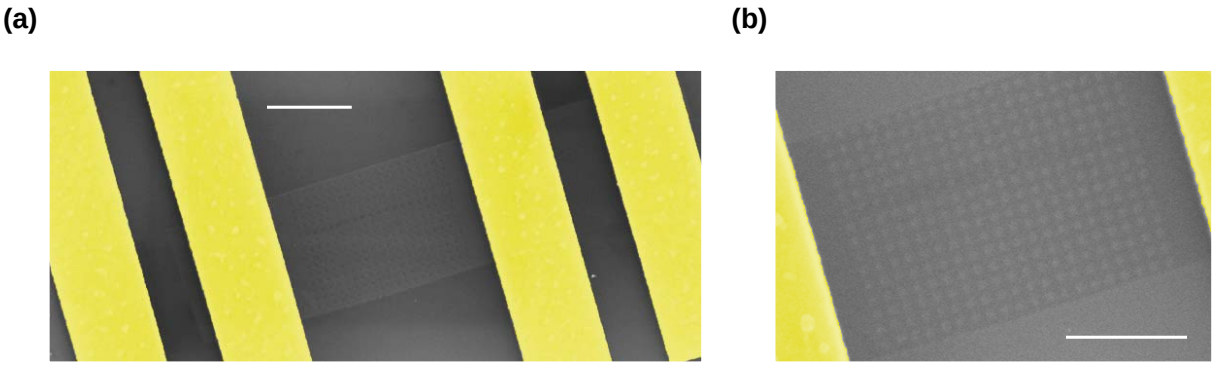

Figure 5.2: SEM image (a) and zoom (b) of a GAL device in lateral four-terminal geometry (metal contacts are colorized yellow). Typically, the GAL devices are patterned from exfoliated monolayer stripes a few micrometers wide and long. The scale bar is 1 μm.

5.1 Transport Behavior depending on Antidot Lattice Geometry

5.1.1 Transport Mechanisms

For pristine graphene, the transport characteristics are governed by the position of the CNP. Below this point, p-type conduction with holes as charge carriers occurs, while above the CNP n-type conduction with electrons as charge carriers dominates. In an idealized model, no charge carriers exist directly at the CNP, which would imply infinite resistivity. However, due to the formation of electron-hole puddles [62], electrons and holes coexist at the CNP and only the net charge is exactly zero. This leads to a finite resistance at the CNP, which has been found to be close to 4 e^2/h [29].

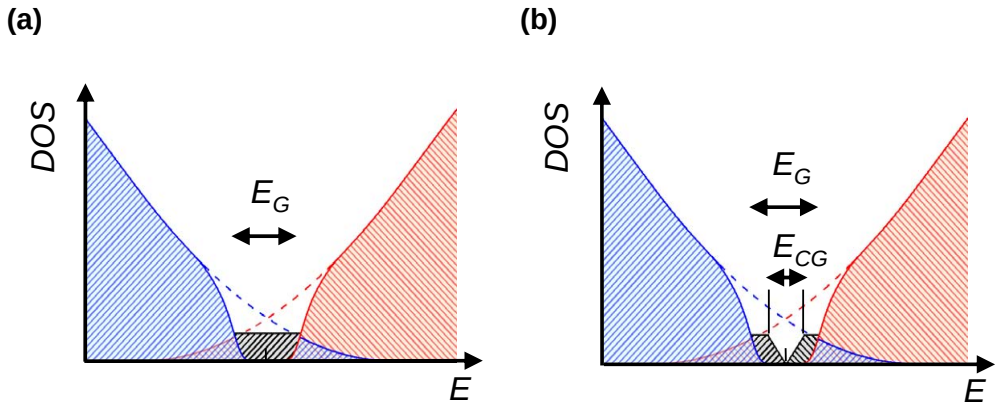

Figure 5.3: Schematic of different scenarios for the density of states (DOS). Blue represents the hole density of states and red the electrons density of states. The coexistence of charge carriers around the CNP ($E = 0$) is indicated by the tail of the DOS of the opposite charge carriers. The dashed lines indicate the DOS in case no gap is opened. (a) DOS for Mott VRH with a constant density of localized states (black) in the band gap E_G. (b) DOS for ES VRH with a Coulomb gap (CG) E_{CG} in the localized density of states.

Activated Transport

While pristine graphene is a semi-metal, opening of a band gap E_G transforms it into a semiconductor, and the charge transport can be described by models developed for doped semiconductors [121]. Accordingly, in order to contribute to conduction charge carriers need to be activated by the energy $e_A = T_0 k_B$ (k_B being the Boltzmann constant) to the nearest mobility edge of the conduction or valence band. This energy corresponds to half of the gap size E_A and is experimentally accessible via the temperature dependence of the

conductivity. The general law for the temperature-dependent conductivity is given as:

$$\sigma = \sigma_0 exp\left(-\left(\frac{T_0}{T}\right)^{\nu}\right) \tag{5.1}$$

with $\sigma_0 = e^2/h$ [121]. In case of a simple band gap, the exponent for activated transport is equal to $\nu = 1$ and the exponential law is the Arrhenius equation. For a simple band gap with electron conduction above the gap and hole conduction below the gap the DOS would be expected to increase linearly above and below the gap.

2D Mott Variable Range Hopping

As mentioned above, impurities and adsorbates may introduce localized states. These can contribute to the conduction by hopping of carriers from one localized state to the next. The simplest case is Mott variable range hopping (VRH), where the hopping probability between two hopping sites depends on their spatial and energetic separation, with negligible interactions between the charge carriers. Here, the density of the localized states in the band gap is constant (see figure 5.3(a)), and the exponent in equation 5.1 is given as $\nu = 1/(d+1)$, where d is the dimensionality of the system. In the case of two-dimensional ($2D$) transport in graphene, the exponent becomes $\nu = 1/3$. For $2D$ Mott VRH the hopping distance R_{hop} and energy E_{hop} [121–123] are given by:

$$R_{hop} = \frac{\xi}{3}\left(\frac{T_0}{T}\right)^{1/3} \tag{5.2}$$

and

$$E_{hop} = \frac{1}{3}T_0^{2/3}T^{1/3}. \tag{5.3}$$

In these equations

$$T_0 = T_0^M = 27/\pi g_0 \xi^2, \tag{5.4}$$

which contains the constant density of states g_0 and the localization length ξ.

Efros-Shklovskii Variable Range Hopping

Correlations between localized charge carriers are especially relevant for strong interactions and low temperatures. Due to the long-range nature of the Coulomb potential, the density of localized states vanishes around the Fermi level and a so-called Coulomb gap (CG) emerges in the single-particle constant density of localized states [121] (see figure 5.3(b)). Inclusion of electron-electron interactions changes the exponent in equation 5.1 to $\nu = 1/2$, and conduction is described by Efros-Shklovskii variable range hopping (ES VRH). In this case, the hopping distance and the hopping energy [121–123] are given by:

$$R_{hop} = \frac{\xi}{4}\left(\frac{T_0}{T}\right)^{1/2} \tag{5.5}$$

and

$$E_{hop} = \frac{1}{2} T_0^{1/2} T^{1/2}. \tag{5.6}$$

The localization length ξ can be derived directly from

$$T_0 = T_0^{ES} = \frac{\beta e^2}{4\pi\epsilon\epsilon_0 k_B \xi}, \tag{5.7}$$

where $\beta = 2.8$ is a constant [121], ϵ_0 is the vacuum permittivity and $\epsilon = 2.4$ is the dielectric constant of graphene on SiO_2 [124]. The Coulomb gap (CG) can be calculated from:

$$E_{CG} = \frac{T_0}{\beta\sqrt{4\pi}}. \tag{5.8}$$

5.1.2 Temperature dependence

Figure 5.4(a) shows the gate voltage dependent conductivity around the CNP of a GAL sample with 100 nm spacing for temperatures between $T = 1.4\ K$ and $T = 70\ K$.

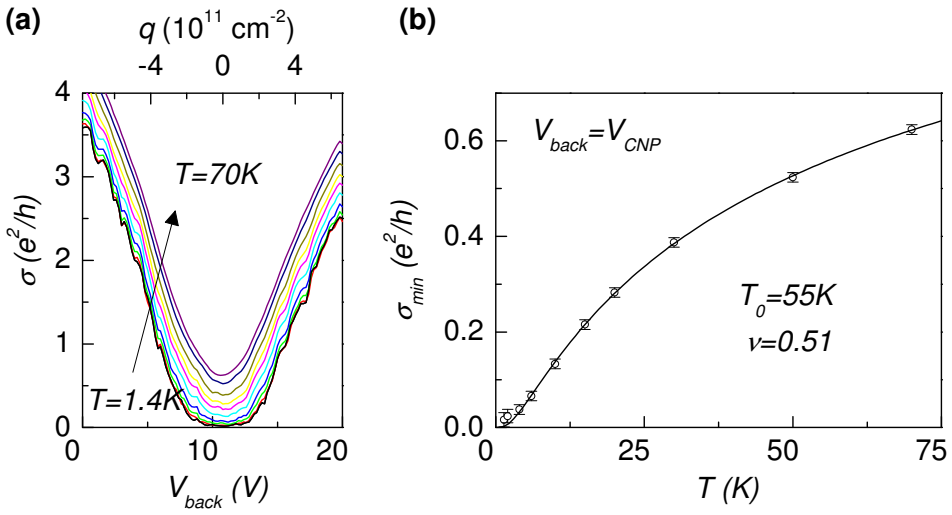

Figure 5.4: Temperature dependent conductivity of a 100 nm spacing sample (8855_$D1$). (a) In the gate-sweeps between $T = 1.4\ K$ and $T = 70\ K$, a gap opens around the CNP for low temperatures. The gate coupling factor is $7.2 \cdot 10^{10}\ V^{-1}cm^{-2}$. (b) The minimum conductivity shown in panel a) is fitted with equation 5.1. The fit parameters for this sample are $T_0 = 55 \pm 7\ K$ and $\nu = 0.51 \pm 0.02$. σ_0 is close to 1 e^2/h.

The net charge carrier density is adjusted by varying the back gate voltage V_{back} and corresponds to $q = \alpha(V_{back} - V_{CNP})$ with the gate coupling factor α, which is about $7 \cdot 10^{10}\ V^{-1}cm^{-2}$ for pristine graphene on Si/SiO_2 with a 300 nm oxide layer [29]. Around the CNP, for this sample located at $V_{CNP} = 10.6\ V$, the conductivity closely approaches

zero at the lowest temperatures in contrast to $\sigma \approx 4\ e^2/h$ for pristine graphene, which indicates the presence of a transport gap [25, 114–116]. In order to analyze the transport mechanism the temperature dependence at the CNP can be fitted with equation 5.1 as shown in figure 5.4(b).

Dependence on the GAL geometry

For GALs with large spacing (200 nm), the temperature dependent minimum conductivity reveals a $ln(\sigma) \propto T^{-1/3}$ dependence with an average exponent of $\nu = 0.26 \pm 0.03$, pointing towards 2D Mott VRH (exponent $\nu = 1/3$) in these samples.
Upon decreasing the lattice spacing, the temperature dependence of the minimum conductivity changes to $ln(\sigma) \propto T^{-1/2}$. The average exponent is $\nu = 0.50 \pm 0.04$ and $\nu = 0.47 \pm 0.04$ for samples with 100 nm and 80 nm nanohole spacing, respectively. This change from $\nu = 1/3$ to $\nu = 1/2$ indicates a transition to ES VRH [121] and signifies enhanced electron-electron interactions. The increased exchange energy can be explained by a smaller separation of the localized states and correspondingly increased overlap of the wave functions. These states are most likely located at the nanohole edges [115, 121].

5.1.3 I/V Curves

Complementary to the AC measurements, DC measurements are performed on the GALs.

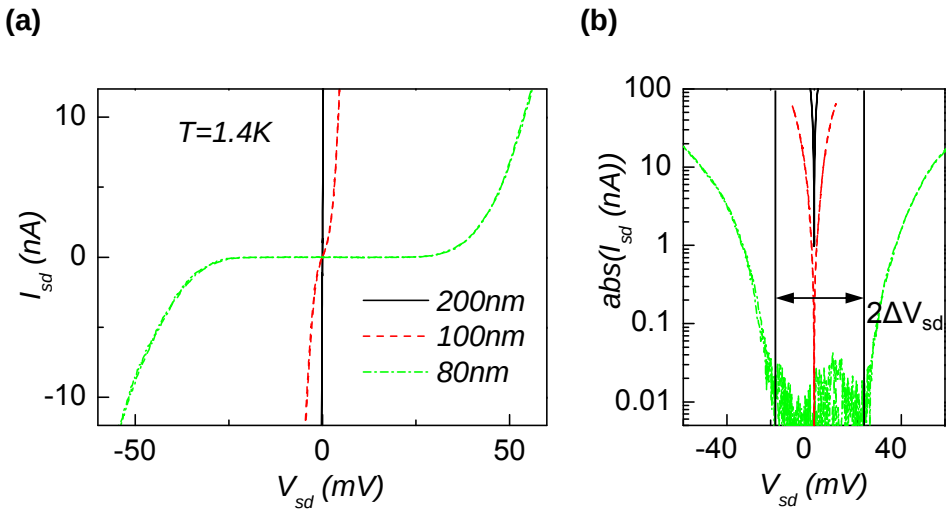

Figure 5.5: I/V curves for different lattice geometries. (a) I/V curves at the CNP of sample 8855_$D2b$ (200 nm spacing), 8855_$D1$ (100 nm spacing) and 8854_$D3a$ (80 nm spacing) at $T = 1.4\ K$. (b) Plots of the absolute current on a logarithmic scale show a variation over 5 orders of magnitude and a zero conductance plateau around the CNP. The width of the plateau increases with decreasing spacing.

In figure 5.5 I/V curves for samples with different lattice spacings are shown. The transport gap is reflected by a zero-bias plateau, which is wider for smaller nanohole spacing. In fact, for small lattice spacing, the zero-bias conductance of the samples decreases and the plateau flattens out and broadens. Similar observations have been made on GNRs [119]. For pristine graphene the I/V characteristics are linear even for samples of low quality, where regions of different doping are likely to introduce pn-junctions. This can be explained by the fact that transport across pn-junctions in graphene is not impeded due to Klein tunneling [47].
The width of the plateau in the I/V curves ($2\Delta V_{sd}$) can be used to estimate the size of the transport gap $E_G = e2\Delta V_{sd}$ as exemplified for the 80 nm spacing sample by the logarithmic plot in figure 5.5b). At $T = 1.4\ K$, this yields an approximate gap size of $E_G = 29\ K$ ($2.5\ meV$) and $E_G = 394\ K$ ($34\ meV$) for the 100 nm and 80 nm spacing samples, respectively.
The DC measurements furthermore confirm that bias voltage effects are negligible since similar results are obtained for the temperature dependent low-bias conductivity at the CNP as in the AC measurements. The temperature dependence of the I/V curves is exemplified by sample 8855_$D1$ (100_nm spacing) in figure 5.6(a). With decreasing temperature (figure 5.6(a)), the plateau becomes more pronounced. The temperature dependent conductivity at the CNP exhibits the same exponential increase as in the AC measurements (with $\nu = 0.49$ and $T_0 = 63\ K$), and yields an exponent of $\nu = 0.48$ and $T_0 = 58\ K$ for this sample (figure 5.6(b)).

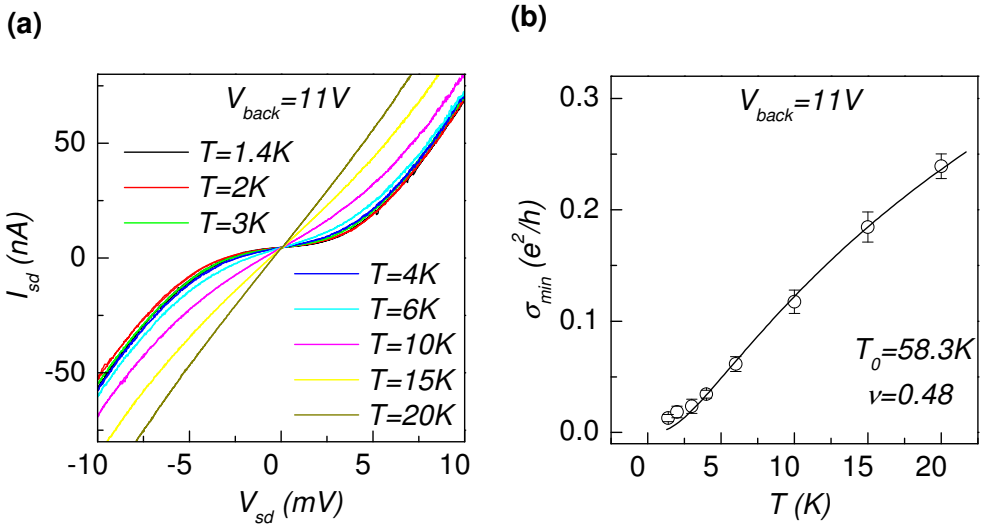

Figure 5.6: Temperature dependence of the I/V curves. (a) I/V curves at the CNP for different temperatures of sample 8855_$D1$ (100 nm spacing) at different temperatures. (b) Fit of equation 5.1 to the conductance derived from the I/V curves in panel (a) at low bias voltage. The obtained fit parameters are $T_0 = 58 \pm 10\ K$ and $\nu = 0.48 \pm 0.03$, while σ_0 is close to 1.

5.2 Variable Range Hopping Regimes

As shown above (see section 5.1), the transport mechanism, as determined from the temperature dependent resistance behavior, depends on the GAL dimension. It changes from 2D Mott VRH (with an exponent close to $\nu = 1/3$) for large lattice spacing to ES VRH (with an exponent close to $\nu = 1/2$) for smaller lattice spacing. This trend is reasonable considering that placing the nanoholes closer together should enhance the Coulomb interactions such that a Coulomb gap appears in the localized density of states, which increases further with decreasing lattice spacing. It is noteworthy that a similar transition has been documented for graphene covalently functionalized with fluorine [125], albeit the functionalization pattern is quite likely more random compared to the present samples. In fluorinated graphene, charge transport was found to occur via ES-VRH at higher functionalization degrees (equivalent to a high density of localized states), whereas at lower fluorine content the transport was dominated by Mott-VRH. Such transition is in accordance with theory predicting that for lower densities of localized states, the average hopping distance increases, and correspondingly the Coulomb gap becomes less relevant and a constant density of states, g_0, prevails [123, 125].

Derived VRH Parameters

The fit parameters gained from the temperature dependent measurements provide additional information such as the hopping distance R_{hop} and energy E_{hop} (equations 5.3 and 5.5-5.7), the localization length ξ (equation 5.7) and the Coulomb gap size E_{CG} (equation 5.8).

Spacing (nm)	ν Regime	T_0 (K)	ξ (nm)	E_{CG} (K) (meV)	E_{hop} (K) (meV)	R_{hop} (nm)
80	0.47 ± 0.04	360	54	36.4	30.0	81
	ES VRH			3.1	2.6	
100	0.50 ± 0.04	50	345	7.4	13.1	199
	ES VRH			0.64	1.1	
200	0.26 ± 0.03	0.5	$g_0\xi^2 = 17\ K^{-1}$	-	1.2	
	Mott VRH			-	0.1	
no dots	-	-	-	-	-	-

Table 5.1: Average VRH parameters derived from the AC measurements for GALs with different lattice dimensions. The hopping energies and distances are calculated for $T = 10\ K$.

Table 5.1 summarizes the average values of these parameters for different GAL geometries, as well as for pristine graphene. For the calculation of the localization length a dielectric constant of $\epsilon = 2.4$ for graphene on SiO_2 [124] is assumed.

Localization and Exchange Interactions

A closer look at the parameters in dependence of the GAL geometry underscores the transition from weaker to stronger localization and enhanced exchange interactions with decreasing nanohole spacing:
For the nanohole spacing of 200 nm the product of $g_0\xi^2$ is calculated using equation 5.4 to be 17.2 K^{-1}. Since the Coulomb interactions between charge carriers are weak in this regime, the DOS of the localized states is constant and no Coulomb gap is formed. Hence, hopping between the weakly interacting localized states occurs with a low hopping energy of $E_{hop} = 1.2\ K$ (0.1 meV) at $T = 10\ K$.
It is apparent from the fit parameters in table 5.1 that reducing the nanohole spacing leads to a strong increase in T_0 and therefore a decrease in the product $\epsilon\xi$. This change suggests a corresponding decrease of either the dielectric constant or the localization length, or both. If one assumes ϵ to be constant (like in table 5.1), it follows that the localization length is affected by the GAL density. Comparison of the localization length for the 100 nm and 80 nm spacing samples reveals that by decreasing the lattice spacing, the localization length decreases, which corresponds to stronger localization. Specifically, the obtained values for the localization length are $\xi = 345\ nm$ and $\xi = 54\ nm$ for the 100 nm and 80 nm spacing samples, respectively. The stronger localization also influences the hopping energy which is larger compared to the case of 200 nm nanohole spacing ($E_{hop} = 1.2\ K$ (0.1 meV)),as reflected by the values of $E_{hop} = 13.1\ K$ (1.1 meV) and $E_{hop} = 30.0\ K$ (2.6 meV) for samples with 100 nm and 80 nm spacing, respectively, at $T = 10\ K$. With the increase of the hopping energy, the hopping distance decreases from $R_{hop} = 199\ nm$ (100 nm spacing) to $R_{hop} = 81\ nm$ (80 nm spacing) at $T = 10\ K$. This can be expected since with decreased lattice spacing, the localized states at the nanohole edges move closer together. It is noteworthy that in the temperature region used for calculating the hopping distances and energies, R_{hop} equals once to twice the respective nanohole separation. This implies that charge carriers can hop from one nanohole edge to the edge of the nearest or next-nearest nanohole. With decreasing temperature, the hopping energy increases while the hopping distance decreases, similar to the effect of decreased lattice spacing. With increasing localization, the CG increases from $E_{CG} = 7.4\ K$ (0.6 meV) for 100 nm spacing to $E_{CG} = 36\ K$ (3.1 meV) for 80 nm spacing, owing to increased Coulomb interactions in the latter type of GALs. The CG emerges as a linear gap [126] in the localized density of states between the two mobility edges at the border of the transport gap (see section 5.3). Here, the minimum of the localized density of states, which marks the position of the CG, is defined to be always located at the Fermi energy.
Sample-to-sample variations in the obtained values, especially of T_0, can be ascribed to small differences in the nanohole dimensions such as a slightly higher or lower andidot diameter due to the non-ideal graphene etching step and different degrees of unintentional chemical functionalization of the nanohole edges. As T_0 assumes values between 33 K and 140 K for different 100 nm spacing samples, this leads to a localization length between 139 nm and 591 nm, and a CG between 14.1 K and 3.3 K. Also the extend of surface doping influences the T_0 value, as described in more detail in section 5.3.

From the data in table 5.1, it follows that with increasing nanohole spacing the localization strength is reduced, thus inducing a transition from ES VRH to Mott VRH. For antidot spacings larger than 200 nm the interactions might become even less important and accordingly the transport behavior change from strong (ES VRH followed by Mott VRH) to weak localization.

5.3 Influence of charge carrier density and sample quality

Due to residues from the sample fabrication, mainly e-beam resist, as well as adsorbates from the ambient, the CNP of as-fabricated devices is usually not positioned at $V_g = 0\ V$, but shifted toward positive back gate voltages. This results from residues or adsorbates as well as defects in the SiO_2 surface that trap charges near the graphene, which leads to doping of the device. At the same time, there is a broadening of the gate sweep characteristic, which is a measure for the quality of the graphene sheet. The mobility of the charge carriers is reduced due to increased scattering by the trapped charges. The present GAL devices exhibit only small shifts of the CNP to between 10 V and 20 V, which is indicative of a low doping concentration of trapped charges. Nonetheless, this doping affects the VRH. The trapped charges screen the localized states and thus decrease the CG due to weaker localization. In figure 5.7 the CG size is plotted for different samples with varying CNP positions for devices with 100 nm nanohole spacing. It can be seen that the localization is stronger for samples with the CNP close to 0 V. In these devices, the CG is large compared to devices with high CNP positions. For GALs with a CNP at even higher back gate voltages, localization should become even weaker, thus promoting a transition to the weak localization regime for sufficiently high doping levels [25].

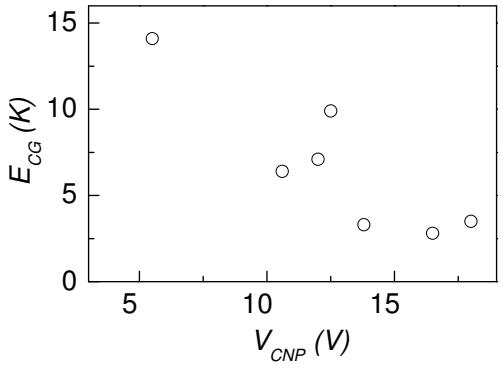

Figure 5.7: Dependence of the CG size on the CNP position of the sample. Data of different 100 nm spacing samples (8855_$D1$, 8855_$D4$, 8817_$D5$, 8817_$D4$, 9249_$D3a$, 9249_$aD3a$, 8854_$D1$) is shown.

The influence of the doping level is also apparent upon annealing of the device, whereupon the CNP shifts to lower back gate voltages. Likewise, an applied back gate voltage reduces localization and causes a transition to the weak localization regime due to screening by the induced charge carriers. In the following section this behavior is described in more detail.

5.3.1 Annealing

In situ thermal annealing of the samples enables determining their properties as a function of the CNP position. For this purpose, devices are annealed at 125° C insitu under vacuum ($p \approx 1 \cdot 10^{-5}$ $mbar$) for several hours. Figure 5.8(a) shows the shift of the CNP of a 100 nm and 200 nm spacing sample, respectively. This shift is accompanied by a narrowing of the gate sweep curve indicating a mobility increase due to the removed surface contaminants. The evolution of the resistance at zero gate voltage during annealing process of the 100 nm spacing device is plotted in panel (b). The observed resistance increase is due to the CNP shift from initially $V_{CNP} = 12.5\ V$ to $V_{CNP} = 5.5\ V$.

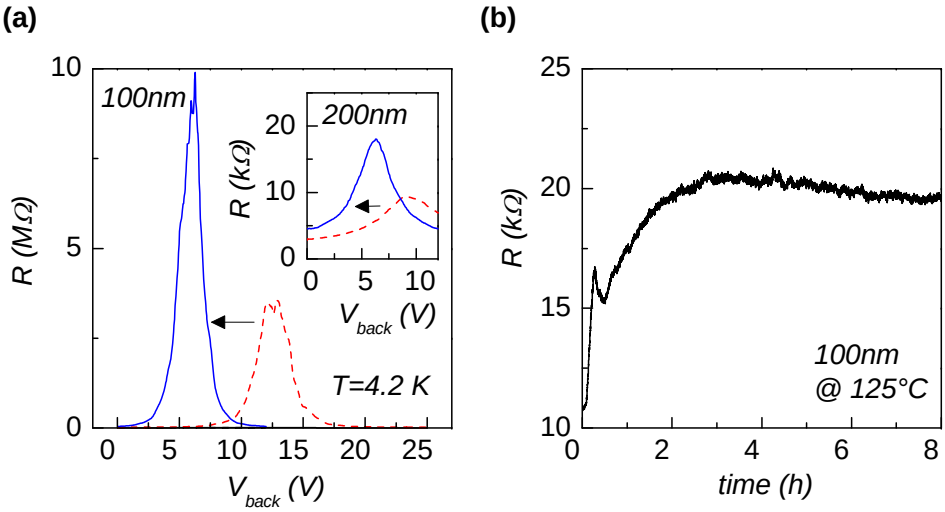

Figure 5.8: Effect of annealing at 125° C in vacuum. (a) Annealing at this temperature removes adsorbed water, thus shifting the CNP of sample 9249_$D3a$ (100 nm spacing) from 12.5 V to 5.5 V, and of sample 9249_$D2$ (200 nm spacing; inset) from 8.5 V to 5.5 V. (b) Resistance measured at $V_{back} = 0\ V$ of sample 9249_$D3a$ during the annealing process.

Additionally to the CNP shift and narrowing of the Dirac peak, the annealed GAL devices exhibit a strong increase of the maximum resistance. Furthermore, there is a strong increase in T_0, implying a decrease in ξ and thus stronger localization. This, in turn, leads to an enhanced CG, which increases from $E_{CG} = 9.9\ K$ ($0.85\ meV$) to $E_{CG} = 14.1\ K$ ($1.22\ meV$) for the 100 nm sample. Along with the dependence of the CG on the CNP position of the different samples (figure 5.7), this observation evidences that the unintentional doping has a profound influence on the localization strength and Coulomb interactions in the devices.

With an increased amount of surface contaminants, the localization strength decreases, and it can be expected that for highly doped GALs [25] weak localization behavior emerges instead of strongly localized VRH.

5.3.2 Influence of Back Gate

Besides the comparison of devices with different CNP position, or samples before and after annealing, the influence of an increased charge carrier density can be studied via the field effect by application of a back gate voltage. Back gate voltage and charge carrier density are related to each other via the gate coupling factor α: $q = \alpha V_b$ ($V = V_{back} - V_{CNP}$). Figure 5.9 shows I/V curves of sample 8855_D1 (100 nm spacing) in dependence of the gate-induced charge carrier density. Similarly to an increase in temperature or a decrease in nanohole spacing, with increasing charge carrier density the zero bias plateau becomes less pronounced and the curves approach ohmic behavior. At the CNP the measured transport gap is largest and ES VRH is present in the shown 100 nm spacing sample. Outside the center of the gap region (i.e. away from $V_{CNP} = 10.6\ V$), the measured gap becomes smaller.

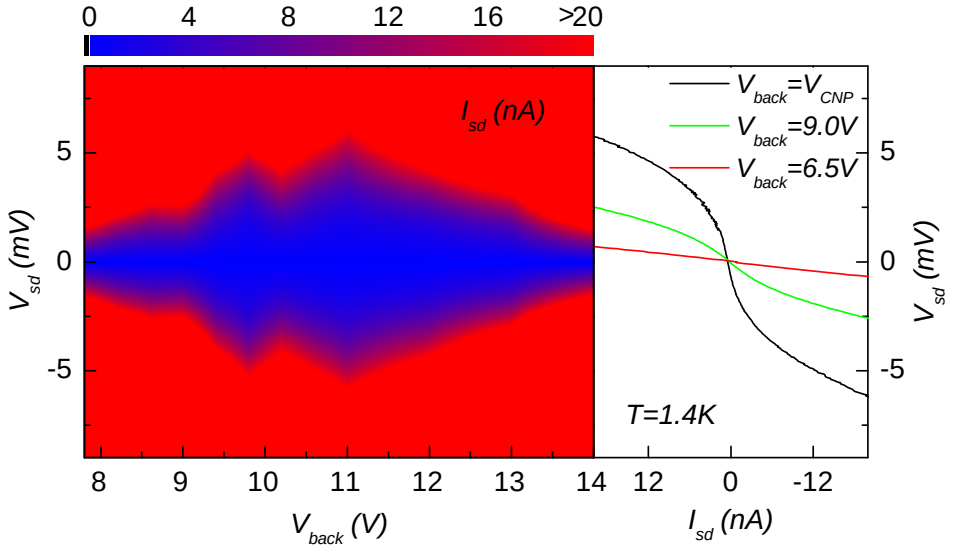

Figure 5.9: Gate dependence of the I/V curves. The color plot shows the absolute current (in nA) of sample 8855_D1 (100 nm spacing) as a function of gate voltage and source-drain voltage. Line-cuts at gate voltages $V_{back} = V_{CNP}$, $V_{back} = 9.0\ V$, $V_{back} = 6.5\ V$ are plotted in the graph on the right.

In figure 5.10(a), the CG for the same 100 nm spacing sample, derived from the temperature dependence of conductivity, is plotted as a function of charge carrier density. Around the CNP (at zero net charge carrier density) the measured size of the CG is largest and decreases linearly with increasing positive or negative charge carrier density. This decrease

can again be ascribed to enhanced screening of the localized states and a resulting smaller overlap of the wave functions of the localized states, leading to weakened exchange interactions. At moderate concentrations of $|q| \approx 2 \cdot 10^{11}\ cm^{-2}$ the CG reaches a value of $E_{CG} \approx 2\ K$ ($0.17\ meV$). Above this concentration the CG is no longer important, and the exponent (equation 5.1) changes from 1/2 to 1/3, indicating the transition from ES VRH to Mott VRH without Coulomb interactions [121]. At even higher concentrations, the localization length decreases further. The dependence of T_0 and the localization length on q are plotted in panel (b) of figure 5.10.

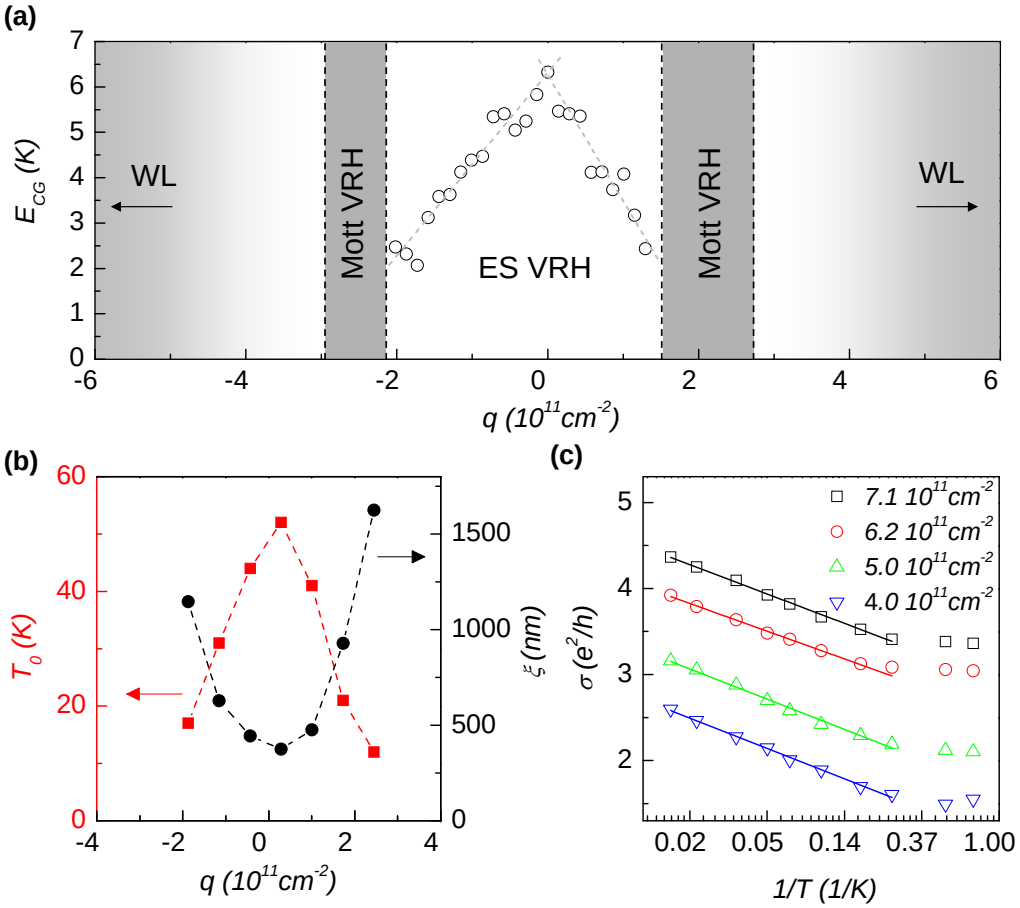

Figure 5.10: Influence of an applied back gate voltage on the temperature dependence. (a) Coulomb gap for sample 8855_$D1$ (100 nm spacing) at different densities. For low concentrations charge transport is via ES VRH is the transport regime. In the higher concentration range of $-2.3 \cdot 10^{11}\ cm^{-2} < q < -3 \cdot 10^{11}\ cm^{-2}$ and $1.6 \cdot 10^{11}\ cm^{-2} < q < 2.7 \cdot 10^{11}\ cm^{-2}$ the transport regime changes to Mott VRH and at even higher concentrations $4 \cdot 10^{11}\ cm^{-2}$ ($|q| > 4 \cdot 10^{11}\ cm^{-2}$) the device exhibits weak localization behavior. (b) Fit parameter T_0 and localization length ξ of sample 8855_$D1$ (100 nm spacing) around the CNP. The gate coupling factor is $7.2 \cdot 10^{10}\ V^{-1}cm^{-2}$. (c) Weak localization fits at high carrier densities.

The above findings demonstrate that ES VRH can only be observed at low temperatures, high GAL densities and low charge carrier concentrations. At highest charge carrier concentrations ($|n| > 4 \cdot 10^{11}\ cm^{-2}$), the temperature dependence of conductivity no longer follows an exponential behavior (equation 5.1). It rather displays a logarithmic dependence, which is characteristic of weak localization in 2D [127]:

$$\sigma_{WL} = -\frac{p}{\pi} ln\left(\frac{T_0^{WL}}{T}\right) \tag{5.9}$$

Here it should be mentioned that outside the WL regime, electron-electron interactions can also lead to a logarithmic dependence on temperature [128].
In the pre-factor of the logarithmic function in equation 5.9, p is the temperature exponent for the (inverse) phase coherence time (phase breaking rate) in the following equation:

$$\tau_\phi^{-1} = \alpha T^p. \tag{5.10}$$

Here, α is a constant and the exponent p is of the order of unity [127]. The phase coherence length L_ϕ is connected to the phase coherence time via the diffusion constant D:

$$L_\phi^2 = D\tau_\phi. \tag{5.11}$$

Furthermore, the following equation holds:

$$T_0^{WL} = (D/\alpha l^2)^{1/p}, \tag{5.12}$$

where l is the charge carrier mean free path.
Figure 5.10(c) shows the weak localization behavior at high charge carrier concentrations. For concentrations above $|q| > 4 \cdot 10^{11}\ cm^{-2}$, the T_0 vs. $1/T$ curves can be reasonably well fitted with equation 5.9. For the exponent p, this yields $p = 1.07 \pm 0.07$, from which the temperature dependence of the phase coherence length $L_\phi \propto \tau^{1/2} \propto T^{-0.5}$ follows. This dependency is in good agreement with reports on graphene [129] and heavily doped GALs [25]. At the lowest temperatures (see figure 5.10(c) for $T < 4\ K$), there is a small deviation from the weak localization behavior, which can be attributed to the onset of VRH.

Chapter 6

Variable Range Hopping in Magnetic Field

Introduction

As described in the previous chapter, patterning of graphene into GALs imparts a transport gap and different regimes of hopping conduction, with weaker or stronger localization depending on the GAL dimensions. Correspondingly, especially in magnetic fields GALs are expected to exhibit a wide range of intricate properties similar to two-dimensional electron gases (2DEGs) defined within semiconductor heterostructures. For the latter, interaction effects are well-documented to be influenced by magnetic fields involving a change of the VRH parameters and crossover between different hopping mechanisms [121]. In magnetic fields, competing length scales such as the magnetic length, the localization length and the phase coherence length, lead to extremely rich physics. As the wave functions of the charge carriers shrink in an applied magnetic field (decreasing magnetic length), magnetoresistance effects can be observed even in pristine graphene [130] due to the existence of electron-hole puddles [62]. In general, the theoretically predicted magnetic field dependent hopping probability of charge carriers [131] gives rise to quantum interference effects in the VRH or weak localization regime, which lead to a resistance correction. Such correction is usually necessary in the weak localization regime to account for the observation of a negative magnetoresistance [132]. The situation is similar for the VRH regime [133, 134]. Outside the VRH regime, interference between different conduction paths leads to Aharanov-Bohm type (AB) oscillations in the magnetoresistance, as has been observed for graphene ring structures [135] and graphene antidot lattices on SiC [136], where a phase difference is accommodated between the charge carriers traveling along the different paths. The Quantum Hall Effect (QHE) emerges upon condensation of the charge carrier density of states into Landau levels, in a manner that depends on the charge carrier quasi-particle properties (see chapter 2). In samples of extremely high mobility, where charge carrier transport approaches the ballistic regime, additional effects are expected upon introduction of an an-

Part of this chapter was published in: A. J. M. Giesbers, E. C. Peters et al., Charge transport gap in graphene antidot lattices. Phys. Rev. B **86**, 045445 (2012).

tidot lattice. Specifically, in high mobility GaAs/AlGaAs antidot lattices [137] anomalous low-field plateaus have been observed.

Experiment and Samples

Here, we analyze the influence of an external magnetic field on the charge transport mechanism in the GAL structures (section 6.1). In section 6.2 the magnetoresistance behavior of the GALs is evaluated for low to intermediate magnetic fields up to 12 T. Commensurability effects are investigated in in dependence of the applied back gate voltage section 6.3 and the relevant length scales in the respective magnetic field regions are derived.
For the experiments under magnetic fields, the same samples as for the zero-magnetic field measurements (chapter 5) are used, with typical lateral dimensions of a few micrometers in length and width (see figure 5.2). In order to evaluate the charge transport mechanism, the temperature dependence of the conductance is measured as a function of applied back gate voltage up to $B = 12\ T$ in the same temperature range as for the zero-magnetic field measurements ($T = 1.4\ K$ to $T = 100\ K$). To investigate magnetoresistance effects, the device is kept at constant charge carrier density and temperature, while sweeping the magnetic field.

6.1 Transport Characteristics under Magnetic Field

6.1.1 Magnetotransport behavior

Just as for zero magnetic field, the zero-conductance plateau of the I/V characteristic is most pronounced for smallest nanohole spacing. Figure 6.1(a) compares I/V curves of sample 8854_$D3a$ with and without applied magnetic field. In the low field range, the plateau becomes smaller with rising magnetic field and increases again above $B = 6\ T$. Above this strength, in the high field region the slope of the I/V curves (outside the plateau regions) steepens. This behavior is best visible when the current is plotted on a logarithmic scale (inset of figure 6.1(a)).
A similar behavior is displayed by the AC conductivity of the devices. Figure 6.1(b) shows gate voltage sweeps of a 100 nm spacing sample under magnetic field at $T = 1.4\ K$. Without B-field, the conductance is close to zero around the CNP due to the transport gap caused by the antidot lattice. For high enough magnetic fields, the usual quantized conductance plateaus appear. In the shown gate sweeps for fields from $B = 6\ T$ to $B = 12\ T$, the first plateau $\sigma = 2\ e^2/h$ occurs at filling factor $\nu = 2$. With increasing magnetic field the plateau in the gate sweeps first becomes narrower, but then broadens with increasing magnetic field above $B = 6\ T$. This behavior reflects the interplay of competing mechanisms. On the one hand the magnetic field changes the localization strength and the data indicate a change in the hopping conduction in the low magnetic field range, which will be the topic in this chapter, but the magnetic field also has a strong influence on the gap size itself leading to a different transport mechanism in the high field region which will be the topic of chapter 7. When the device is brought into the Quantum

Hall (QH) regime, the transport is governed by edge channel conduction. Both factors are especially relevant for very high fields, which will be the subject of chapter 7.

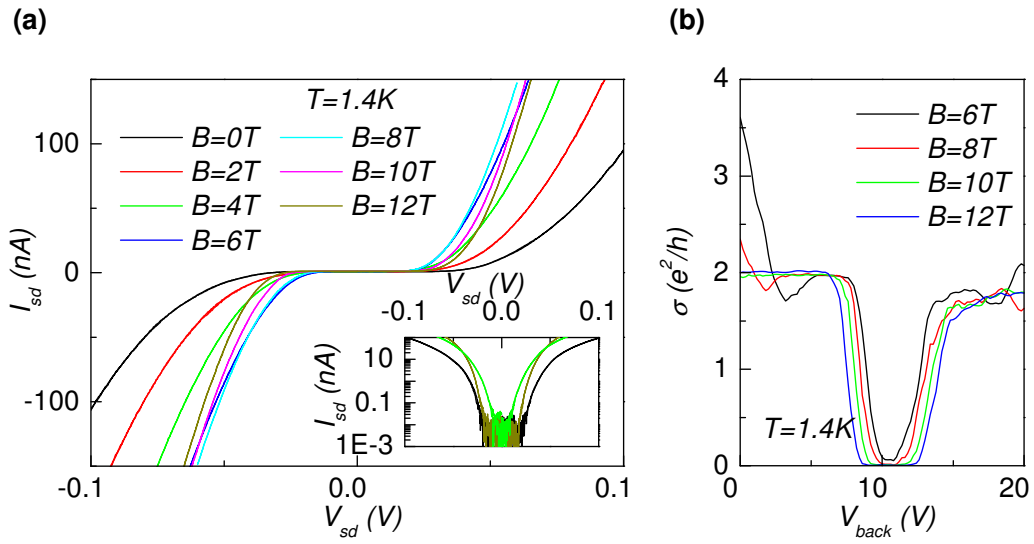

Figure 6.1: B-field dependence of gate sweeps and I/V curves. (a) I/V curves of sample 8854_$D3a$ (80 nm spacing) in dependence of an applied magnetic field. The inset shows selected I/V curves from the main panel on a logarithmic scale. (b) Gate sweeps of conductivity of a 100 nm spacing sample (8855_$D1$) at different magnetic fields.

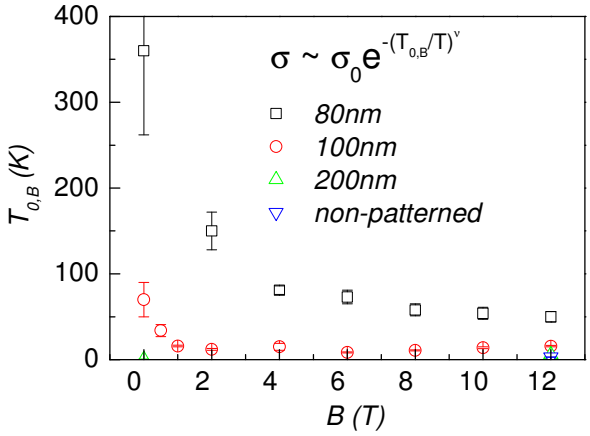

Figure 6.2: Fit parameter $T_{0,B}$ as a function of magnetic field for samples of different spacing: 80 nm (sample 8854_$D3a$), 100 nm (sample 8854_$D1$), 200 nm (sample 8855_$D2b$) and pristine graphene sample 8855_$D2a$.

The conductivity at the CNP at different temperatures can be fitted with equation 5.1

analogous to the analysis in the previous chapter. Thus obtained parameter $T_{0,B}$ for samples with different GAL spacings is displayed in figure 6.2. For all GAL devices, $T_{0,B}$ decreases with increasing magnetic field in the low field range ($B <\approx 6\ T$ for 100 nm spacing samples). Since $T_{0,B}$ is directly coupled to the localization length (equations 5.4 and 5.7), this trend hints toward weakening of the localization strength with magnetic field, similar to the effect of increased lattice spacing or increased charge carrier density. Thus, for the high nanohole density GALs, a transition from ES to Mott VRH can be expected. In order to validate this assertion, the exponent in the exponential temperature dependence has to be evaluated in detail.

6.1.2 Hopping Regimes

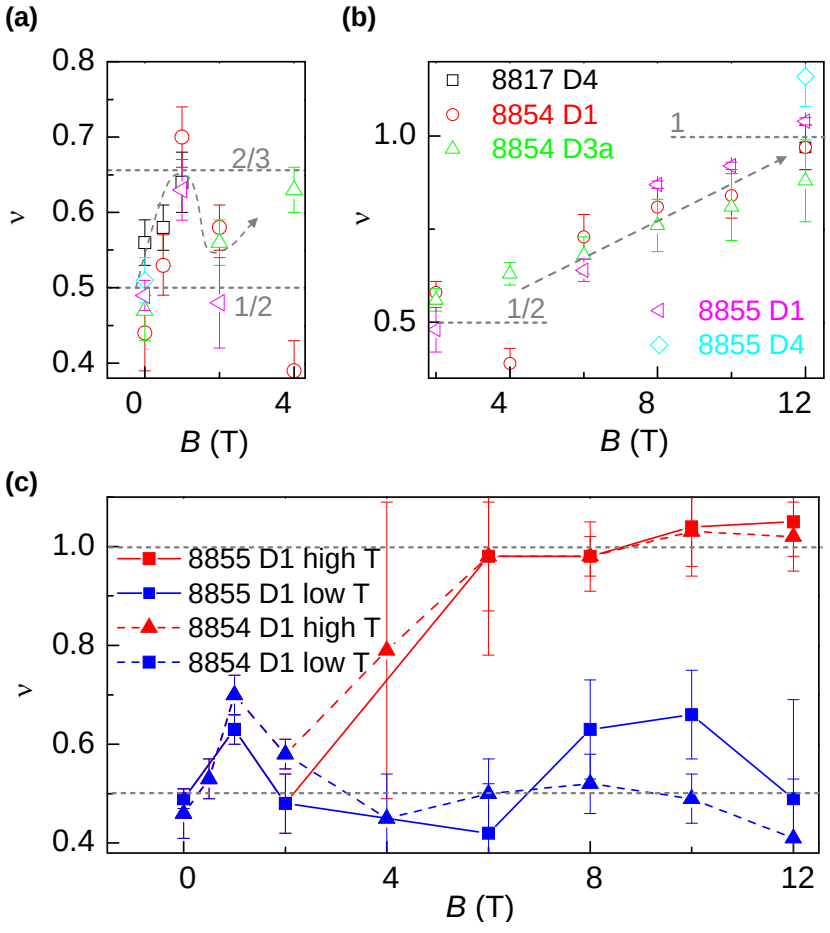

Figure 6.3: B-dependence of the exponent. All of the shown devices are GAL samples with 100 nm spacing. (a) Development of the exponent in the low field range. (b) Transition from Mott VRH to activated transport at higher fields. (c) Low (blue) and high (red) temperature regime fits.

For samples of high nanohole density the relevant charge transport mechanism is ES VRH, where Coulomb interactions lead to a soft gap, the Coulomb gap, in the localized density of states. This conduction type is preserved upon application of magnetic fields up to $B \approx 1\,T$, as concluded from the exponent of the exponential temperature dependence being close to 1/2. In figure 6.3 the exponent obtained from the fits is plotted as a function of magnetic field for different 100 nm spacing samples.

ES VRH in magnetic field

Starting from a value around 1/2 the exponent initially rises to 2/3 before decreasing back to 1/2 (figure 6.3a)). That at higher magnetic fields ($>$ 2 Tesla) the exponent of $\nu = 1/2$ is resumed is characteristic of VRH in 2D systems, and has been commonly ascribed to a transition from ES-VRH to Mott-VRH [123, 138–140], since for 2D Mott VRH under magnetic field the exponent is also expected to be 1/2. The intermediate value of 2/3, however, has not yet been observed before. Theoretically, such a value is predicted by percolation theory applied to ES-VRH within a 2D system [138]. According to this theory, the conductivity under magnetic field is given by [138]:

$$\sigma = \sigma_0 exp\left(-\left(\frac{T_{0,B}}{T}\right)^{\frac{2}{3}}\right), \tag{6.1}$$

with the parameter:

$$T_{0,B} = T_{0,B}^{ES} = te^2/4\pi\epsilon_0\epsilon k_B l_B. \tag{6.2}$$

In the latter equation, t is a constant. If the dielectric constant is assumed to be magnetic field independent, $T_{0,B}$ only depends on the magnetic length defined as:

$$l_B = \sqrt{\hbar/eB}. \tag{6.3}$$

The most likely reason why the transition to the intermediate exponent for ES VRH in magnetic field could not be observed in charge transport studies of semiconductor 2DEGs is the predominance of the Mott VRH regime under magnetic field [121, 139, 140]. Fitting equation 6.1 in the relevant magnetic field range ($B \approx 1\ T$ for the 100 nm spacing samples) yields small $T_{0,B}$ values compared to the zero-field T_0 (figure 6.2). Specifically, $T_{0,B}$ is around 17 K for the 100 nm samples, and approximately 81 K for 80 nm spacing, where an exponent close to 2/3 is reached at 4 T.
Alternatively, in equation 6.1 the temperature can be fixed so that the conductivity becomes a function of the magnetic field instead of the temperature. Fitting this equation in the magnetic field range of 0.5 to 1.5 Tesla at a constant temperature of $T = 1.4\ K$ reveals that the logarithm of the conductance depends linearly on $B^{1/3}$ ($ln(\sigma) \propto B^{1/3}$), verifying the exponent of $\nu = 2/3$ in equation 6.1. The fit further yields $T_{0,B} \approx 16\ K$ for 100 nm spacing in very good agreement with the values obtained from the fits of the temperature dependent data.

Magnetic field-induced crossover from ES to Mott VRH

The crossover from ES to Mott VRH in magnetic field

$$\sigma = \sigma_0 exp\left(-\left(\frac{T_{0,B}^{Mott}}{T}\right)^{1/2}\right), \tag{6.4}$$

is a direct consequence of shrinking of the wavefunction of the localized states, which reduces their overlap and hence the Coulomb interaction. This renders the CG less influential and the charge carriers behave like non-interacting particles. Under these conditions, ES VRH can only be reestablished by lowering the temperature [121–123]. Alternatively to an applied magnetic field, the crossover from ES to Mott VRH can be induced by either increasing the nanohole spacing (i.e. from 100 nm to 200 nm spacing) or by increasing the charge carrier density through an applied back gate voltage (see chapter 5).
At higher magnetic fields between $B = 4\ T$ and $B = 12\ T$, an increasing exponent which continuously rises from $\nu = 1/2$ to $\nu = 1$ is observed (figure 6.3(b)). This suggests a transition from 2D Mott VRH to activated charge carrier transport wherein hopping between localized states does no further play a role in the conduction process.

Crossover to Activated Transport

Intermediate values between $\nu = 1/2$ and $\nu = 1$ are obtained since activated transport dominates at high fields and high temperatures, while Mott VRH is more relevant for small B-fields and low temperatures. The conductivity is, however, fitted over the complete temperature range. Thus, the transport in magnetic field can be described by a high and a low temperature regime with activated transport or VRH as the dominant regime, respectively. In figure 6.3(c) the conductivity has been fitted separately for the high and the low temperature regime, which yields the expected exponents of 1/2 and 1 for low and high temperatures, respectively. At low B-fields, VRH is dominant even at high temperatures.

6.2 Magnetoresistance Behavior

In addition to the conductivity detected at constant magnetic field, additional measurements with variable magnetic field and fixed back gate voltage were performed to study the magnetoresistance. First, the magnetoresistance behavior at the CNP at sufficiently low B-fields to be still within the VRH regime will be addressed. As seen in chapter 5, weak localization behavior emerges at increased carrier concentrations, which is studied here under applied magnetic field. At higher B-fields, where the crossover from VRH to activated transport occurs commensurability effects can be observed, which is detailed in section 6.3. The magnetoresistance under high magnetic fields, where activated transport is present, will be discussed in chapter 7.
Figure 6.4(a) depicts the magnetoresistance behavior of different GAL devices as well as of a non-patterned graphene device in the low magnetic field region (between $B = 0\ T$ and

$B = 4\ T$). The observed magnetoresistance behavior furthermore depends on the carrier concentration (figure 6.4(b)). The observed negative magnetoresistance, on top of a weak positive magnetoresistance for large nanohole spacing or non-structured graphene, can be ascribed to interference effects either in the VRH or weak localization regime.

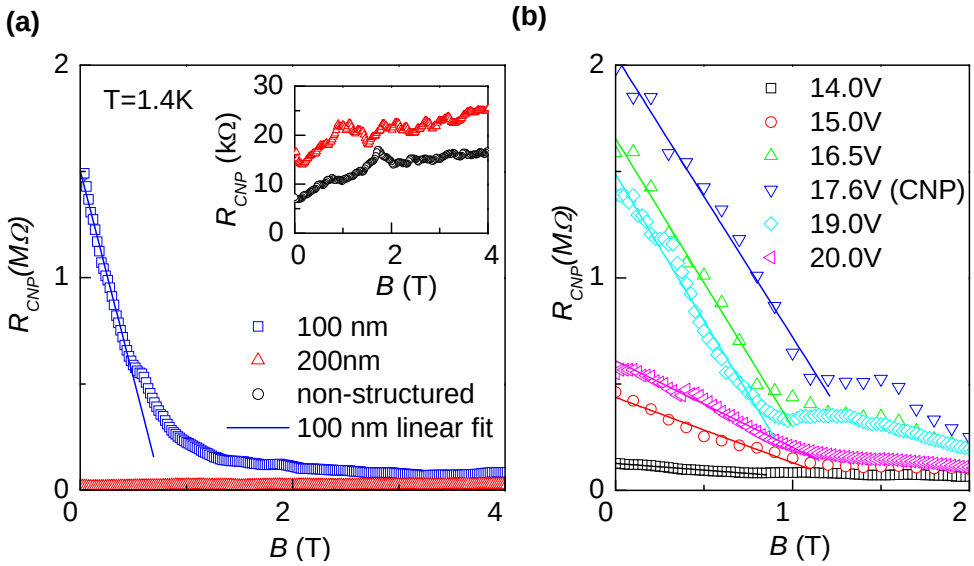

Figure 6.4: Magnetoresistance of GALs of different geometry. (a) Resistance at the CNP as a function of magnetic field for a bare graphene sample (8855_$D2a$, black squares), a 200 nm spacing GAL (8855_$D2b$, red triangles), and a 100 nm GAL (8855_$D4$, blue circles). All curves were measured at $T = 1.4\ K$. The dotted line represents a linear fit to the low field data of sample 8855_$D4$. The inset shows a zoom into the low resistance region of the main panel. (b) Magnetic field dependent resistance of the 100 nm sample 8817_$D4$ at different back gate voltages.

Positive Magnetoresistance (pMR)

Non-patterned graphene exhibits a weak positive magnetoresistance as shown in figure 6.4(a). The magnetoresistance up to $B = 4\ T$ is plotted for GALs with different nanohole spacings, as well as a non-patterned graphene device. The inset shows a zoom of the low resistance region. The observed behavior can be explained by the shrinkage of the electron wave functions with increasing magnetic field. When the magnetic length becomes comparable to the spatial extend of the electron-hole puddles in graphene, the resistance increases [130]. Samples with 200 nm spacing behave similarly in the low and intermediate magnetic field region. The same is true for smaller nanohole spacing under moderate magnetic fields. For these samples, however, another field dependent effect is dominant at small fields.

Negative Magnetoresistance (nMR) in the VRH Regime

At low magnetic fields ($B < 1\ T$), GAL devices with high nanohole density exhibit a pronounced quasi-linear negative magnetoresistance. This is exemplified by figure 6.4a) for the 100 nm spacing sample 8855_$D4$. The same effect is observed for other 100 nm and 80 nm spacing samples, and indicates a strong change in the hopping probability due to the applied magnetic field [133, 134].
The hopping probability itself corresponds to the sum over all possible interference paths of the charge carriers from one hopping site to another. The distance between the two hopping sites is the hopping distance R_{hop}. The numerical average of the conductivities along the different paths leads to a net linear decrease of the resistance with increasing magnetic field, provided that the B-field is above the threshold field B_c:

$$B_c = h/(2\pi e R_{hop}^{3/2} \xi^{1/2}). \tag{6.5}$$

Below B_c, the interference effects instead result in a MR depending on B^2 [141]. The threshold field can be calculated using the values from chapter 5. For the 100 nm spacing sample in figure 6.4(a) with $R_{hop} = 268\ nm$ and $\xi = 591\ nm$, one obtains $B_c = 6\ mT$. This calculated threshold field lies below the magnetic field resolution of the measurement. The same is true for the sample in panel (b). This is why only the linear part of the negative magnetoresistance is visible. Figure 6.4(b) shows the dependence of the slope of the linear negative magnetoresistance at different back gate voltages. Similarly to the localization strength, it is largest at zero charge carrier density at the CNP ($V_{CNP} = 18.0\ V$ for this sample) and for smallest nanohole spacing. For high charge carrier densities, a much weaker negative magnetoresistance is observed due to a transition to the weak localization regime, where the negative magnetoresistance can be described by a weak localization correction of the resistance (see below).
Since, similar to the AB effect, the linear negative magnetoresistance depends on interference of the charge carrier wavefunctions, the phase coherence length is an important parameter. In contrast to the AB effect, however, the negative magnetoresistance appears in the VRH regime. The latter is related to the flux penetrating the area A_{nMR} enclosed by the different hopping paths, which is of the order of $R_{hop}^{3/2}\xi^{1/2}$ [133]. In order for the interference effect to be visible, a charge carrier has to travel phase coherently around half of the circumference of the area A_{nMR}. This corresponds to a phase coherence length $L_\Phi \approx 580\ nm$ for the 100 nm spacing sample 8855_$D4$ and thus lies between three to four times the circumference of a nanohole with $d = 50\ nm$.

Weak Localization (WL)

As already mentioned, the observed linear negative magnetoresistance is distinguished from the negative magnetoresistance in the weak localization regime. For higher charge carrier concentrations, $|q| \geq 4 \cdot 10^{11}\ cm^{-1}$, the device can be brought into the latter regime where also a negative magnetoresistance is observed, albeit with considerably weaker slope. Figure 6.5 shows the conductivity correction as a function of magnetic

field $\Delta\sigma = \sigma(B) - \sigma(B = 0)$ for sample 8817_$D4$ (100 nm spacing) under such conditions ($q = -4.0 \cdot 10^{11}\ cm^{-2}$).

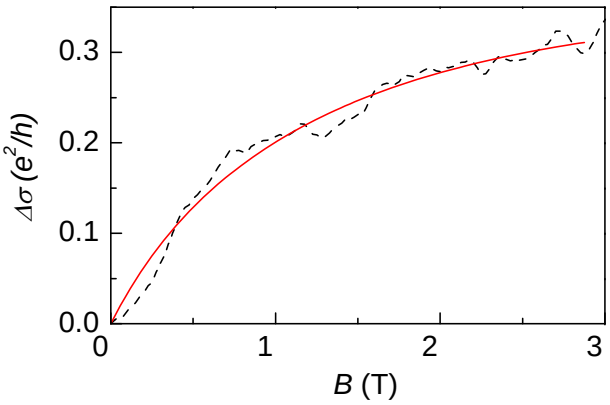

Figure 6.5: Weak localization correction in magnetic field for sample 8817_$D4$ (100 nm spacing) in the Weak Localization regime at a gate voltage of $V = 23.5\ V$ which corresponds to a charge carrier concentration of $q = -4.0 \cdot 10^{11}\ cm^{-2}$. The red line shows the fit of the weak localization correction (equation 6.6).

The nMR (positive magnetoconductance) can be accounted for by a weak localization correction to the conductivity, in analogy to highly doped GALs [25]:

$$\Delta\sigma = \frac{e^2}{2\pi^2\hbar}\left\{F\left(\frac{B}{B_\Phi}\right) - F\left(\frac{B}{B_\Phi + 2B_i}\right) - 2F\left(\frac{B}{B_\Phi + B_*}\right)\right\}, \tag{6.6}$$

where a finite phase coherence length L_Φ, intervalley scattering length L_i and scattering length (including intervalley, intravalley scattering and trigonal warping) L_*:

$$L_{\Phi,i,*} = \sqrt{D\tau_{\Phi,i,*}} \tag{6.7}$$

with a diffusion constant

$$D = 1/2\nu_F^2\left(\tau_i^{-1} + \tau_*^{-1}\right)^{-1} \tag{6.8}$$

and corresponding time scales

$$\tau_{\Phi,i,*}^{-1} = \frac{4B_{\Phi,i,*}eD}{\hbar} \tag{6.9}$$

lead to a critical magnetic field $B_{\Phi,i,*}$, which would disrupt the localization effects, given by

$$B_{\Phi,i,*} = \frac{\hbar}{4e(L_{\Phi,i,*})^2} \tag{6.10}$$

The weak localization correction can be calculated from the function:

$$F(x) = ln(x) + \Psi(1/2 + 1/x), \tag{6.11}$$

where $\Psi(z)$ is the digamma function. For large z the Taylor approximation $\Psi(z) \approx ln(z) - 1/z \approx ln(1/2 + 1/x) - \frac{1}{1/2+1/x}$ holds, leading to

$$F(x) = ln(1/2x + 1) - \frac{1}{1 + 2x^{-1}}. \tag{6.12}$$

The fit based upon this equation is shown in figure 6.5 (red line). It yields a phase coherence length in the weak localization regime of $L_\Phi = 20\ nm$, an intervalley scattering length of $L_i = 11\ nm$, and a scattering length of $L_* = 3\ nm$. The corresponding time constants are obtained as $\tau_\Phi = 1.6 \cdot 10^{-13}\ s$, $\tau_i = 4.4 \cdot 10^{-14}\ s$, $\tau_* = 5.2 \cdot 10^{-15}\ s$, while $B_{\Phi,i,*} = 0.4/1.4/18\ T$ and $D = 0.00233\ m^2/s$. These values are in reasonable agreement with weak localization measurements on highly doped GALs with similar dimensions [25]. However, they are smaller than the phase coherence length derived in the VRH regime (see above). One plausible explanation for this difference is the considerably higher density of induced charge carriers in the weak localization regime. These charges are expected to screen localized states and thus render long phase coherent hops between them unlikely. This scenario is in agreement with the fact that in the WL-regime no B-dependent (AB-type) oscillations, which also require long phase coherence lengths, are observed.

6.3 Aharonov-Bohm Effect

In section 6.1, it is shown that for sufficiently high magnetic fields, VRH is no longer the relevant transport mechanism in the GAL structures. This holds particularly at high temperatures. At sufficiently high magnetic fields, the device is in the Quantum Hall (QH) regime, where the conductivity is determined by edge channel conduction. In the magnetic field range between 2 and 10 Tesla the conductance is of the order of e^2/h, as the sample leaves the VRH regime, where a very low conductivity is observed at the CNP. For magnetic fields above $B = 10\ T$ the conduction is still governed by activated transport, but the resistance at the CNP increases again due to the gap opening in magnetic field (chapter 7).

In this mid-field range, where increased conductivity prevails, one observes commensurability effects in the GAL devices. This comprises resistance oscillations as a function of magnetic field (see figure 6.6(a)), which can be ascribed to Aharonov-Bohm (AB) type oscillations around the individual nanoholes [136, 142]. Figure 6.6(a) shows the conductivity (black dashed line) as well as its variation ($\sigma - \sigma_0$, red solid line) as a function of magnetic field. Here, σ_0 is the smooth background conductivity. Oscillations occur in the region where the conductivity deviates from zero, whereas they are absent in the low and high field region, where the conductivity approaches zero. In general, the oscillations are most prominent around the CNP. Moving away from the CNP, the oscillations are less periodic, as expected since for high carrier densities the conductivity is governed by weak localization (see section 6.2). The frequency of the oscillations along with higher harmonics are visible in the Fourier spectrum in figure 6.6(b). The AB type oscillations are related to the magnetic flux Φ penetrating the enclosed area A between the two paths that the charge

carriers can take around the individual nanoholes.

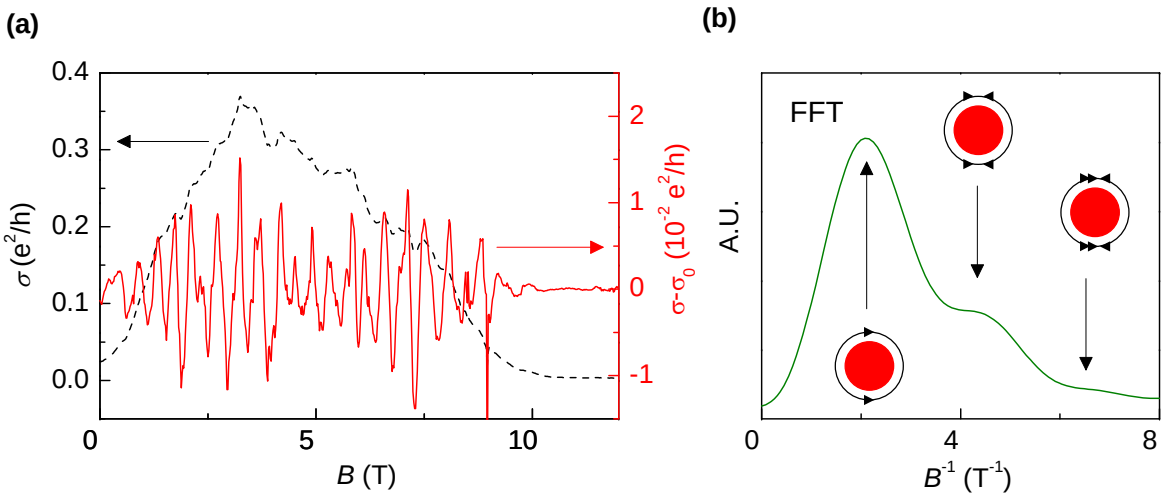

Figure 6.6: Aharonov-Bohm oscillations in GALs. (a) Aharonov-Bohm oscillations in sample 8855_$D4$ at $T = 1.4\ K$ close to the CNP, at $V_g = 14.1\ V$. The smoothly varying background σ_0 is subtracted from the conductivity σ to visualize the oscillations. (b) Corresponding FFT of the oscillations, clearly displaying maxima at $eA/h = 2.1$ and $2eA/h \approx 4.2$. Also a third, weak maximum at $3eA/h \approx 6.3$ can be discerned.

A charge carrier can either move along the upper or lower half of the nanohole. Interference of the wave functions of the carriers can either be constructive or destructive, depending on the nanohole size since the charge carrier accumulates a phase difference φ when moving along the different paths:

$$\Delta\varphi = \frac{2\pi e}{h}\Phi. \tag{6.13}$$

The magnetic flux is given as a path integral $\Phi = \oint \vec{A}(\vec{s}) \cdot d\vec{s}$, where $\vec{A}(\vec{s})$ is the vector potential $B = \nabla \times \vec{A}(\vec{s})$. Using Stokes law, Φ can be calculated as the integral over the enclosed area A: $\Phi = \int_A \vec{B} \cdot d\vec{A}$. With each flux quantum $\varphi_0 = h/e$ the phase difference between the two paths around the nanoholes varies between 0 and 2π. This leads to an AB oscillation period of

$$\Delta B = \varphi_0/A. \tag{6.14}$$

The area enclosed by the charge carriers moving around the nanohole can be calculated from the AB diameter d_{AB}: $A = \frac{1}{4}\pi d_{AB}^2$. Conversely, the AB oscillation period can be used to determine the diameter of the area enclosed by the charge carrier movement. For the 100 nm spacing sample an oscillation period of $\Delta B = 0.48\ T$ is obtained (see figure 6.6(b)). This corresponds to an AB diameter of $d_{AB} = 105\ nm$, in close correspondence to a closed path around a nanohole of 50 nm diameter with a center to center distance of 100 nm to the neighboring nanoholes.

Being caused by interference effects, AB oscillations, similar to the weak localization correction, can only be observed for sufficiently long phase coherence lengths. This is the case if the phase information is preserved in the transport path around the nanohole. If scattering occurs, phase information is lost and the AB oscillation amplitude is decreased and finally vanishes. Thus, the AB oscillations give a measure of the phase coherence length of the interfering charge carriers. The estimated phase coherence length is determined by the number of higher harmonics discernible in the Fourier spectrum of the oscillations. For sample 8855_$D4$ besides the first harmonic, the second and weak third harmonic are visible at $1/B \approx 4.2\ T^{-1}$ and $1/B \approx 6.3\ T^{-1}$ (figure 6.6(b)), respectively. Observation of the higher harmonics testifies a high phase coherence, enabling the charge carriers to move a second and third time phase coherently around half of the nanohole. Thus, the phase coherence length for sample 8855_$D4$ can be estimated to be three times half of the circumference of the closed path, which corresponds to a value of $L_\Phi \approx 495\ nm$. Similar phase coherence lengths are found for the other 100 nm spacing samples. Although the phase coherence length in the AB regime is determined in a different transport regime and a different magnetic field range than the VRH regime, the extracted phase coherence length of $L_\Phi \approx 500\ nm$ for the same sample, is in good agreement with the localization length derived from the negative magnetoresistance (see section 6.2). Furthermore, comparable values have been gained from AB oscillations in GALs prepared on SiC ($L_\Phi \approx 100\ nm$ at $T = 1\ K$) [136].

Chapter 7

Fundamental High Field Gap

Introduction

In chapter 5 it is shown that a transport gap can be opened by structuring graphene into GALs. The transport in such samples is governed by variable range hopping. In an applied magnetic field, a transition to activated behavior occurs for high enough fields (chapter 6). In the latter region, the QHE dominates the transport characteristics. For pristine graphene, the linear dispersion leads to the formation of Landau levels, whose energy exhibits a square-root dependence on the magnetic field [29, 30]. Compared to 2DEGs, the energy positions of the Landau levels are shifted, and a $N = 0$ LL emerges at zero energy. This lowest Landau level is equally shared between electrons and holes. Monolayer graphene displays the integer quantum Hall effect (iQHE) with filling factors $\nu = 2, 6, 10, ...$ due to the four-fold degeneracy originating from the spin and sublattice symmetry (see chapter 2). At high enough magnetic fields, or for enhanced sample quality (chapter 4), distinct levels of the degree of freedom of the charge carriers can be traced. Specifically, in the Landau level spectrum additional levels with filling factors corresponding to all possible integers appear. This lifting of the degeneracies has been ascribed to electron-electron interactions [143, 144] or spin splitting due to the Zeeman effect [96, 98, 145, 146]. Which of the involved mechanisms is responsible for the splitting and the sequence in which the respective filling factors appear, depends on the strength of the respective interaction. Recently, the question if the hierarchy of the symmetry breaking in pristine graphene favors either spin-first, valley-later splitting or vice-versa has gained attention [147].
For GALs, just as without magnetic field, theory also predicts the presence of a fundamental band gap under applied magnetic field [148, 149]. Recently, theoretical work on GALs has predicted that breaking of the electron-hole symmetry in the individual valleys K and K' occurs for an isolated graphene antidot in a magnetic field [150]. Thus, electrons would be associated with one valley and holes with the other valley. Experimentally, it was observed, that the QHE can be suppressed at low magnetic fields, where the cyclotron orbit of the charge carriers is larger than the antidot spacing [25].

Part of this chapter was published in: E. C. Peters et al., Valley-polarized massive charge carriers in gapped graphene. Phys. Rev. B, Phys. Rev. B **87**, 201403(R) (2013) .

Experiment

Here, we use the GAL structures to address the magnetic field behavior of the gap as well as its influence on the QHE states in graphene. For this purpose measurements are conducted in high magnetic fields up to 30 T. The longitudinal as well as the Hall resistance are used to evaluate the gap properties. All electrical measurements are performed by standard AC lock-in techniques at temperatures down to 1.4 K. Like in the measurements before, sufficiently low currents ($I < 10\ nA$) are used in order to avoid heating effects. Angle dependent measurements are conducted by rotating the sample within the external magnetic field, which allows to distinguish between different Landau level splitting mechanisms.
The influence on the band gap in high magnetic fields is investigated in section 7.1. Angle dependent measurements, where the sample is rotated in the external magnetic field provide more insight into the nature of the opened gap and the hierarchy of the Landau level splitting. The conclusions drawn are supported by Hall resistance measurements of the GALs for different doping levels, temperatures, and magnetic fields (section 7.2). The band gap size in dependence of magnetic field as well as the implications for the band structure at low energies are evaluated in section 7.3 by analyzing the Landau level splitting in the form of fan diagrams. Furthermore, the investigation of samples of highest quality allows to study additional Landau Level splitting effects.

Devices

As an extension of the GAL devices of the previous chapters, devices patterned into Hall bar structures are studied. Such devices enable separate measurements of the longitudinal and transverse conductivities (see chapter 3). The fabrication process is similar to the one for the lateral four-terminal device configuration, since the Hall bar is defined in the same lithography and etching step as the antidot lattice. A typical GAL device is shown in figure 7.1a). To ensure good contacts, the contact width is $\geq 1\ \mu m$.

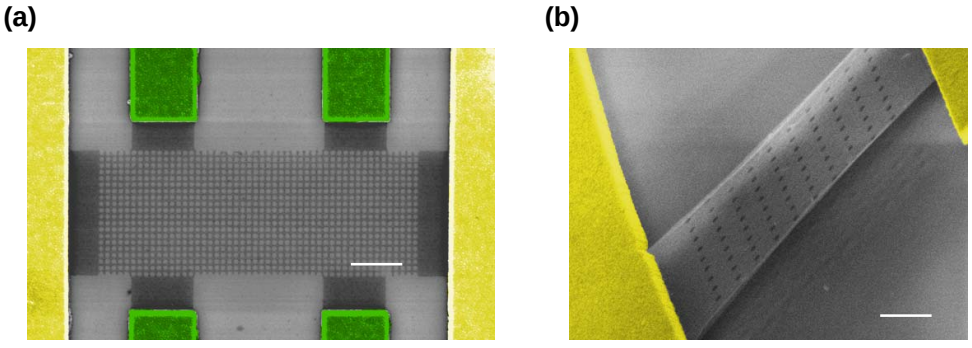

Figure 7.1: SEM images of a) a Hall bar GAL device (scale bar is 1 μm) and b) a suspended GAL (scale bar is 500 nm). The current contacts are colorized yellow and the Hall probes green.

For the investigation of high quality samples, GAL structures in lateral four-terminal geometry are rendered free-standing. After contacting, 150 nm of the underlying 300 nm thick SiO_2 layer are etched away by buffered hydrofluoric acid (HF), followed by critical point drying of the sample. During this step, the devices are supported by thick gold contacts (3/100 nm Cr/Au), which is especially important for monolayer and GAL devices since they are mechanically more fragile than bilayer graphene. Before current annealing, the CNP usually occurs out of the accessible gate voltage range, which is limited to around $\pm 10\ V$ for the suspended devices with a distance of 150 nm between flake and gate dielectric. During the current annealing process (see chapter 3), it typically shifts close to zero gate voltage ($V_{CNP} = 0\ V$). While for the non-suspended GALs on SiO_2 a maximum carrier mobility of 5.000 cm^2/Vs is found, the suspended devices reach values up to 20.000 cm^2/Vs.

7.1 Fundamental Band Gap

7.1.1 Magnetic Field Dependence

Gap opening by magnetic field

In chapter 5 it was shown that for sufficiently high magnetic fields, activated behavior dominates the charge transport. In fact, above $\approx 6\ T$ the minimum conductivity in most of the temperature range can be described by this conduction type.

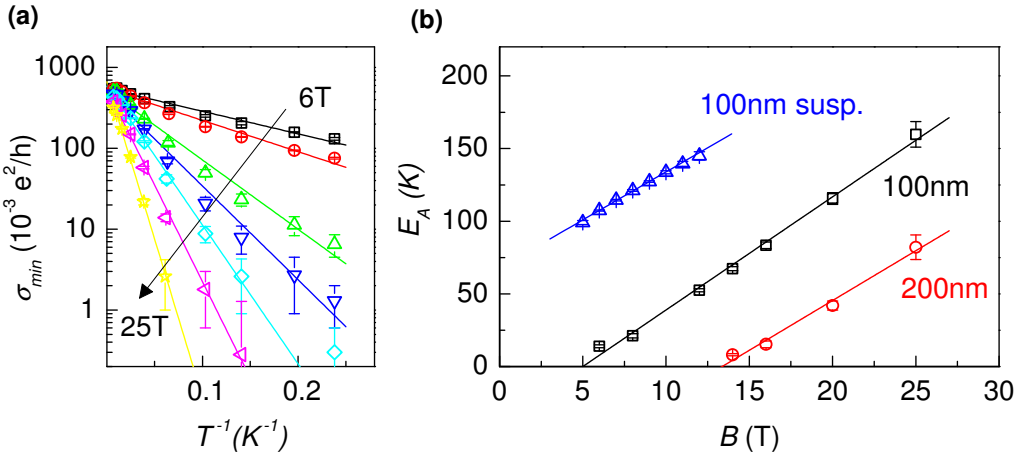

Figure 7.2: Magnetic field dependence of the activated gap. (a) Arrhenius plot of the conductivity at the CNP of the 100 nm spacing sample 9249_$D3a$ for magnetic fields between 6 T and 25 T. (b) Activation gaps E_A displayed as a function of magnetic field for the 100 nm (black squares) 9249_$D3a$, 200 nm (red circles) 9249_$D2$ and 100 nm suspended (blue triangles) spacing 9139_$D2a$ samples, with the full lines representing linear fits.

In figure 7.2(a) the temperature dependence of conductivity at the CNP is shown for a

100 nm spacing sample in the magnetic field range from 6 T to 25 T. Between $T = 3.1$ K and 98 K, the minimum conductivity varies by 5 orders of magnitude. The data can be reasonably fitted by a $ln(\sigma) \propto T^{-1}$ dependence. The extracted fit parameters provide access to the gap size (see chapter 5) as a function of the applied magnetic field. The result is shown in figure 7.2(b) for the same 100 nm spacing sample, as well as for a 200 nm spacing sample and a 100 nm spacing suspended sample. For all magnetic fields, the extracted gap is larger for the 100 nm than for 200 nm spacing. An even higher gap is detected after suspension and current annealing of the 100 nm spacing, as a consequence of reduced doping. The line fits to the temperature dependent activation gap of the respective device (figure 7.2(b)) signify that the gap size increases linearly with magnetic field. The gap determined in this manner is obscured by Landau level broadening Γ due to a finite Landau level width. Extended states forming the center of the Landau level contribute to conduction, while the localized states in the Landau level tails independent of their occupation do not contribute to the conduction (see chapter 2, figure 2.2). Increased scattering in low quality samples causes higher Landau level broadening. Thus, for the suspended sample the Landau level broadening is expected to be smaller than for the non-suspended sample. Due to the Landau level broadening, the obtained activation gap E_A is smaller than the Landau level splitting. For the 200 nm sample the activation gap can only be discerned for magnetic fields above ≈ 10 T. The gap opening is also visible in the magnetoresistance behavior of the GALs, as described below.

Diverging Magnetoresistance

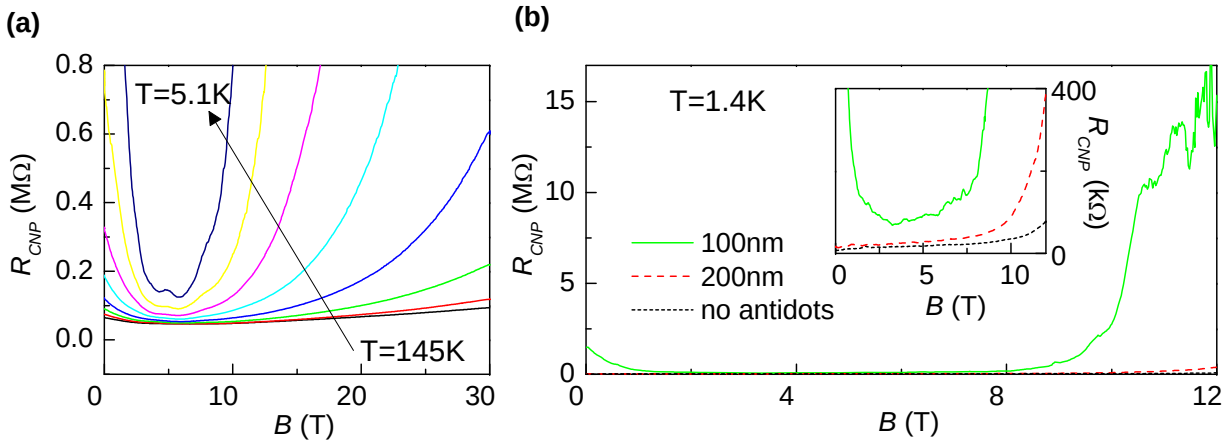

Figure 7.3: Magnetoresistance behavior as a function of temperature and for different devices. (a) Temperature dependent magnetic field sweeps of a 100 nm spacing sample (9249_$D3a$). (b) Magnetoresistance at $T = 1.4$ K for a 100 nm (8855_$D4$), 200 nm (8855_$D2b$) and a non-structured sample (8855_$D2a$).

Figure 7.3 depicts the temperature dependent magnetoresistance of a 100 nm spacing

sample, and the magnetoresistance of different GAL and pristine graphene devices. The magnetoresistance curves are taken at the CNP of the respective device. As already seen in chapter 6, pristine graphene and GALs of low spacing exhibit a monotonous positive magnetoresistance at low magnetic fields. If the nanoholes are more closely spaced, a negative magnetoresistance is observed. Similarly to decreasing the carrier concentration, lowering of the temperature results in a stronger negative slope of the magnetoresistance at low magnetic fields. This trend is expected since the device is brought into a temperature and doping range where strongly localized VRH prevails.
At high magnetic fields, in the quantum Hall regime ($B \approx 10\ T$), the GAL devices display a diverging positive magnetoresistance, whose magnitude considerably exceeds that of pristine graphene (see figure 7.3(b)). This effect is not only observed for the 100 nm spacing samples, but also for 200 nm nanohole spacing, albeit with a weaker resistance increase in the latter case. Similar behavior has been found in the high field region of pristine graphene of sufficient quality [96, 98], and has in this case been attributed to a lifting of the spin degeneracy. The diverging positive magnetoresistance displayed by the GALs indicates a degeneracy lifting of the zeroth LL [151] by the gap introduced by the antidot lattice.

Diverging Hall Resistance

In order to further analyze the gap opening and the diverging magnetoresistance, Hall resistance measurements are performed. The Si back gate is used to tune the charge carrier concentration. The gate coupling factor links gate voltage V_{back} with the charge carrier density according to: $q = \alpha V_b = \alpha(V_{back} - V_{CNP})$. Thus, the Hall and longitudinal resistances can be explored as a function of charge carrier density. In figure 7.4 the Hall resistance and longitudinal resistance at $B = 20\ T$ and $B = 30\ T$ of a 100 nm spacing GAL is depicted as a function of charge carrier density. From these two quantities the lateral σ_{xx} and the transverse σ_{xy} conductivities can be derived by a tensor inversion (see chapter 3) as a function of the filling factor $\nu = \frac{qh}{eB}$.
The resistance plateaus observed at $R_{xy} = 2\ h/e^2$, $6\ h/e^2$,... (dashed gray lines in figure 7.4(a)) corresponding to filling factors 2,6,... are characteristic of the LL pattern of pristine graphene. They are accompanied by minima in the longitudinal resistivity (figure 7.4(b)) since the Fermi level is located between two Landau levels, where only localized states and no extended states exist. By comparison, if the Fermi level is positioned at the center of a Landau level, extended states are available for conduction. This leads to finite longitudinal resistivity and the Hall resistance changes from one plateau to the next.
In pristine graphene, the Hall resistance changes its sign and smoothly crosses zero at zero charge carrier density since the Fermi level is positioned in the zeroth LL which is shared by electrons and holes. In the GALs, however, with increasing magnetic field, the Hall resistance deviates from this behavior. At small charge carrier densities, the Hall resistance starts to diverge and does not cross zero anymore above 10 T. Figure 7.4(a) reveals that ρ_{xy} diverges close to the CNP, located at $V_{CNP} = 16.0\ V$ for sample 9398_$D2$, to either negative or positive values on the p-type and n-type side, respectively. This

behavior evidences the opening of a fundamental band gap at elevated magnetic fields. With increasing B-field, the gap region widens and the onset where the resistance starts to diverge moves to higher absolute voltages $|V_{back} - V_{CNP}|$.

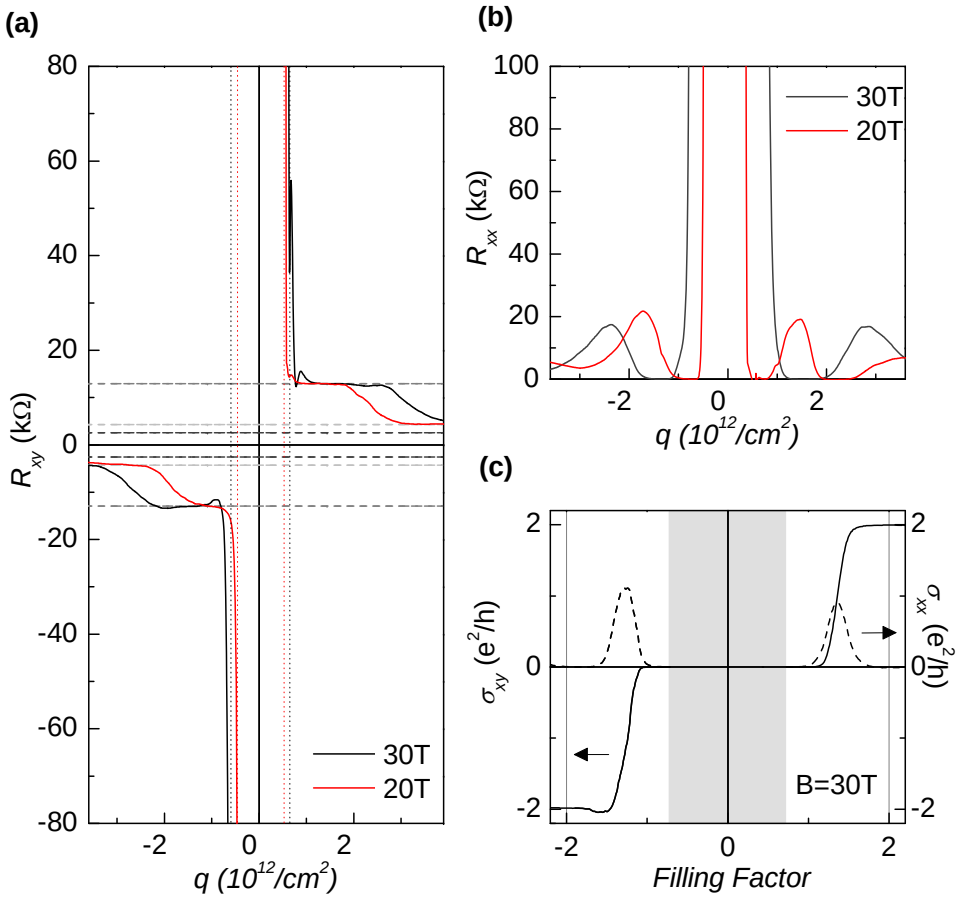

Figure 7.4: Hall resistance measurements at $T = 4\ K$. (a) Hall resistance of sample 9398_D2 at $B = 20\ T$ and $B = 30\ T$. The dashed gray lines indicate the position of the usual graphene resistance plateaus. (b) Corresponding longitudinal resistances. (c) Longitudinal σ_{xx} and transverse σ_{xy} conductivities calculated from the data in panels (a) and (b).

Figure 7.4(c) displays the longitudinal and transverse conductivities calculated from the data in panels (a) and (b). The zeroth LL, which is located at zero filling factor for pristine graphene, is split up in two separate levels below and above the gap. Within the gap both, longitudinal and transverse conductivity, vanish since no conduction is possible.

7.1.2 Angle Dependence

In order to explore the origin of the fundamental band gap opened at elevated magnetic fields in more detail, we perform angle dependent measurements of the minimum conduc-

tivity under magnetic fields between 0 and 30 Tesla. For these measurements, the sample is rotated out-of-plane by an angle θ relative to the surface normal. Figure 7.5 shows the dependence of the resistance at the CNP on perpendicular and in-plane external magnetic field. Measurements are performed at $T = 4\ K$ for a 100 nm spacing device and for angles $\theta = 0°$, 15°, 30°, 45°, 60° and 75°.

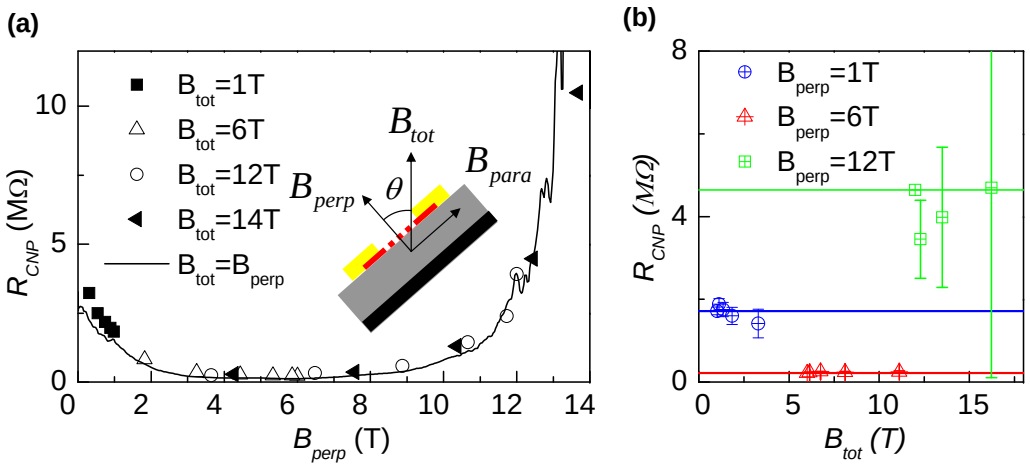

Figure 7.5: Tilted magnetic field measurements of sample 9249_$D3a$ at $T = 4\ K$. (a) Measurements under constant total magnetic field. (b) In these measurements, the perpendicular field is kept constant while the total field changes. The resistance remains at the zero-angle-value (solid lines) within the error bars.

The solid line in figure 7.5a) represents the resistance at the CNP as a function of perpendicular field $B_{perp} = B_{tot}cos(\theta)$ at $\theta = 0$ for a 100 nm spacing GAL device. As observed before (chapter 6), there emerges a negative magnetoresistance at small fields and a pronounced positive magnetoresistance at higher fields. As exemplified for constant total fields of $B_{tot} = 1$, 6, 12, and 14 T, the angle-dependent resistance at these fields coincides with the values recorded at zero angle, where $B_{tot}\ (\theta = 0°) = B_{perp}(\theta)$. Since the same resistance values are obtained for constant total field and variable perpendicular field magnetic field, it follows that the resistance at the CNP depends on the perpendicular magnetic field component B_{perp} only. Measurements at constant perpendicular magnetic field confirm this conclusion, i.e. the resistance remains almost constant for different values of B_{tot}. The sizable error bars arise due to an uncertainty of the sample rotation angle of 3° which leads to an error in the calculated B_{perp} component. That the resistance at the CNP (i.e., the minimum conductivity) depends only on perpendicular magnetic field hints against a spin-related origin of the opened band gap. If the band gap were related to spin degeneracy lifting due to the Zeeman effect, a dependence of the minimum conductivity on the total B-field would be expected. This has indeed been observed for the zeroth LL splitting for pristine graphene under high magnetic fields [96, 98].

7.2 Valley Splitting of the Zeroth Landau Level

7.2.1 Split Electron- and Hole-Conduction

The Hall resistance does not only demonstrate the opening of a fundamental band gap, but can also be used to determine the electron and hole concentrations.

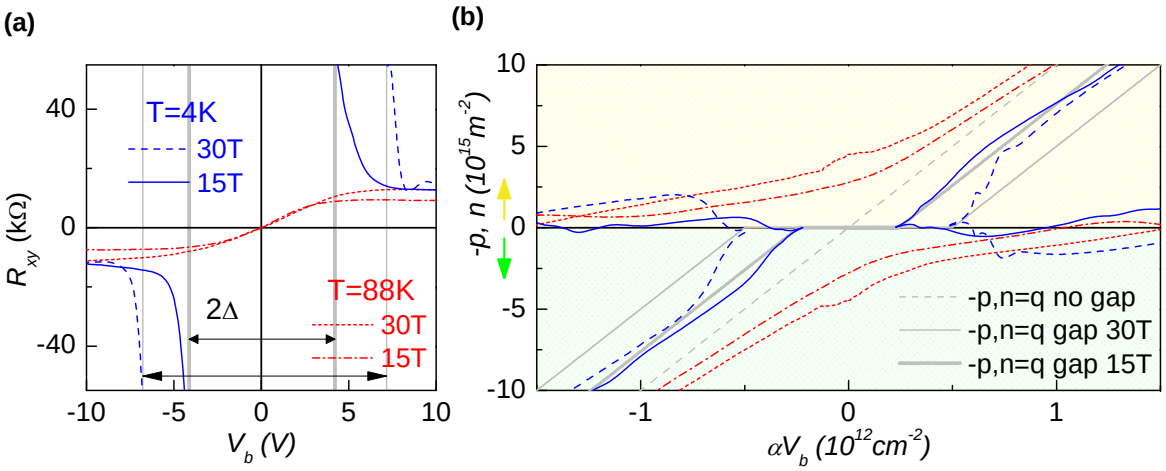

Figure 7.6: Insulating gap around the CNP in a 100 nm (9398_$D2$) spacing GAL device under high magnetic fields. (a) Hall resistance measured at $T = 4\ K$ and $T = 88\ K$, respectively, each at magnetic fields of $B = 15\ T$ and $B = 30\ T$. (b) Concentration of electrons (positive values) and holes (negative values), as determined from the plots in the first panels. The three gray curves (solid bold, solid fine, and dashed) represent ideal cases of pure electron or hole conduction outside the gap for the two different gap sizes.

Zeroth Landau Level

Figure 7.6(a) depicts a similar plot of the Hall resistance like in the previous section, however, with the focus on the zeroth Landau level. The Hall resistance is shown for $T = 88\ K$ (dash-dotted red line $B = 15\ T$; dashed red line $B = 30\ T$) and $T = 4\ K$ (solid blue line $B = 15\ T$; dashed blue line $B = 30\ T$). The high temperature Hall resistance differs notably from the low temperature data due to the presence of the band gap. For temperature above 30 K, there is a smooth transition of R_{xy} between the $\nu = 2$ and $\nu = -2$ plateaus at zero effective charge carrier density ($q = \alpha V = 0$), even at the highest B-field (see data at 88 K). In this respect, GALs behave similarly to pristine graphene, which also shows a smooth zero transition of the Hall resistance. This finding testifies a finite, equal density of electrons and holes that is maintained near the CNP [152].
Upon cooling to $T = 4\ K$, however, the GAL samples are distinguished from pristine graphene by the fact that R_{xy} starts to diverge at small net charge carrier densities q. In fact, it does not cross zero anymore for magnetic fields above 10 T and a temperature of $T =$

4 K. Outside the gap region 2Δ, which is insulating, the high-field Hall resistance exhibits quantized resistance plateaus at the usual graphene filling factors as already described in section 7.1. Since below 30 K the band gap is comparable or larger than the thermal energy, the Hall resistance follows a $(1/q)$-dependence away from the quantized $\nu = \pm 2$ plateaus and diverges toward the asymptote of $\alpha V_b = \pm \Delta q$ (indicated by gray lines in figure 7.6a)). With increasing magnetic field the asymptote is shifted to higher absolute voltages $|V_b| = |V_{back} - V_{CNP}|$. Likewise, the longitudinal (σ_{xx}) and transverse (σ_{xy}) conductivity are influenced by the band gap. Both flatten into a plateau of zero conductivity in the gap region between filling factors $\nu = -2$ and $\nu = +2$ (see figure 7.6(b)). In the insulating region, the detected current lies below the digitalization limit.

Valley Splitting

The Hall resistance data provides direct access to the electron and hole density. In an applied magnetic field, the inverse Hall coefficient is given as $1/R_H = B/R_{xy}$. For a semiconductor with two carrier types, the densities are related to the Hall coefficient by [153]:

$$\frac{1}{R_H} = \frac{e(n\mu_n + p\mu_p)^2}{n\mu_n^2 - p\mu_p^2}, \tag{7.1}$$

where n and p are the electron and hole density, and μ_n and μ_p the corresponding mobilities. In the present samples, the conductance is symmetric in charge carrier density around the CNP, and hence the condition of equal mobility is fulfilled ($\mu_p = \mu_n$). Thus equation 7.1 can be simplified to [154]:

$$\frac{1}{R_H} = \frac{B}{R_{xy}} = \frac{e(n+p)^2}{n-p}. \tag{7.2}$$

For calculating the electron and hole charge carrier densities, the total charge carrier density q is used. In case of pristine graphene without a band gap or GALs in the high temperature region, the net charge carrier density is defined as $q = n - p$. It can be determined from $q = \alpha V_b$, where α is the gate coupling constant. For the shown 100 nm spacing sample, the latter assumes a value of $\alpha = 8.5 \cdot 10^{10}\ cm^{-2}V^{-1}$. Thus, the resulting electron density is:

$$n = \frac{1}{2}((n+p) + q) \tag{7.3}$$

and (negative) hole density is:

$$-p = -\frac{1}{2}((n+p) - q). \tag{7.4}$$

Using equation 7.2 these two quantities are plotted in figure 7.6(b) around the CNP as a function of q.
At high temperatures ($T = 88\ K$), electrons are the majority charge carriers in the n-type regime (positive q, $q \geq 5 \cdot 10^{15}\ m^2$), where the electron density approaches $n = q$, while the hole density approaches $p = 0$. The inverse is true for the p-type regime (negative q),

where holes are the majority charge carriers. Close to the CNP both charge carrier types coexist with a charge carrier density of $n = p = 2.8 \cdot 10^{15}\ m^{-2}$ at $T = 88\ K$ and $B = 15\ T$. At higher magnetic fields, the electron and hole density increases to $n = p = 4.5 \cdot 10^{15}\ m^{-2}$ at $B = 30\ T$. This observation is similar to pristine graphene, where the individual carrier density increase at the CNP with increasing B-field has been explained by the proportional dependence of the degeneracy of the $N = 0$ LL on the magnetic field [152].
By contrast, at low temperatures ($T = 4\ K$), the gap emerges in the charge carrier density and the Hall resistance starts to diverge around the CNP. The zero crossing of the Hall resistance at the CNP vanishes for magnetic fields $B \geq 15\ T$, which indicates that there is no longer a coexisting density of electrons and holes at the CNP (see equation 7.2). If the magnetic field is increased further, R_{xy} already starts to diverge further away from the CNP after assuming the characteristic value for the $\nu = \pm 2$ plateaus $R_{xy} = \pm 12.9\ k\Omega$. This behavior evidences a stronger $N = 0$ Landau level splitting $2\Delta q$ in the charge carrier density at higher magnetic fields. If R_{xy} is plotted versus charge carrier density, this trend can be observed by a shift of the asymptote from $\alpha V_b = \pm \Delta q = 2.2 \cdot 10^{15}\ m^{-2}$ at $B = 15\ T$ to $\pm 4.6 \cdot 10^{15}\ m^{-2}$ at $B = 30\ T$. Below the corresponding values the gap is present and neither charge carriers exist. The charge carrier plot, thus, comprises three separate regions, specifically one below the gap, one above the gap and the third one the gap region itself.
Inside the gap region

(I) $-\Delta q \leq \alpha V_b \leq \Delta q$,

the equality $n = p = q = 0$ holds since no charge carriers are present, while in the region below the gap

(II) $\alpha V_b \leq -\Delta q$

the total charge carrier density is $q = \alpha V_b + \Delta q$. By comparison, above the gap

(III) $\alpha V_b \geq +\Delta q$

and the total charge carrier density is $q = \alpha V_b - \Delta q$.
The individual charge carrier densities (positive values for electron densities (yellow area) and negative values for hole densities (green area)) at low temperatures, as derived from equations 7.2, 7.3 and 7.4 for each of those regions, are plotted in figure 7.6(b).
It is apparent that above the gap, the conduction is n-type with a hole concentration close to zero ($p = 0$ and $n = q$). In contrast, below the gap there is p-type conduction with $-p = q$ and an electron density of approximately zero $n = 0$. The gray lines in figure 7.6(b) indicate the ideal cases of no band gap (dashed gray line), with purely hole and electron conduction below or above zero charge carrier density, respectively. In this case, the Hall resistance would also diverge but with an asymptote of $\alpha V_b = 0$. The solid gray lines are the ideal cases with non-zero asymptotes (non-zero band gap) for the respective magnetic fields of $B = 30\ T$ and $B = 15\ T$.

Taken together, the above findings demonstrate that the fundamental band gap opened under high magnetic fields separates electrons and holes. Since these two carrier types posses different chirality in the zeroth Landau level, this corresponds to an effective separation of carriers with opposite chirality above and below the gap. This valley polarization goes along with a preservation of the spin degree of freedom. The angle-dependent measurements of section 7.1 support this conclusion, since the gap (located around the CNP with R_{CNP}) shows a dependence only on the perpendicular B-field component, rather than the total B-field.
The splitting hierarchy differs from pristine graphene, where valley splitting is observed on top of spin splitting only for high quality devices and high magnetic fields [95]. The various splitting scenarios are contrasted in the following section, and a schematic of the Landau level structure and the consequences for the dispersion at low energies are presented in section 7.3.

7.2.2 Splitting Scenarios

Depending on the hierarchy of the degeneracy lifting, different scenarios for the Hall resistance are possible.
From the total density of states $D(E)$ at a given energy E the longitudinal conductivity σ_{xx} can be derived by application of the Kubo-Greenwood formalism [155, 156]:

$$\sigma_{xx} = e \int_{-\infty}^{\infty} \mu(E) D(E) \frac{\partial f(E)}{\partial E} dE. \tag{7.5}$$

In this equation $\mu(E)$ is the carrier mobility, which is assumed to be constant for all energies, and $f(E)$ the Fermi distribution function $f(E) = (e^{(E-E_F)/k_BT} + 1)^{-1}$. The Hall conductivity is obtained through the summation of all states up to the Fermi energy [157]:

$$\sigma_{xy} = \int_{-\infty}^{E_F} D(E) f(E) \left[1 - f(E)\right] / (k_B T) dE. \tag{7.6}$$

In combination with equation 7.2 and the concentration of electrons n and holes p

$$n, p = \int D_{n,p}(E) f_{n,p}(E) dE, \tag{7.7}$$

the Hall resistivity can then be calculated numerically. The above procedure is applied to the different DOS scenarios in figure 7.7, as discussed below.

No Degeneracy Lifting of the zeroth LL

Figure 7.7(a) shows the density of states and the resulting Hall resistance for monolayer graphene with neither valley nor spin degeneracy lifting. The density of states is marked in red for electrons and blue for holes. At the center of the Landau levels charge carriers can occupy extended states (shaded regions), while in the Landau level tails (filled regions)

localized states are present. Due to the separation of $N = 0$ and $N = 1$ LLs a resistivity plateau occurs at $\nu = \pm 2$. The depicted situation holds for pristine graphene at low magnetic fields and low sample quality. The corresponding Hall resistivity assumes quantized values for the plateau regions which occur when the Fermi level is positioned in between the LLs. Since in these regions, localized states are filled or depleted the conductivity remains constant. Only if the Fermi level E_F is moved into a LL center, where extended states can be occupied, the Hall resistivity changes.

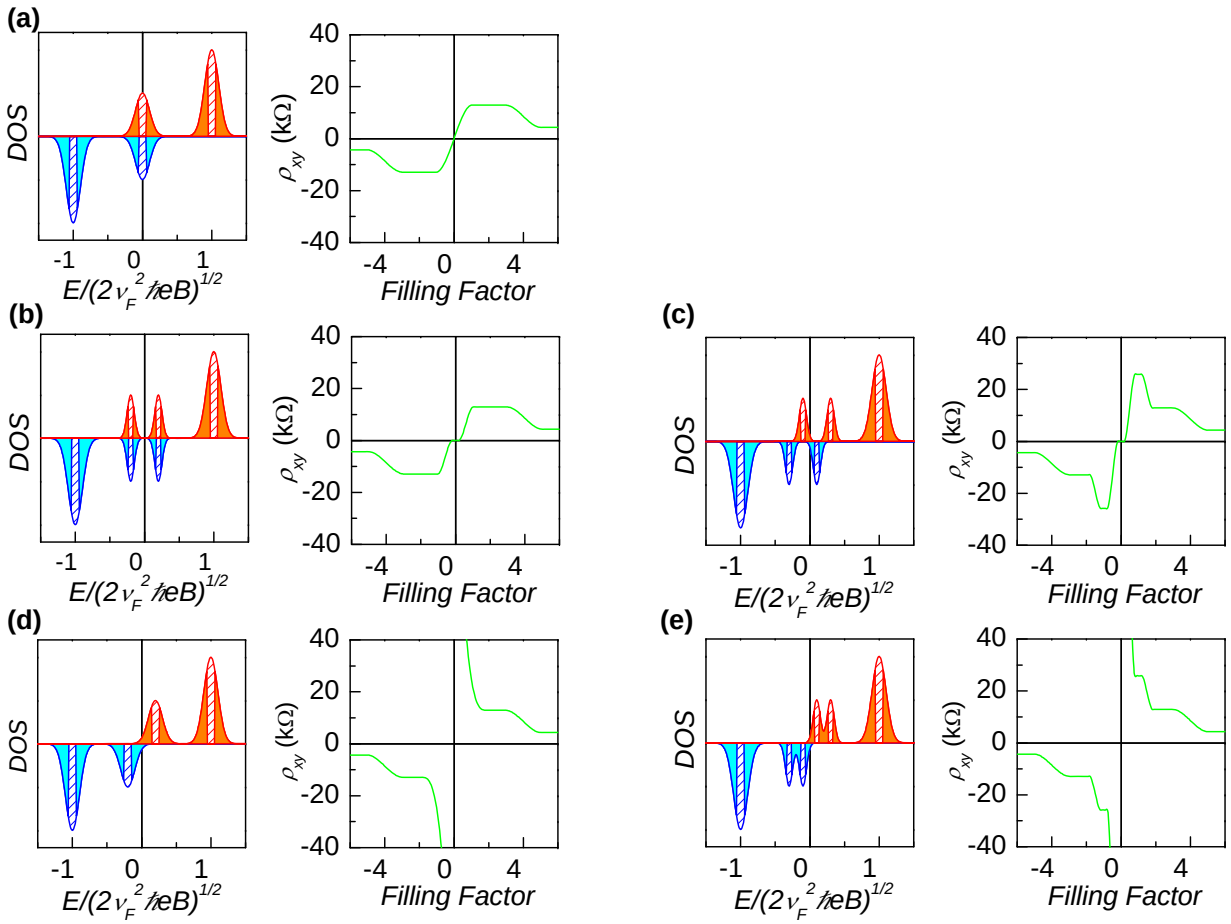

Figure 7.7: Schematic illustration of the density of states (positive for electrons and negative for holes) and Hall resistivity for different splitting scenarios in graphene. Partially adapted from [152] (a) No degeneracy lifting of the zeroth LL. (b) Pure spin splitting. (c) Spin splitting with additional, weaker valley splitting. (d) Pure valley splitting. (e) Valley splitting with additional, weaker spin splitting.

The finite density of electrons n and holes p above and below the CNP (but zero net charge) leads to a smooth zero crossing of the Hall resistance R_{xy}, which can be calculated numerically using equation 7.7 and 7.2. From equation 7.2 it is apparent that R_{xy} crosses zero for finite net charge carrier density $n + p$ and zero total charge carrier density $n - p$. This has

striking consequences for the zeroth LL in graphene, in particular even a band gap opening or a spin-first, valley-latter splitting cannot eliminate the zero crossing of R_{xy} [152].

Spin-first, valley-later splitting

Figure 7.7(b) and (c) depict spin-first, valley-later splitting , which has been observed for pristine graphene of high quality and in high magnetic fields [98], where the filling factor $\nu = 0$ appears due to the spin degeneracy lifting. This manifests itself in a zero-resistivity plateau, as shown in figure 7.7(b). In even higher quality graphene, additionally the degeneracy of the valley degree of freedom is lifted [96] and plateaus with filling factors $\nu = 1$ and $\nu = -1$ emerge in the Hall resistivity (figure 7.7(c)). Thus, in this scenario describing pristine graphene, the $\nu = 0$ Landau level behaves as a quantum Hall metal.

Valley-first, spin-later splitting

Figure 7.7(d) and (e) depict valley-first, spin-later splitting scenarios. Here, electrons and holes are separated above and below the CNP, respectively. Only in this valley-first scenario, the Hall resistivity diverges at the CNP. If only the valley degeneracy is lifted the Hall resistivity starts to rise from the $\nu = \pm 2$ plateaus, whereas for the full degeneracy lifting additional plateaus $\nu = \pm 1$ appear before the divergence towards the CNP. In this case, the $\nu = 0$ Landau level behaves like a Quantum Hall insulator. Such behavior has not yet been experimentally observed for the $\nu = 0$ LL, and identifies the valley-first scenario to be relevant for the present GALs. A similar splitting sequence has so far only been observed for higher LL in extremely high quality graphene on hBN [79].

Overview

type of sample / splitting	σ_{xx}	σ_{xy}	ρ_{xx}	ρ_{xy}
graphene, GALs [25, 29][this work]/ QHE for $\nu > 0$	0	f, q	0	f, q
graphene, GALs at high T [25, 29][this work]/ $\nu = 0$ LL, no degeneracy lifting	f	0	f	0
high quality graphene [96, 98, 145, 151]/ $\nu = 0$ LL, spin-first, valley-later	0	$0, q$	∞	$0, q$
GALs at low T [this work]/ $\nu = 0$ LL, valley-first, spin-later	0	0	∞	∞

Table 7.1: Different types of graphene samples with their longitudinal and transverse conductivities (σ_{xx} and σ_{xy}) and corresponding resistivities (ρ_{xx} and ρ_{xy}). f denotes finite and q quantized values, respectively.

Table 7.1 gives an overview of the different possible splitting scenarios for the zeroth LL. Outside the zeroth LL region, graphene as well as GALs follow the normal QHE behavior

with zero longitudinal resistivity and conductivity, but finite quantized values of the Hall resistivity and conductivity when moving from one LL to the next. The $\nu = 0$ LL of graphene is special, since it is shared between electrons and holes and thus at the CNP the the longitudinal conductivity and resistivity are finite, while the Hall conductivity and resistivity are zero. If spin-first splitting occurs, the scenario of a QH metal applies with a Hall resistivity and conductivity of zero. The longitudinal conductivity has been observed to approach zero and the corresponding resistivity to diverge. However, only for valley-first splitting, a QH insulator behavior at the $\nu > 0$ LL with an infinite resistivity at the CNP is present.

7.3 Dispersion Relation

As shown in section 7.1, the activation gap depends linearly on magnetic field and at $B = 25\ T$ reaches values of (160 ± 9) K for the 100 nm nanohole spacing GAL, 234 K for the freely-suspended 100 nm spacing sample, and (82±8) K for the 200 nm spacing sample. These gap sizes are, however, much smaller than theoretically expected for GALs [114]. Furthermore, they don't follow a square-root dependence [158] as expected for a linear dispersion. This is the case because the linear dispersion relation at low energies does not hold for the GALs. In the following it is argued that the linear dispersion does not apply to the GALs, and that instead a parabolic dispersion relation exists close to the CNP. The parabolic dispersion adds a mass term to the charge carriers and thus renders the magnetic field dependence of the splitting linear. Such band structure modification due to the GAL is not unexpected since also for GNRs, the confinement has been found to cause deviation from the linear dispersion of graphene [24].

7.3.1 Linear Dispersion

LL splitting in general is best observed in LL fan diagrams, where the LL position is traced in dependence of the magnetic field and the applied gate voltage. For pristine graphene with its linear dispersion relation, the LL positions as a function of gate voltage depend linearly on the applied magnetic field. This is also true for the $N = 0$ LL if the degeneracy is lifted. If the degeneracy is not lifted due to e.g. low sample quality, however, the zeroth LL remains at the CNP is independent of the applied magnetic field. This behavior can be deduced by converting the LL position in energy, given as: $E_{LL} = \sqrt{2e\hbar\nu_F^2 B\,|N|}$ (see chapter 2), to the dependence in the gate voltage positions. The Fermi level in graphene is given as: $E_F = \sqrt{q\pi\hbar^2\nu_F^2}$, which yields $V = q/\alpha = E^2/(\pi\hbar^2\nu_F^2\alpha)$ and further:

$$V_\pm = \pm\frac{2eB\,|N|}{\pi\hbar\alpha}. \tag{7.8}$$

Therefore, for a linear dispersion, the LL positions in energy show a square-root dependence on magnetic field, while as a function of gate voltage position the dependence is linear. On

this basis, also the energy gap, in analogy to the LL energy positions, exhibits a square-root dependence on magnetic field [158]. Since the dependence is not very strong, a splitting of the LL positions as observed in the GAL samples (see Hall resistance measurements in this section and the fan diagrams below) would result in huge hypothetical values of e.g. 1800 K at 20 T for the 100 nm spacing sample 9249_D3a. Furthermore, very large zero-field gap values would be obtained, which stronly exceed the measured activation gaps as well as the gaps extracted from the I/V measurements (see chapter 5). In the following it will be shown that although for a parabolic dispersion the magnetic field dependence of the LL energy positions is different, the dependence of the LL gate voltage positions is actually the same and the measured gap values can be accurately described by the parabolic instead of the linear dispersion in the GALs for the lowest LL.

7.3.2 Parabolic Dispersion

Since the linear dispersion relation is unable to account for the observed band gap, the GALs must have an influence not only on the band structure but also on the dispersion relation. Actually, band structure calculations indicate that the gap opening in GALs is accompanied by the emergence of a parabolic energy dispersion in vicinity of the gap [114, 116, 159].

Landau Level Positions and Splitting

In contrast to the linear dispersion relation, the energy positions of the LLs for a parabolic dispersion depend linearly on the magnetic field. This can be seen by application of the Schrödinger equation to the general parabolic dispersion in two dimensions:

$$E(k) = \frac{\hbar^2 k^2}{2m} = \frac{\hbar^2 q \pi}{m}, \tag{7.9}$$

where m is the mass and $q = k^2/2\pi$ is the charge carrier density. The resulting Landau level energies are equidistantly separated and given as:

$$E_{LL} = (N + 1/2)\hbar\omega_c. \tag{7.10}$$

Here, $\omega_c = eB/m$ is the cyclotron frequency, and N the Landau level index. The finite gap at zero magnetic field in the GALs can be included by an additional zero-field gap term E_G^0, which yields:

$$E_{LL} = (N + 1/2)\hbar eB/m + \frac{E_G^0}{2}. \tag{7.11}$$

The conversion to the LL positions as a function of back gate voltage via $V = q/\alpha$ and equation 7.9, results in $V = Em/\pi\hbar^2\alpha$. The ambipolar character of graphene (and GALs) can be accounted for by a plus and minus sign for electrons and holes, respectively, leading to:

$$V = \pm\left((|N| + 1/2)\frac{eB}{\alpha\pi\hbar} + \frac{m}{\alpha\pi\hbar^2}\frac{E_G^0}{2}\right), \tag{7.12}$$

where $V = V_b = V_{back} - V_{CNP}$ and $m = m_{eff} m_e$, with m_e as the free electron mass. For the zeroth LL, which is split by the gap, $N = 0$. Thus, for the two levels, which originate from the split zeroth LL, the positions in back gate voltage are given by:

$$V_{\pm} = \pm \frac{1}{2} \left(\frac{eB}{\alpha \pi \hbar} + \frac{m_{eff} m_e}{\alpha \pi \hbar^2} E_G^0 \right). \tag{7.13}$$

Thus, the LL positions both in energy and as a function of gate voltage depend linearly on magnetic field. This is distinguished from the case of the linear dispersion, where the gate voltage positions exhibit such linear dependence, but the positions in energy a square-root dependence.

Parabolic Dispersion of the zeroth LL

To test the above derived equations, the measured R_{xy} is evaluated as a function of magnetic field and applied back gate voltage. To make the LL positions better visible, the first derivative of the inverse Hall resistance $d(1/R_{xy})/dV_b$ is plotted in the fan diagrams, as exemplified in figure 7.8 for the 100 nm spacing sample 9398_$D2$. Next to the fan diagram line-cuts for the inverse Hall resistance as well as its derivative are shown for $B = 30\ T$. In the displayed gate voltage region, the plateaus at $\nu = \pm 2$ are well-developed and an additional plateau at zero conductivity is visible due to the gap opening. The maxima of $d(1/R_{xy})/dV_b$ within the green regions, where R_{xy} changes from one plateau to the next, correspond to the LL centers and thus enable to trace the LL positions with magnetic field. For low magnetic field, the QHE is obscured, most likely because the cyclotron diameter of the charge carriers approaches the GAL neck width, such that the edge channels impair each other [25].
The LL positions can now be compared to the values calculated based upon either a linear or parabolic dispersion (equation 7.8 and 7.12, respectively). The positions of the higher LLs are consistent with the assumption of usual linear graphene dispersion. The red dashed lines represent the values calculated for the LLs $N = 0, 1$, and 2 using the linear dispersion. The gate coupling factor can be extracted from the slope of the higher LLs, yielding $\alpha = 8.5 \cdot 10^{10}\ cm^{-2}V^{-1}$, which is, as observed in chapter 5, slightly larger than for pristine graphene on 300 nm SiO_2 [29]. This difference most likely results from inhomogeneous electric field effects, analogous to observations made on graphene nanoribbons [160]. This effect is especially relevant for the GALs with high antidot density.
For the zeroth LL, by contrast, the parabolic dispersion is necessary to describe the zeroth LL splitting. Even without the introduction of a zero-field gap, the dependence already matches the measured positions quite well. Using equation 7.13 to fit the zeroth LL splitting (black lines in figure 7.8), perfectly accounts for the observed splitting. As fit parameters an effective mass $m_{eff} = 0.08$ and a zero-field gap $E_G^0 = 44.0\ K$ are obtained. The latter value is in good agreement with the values of $E_G^0 \approx 30\ K$ derived from the I/V measurements in chapter 5. In the same manner as described above, values of $E_G^0 = 29.0\ K$, $\alpha = 7.2 \cdot 10^{10}\ cm^{-2}V^{-1}$ and $m_{eff} = 0.10$ were obtained for the 200 nm spacing sample 9249_$D2$, as well as $E_G^0 = 66.0\ K$, $\alpha = 5.0 \cdot 10^{10}\ cm^{-2}V^{-1}$ and $m_{eff} = 0.08$ for the

suspended 100 nm spacing sample 9139_$D2a$.

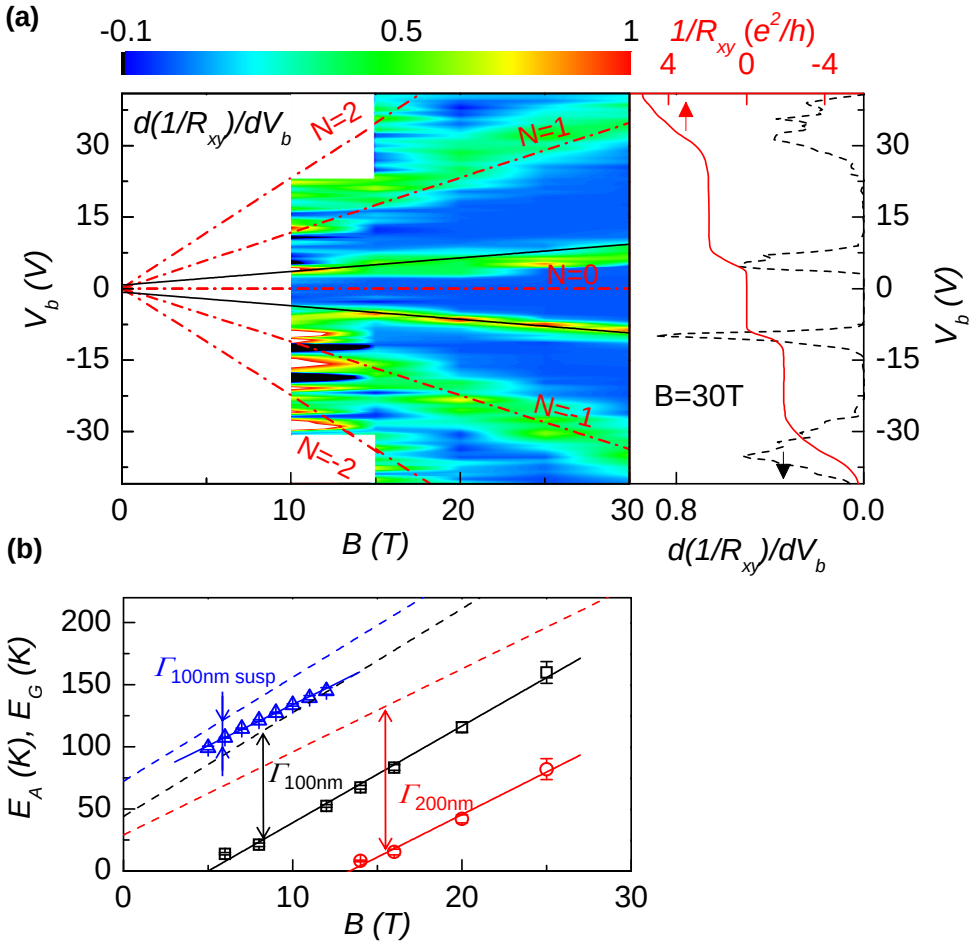

Figure 7.8: Fan diagram of sample 9398_$D2$ and extracted gaps. (a) First derivative of the inverse Hall resistance $d(1/R_{xy})/dV_b$ as a function of magnetic field and gate voltage at $T = 4\ K$. Line-cuts of $1/R_{xy}$ and its derivative at $B = 30\ T$ are displayed on the right. (b) Activation gap E_A and band gap E_G extracted from the LL fans differ by the respective Landau level broadening Γ for samples 9249_$D3a$ (100 nm), 9249_$D2$ (200 nm) and 9139_$D2a$ (100 nm suspended).

Combining the extracted values for the fit parameters m_{eff} and E_G^0 with equation 7.13 allows to determine the band gap in dependence of the magnetic field. Figure 7.8(b) compares the activation gap derived from the Arrhenius fits to the temperature dependence of the minimum conductivity (symbols) with the gaps E_G extracted from the LL fans (dashed lines) for samples of different spacing and quality. The difference between the two values is the Landau level broadening, since the activation gap is the distance between the mobility edges of the two broadened LLs. The values for E_G of a device are shifted with respect to the activation gaps E_A by the LL broadening of the sample. From figure 7.8(b) it is visible that this broadening depends on the sample quality. While the LL broadening obscures

the gap determined by the activation measurements, it has no influence on the gap derived from the LL splitting of the fan diagrams, since here only the LL centers and not their width are important for the fits. Furthermore, both E_A and E_G linearly increase with magnetic field due to the parabolic dispersion near the CNP.
Previous studies have found that the LL broadening depends on the amount of disorder of the sample [161, 162]. It hence can be expected that for high quality samples such as suspended devices the broadening is reduced, which is indeed observed for the present GAL samples. In particular, the broadening extracted from figure 7.8b) is estimated to be $\Gamma = (90 \pm 10)\ K$, $\Gamma = (120 \pm 10)\ K$ and $\Gamma = (30 \pm 10)\ K$ for the 100 nm, 200 nm and suspended 100 nm spacing sample, respectively. The latter value is considerably smaller than the broadening in the non-suspended GALs and also smaller than 100 K, which has been reported for Si/SiO_2-supported pristine graphene at low temperatures [163], reflecting the improved quality of the freely suspended GALs.

Overall Picture of the Splitting Behavior

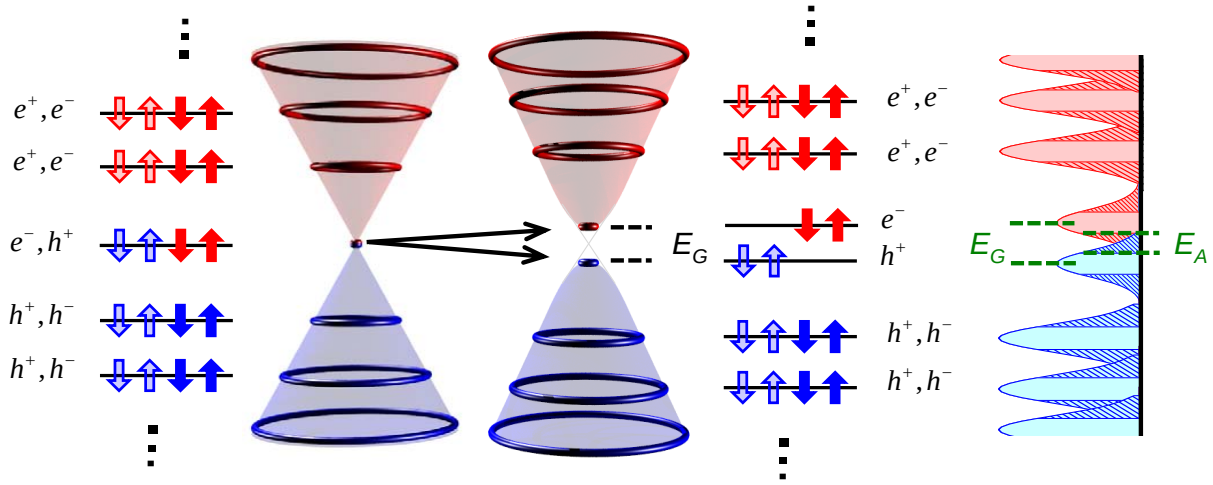

Figure 7.9: Schematic illustration of the impact of the nanohole array on the band structure of graphene under applied B-field. Electron levels are drawn red and hole levels blue. The spin degree of freedom is indicated by the direction of the arrows. The chirality is visualized by filled and transparent arrows. On the right, the corresponding Landau level density of states is depicted, with the actual LL gap E_G and the activation gap E_A (both in dark green).

As shown above, the GAL introduces a finite zero-field E_G^0, such that the two Dirac cones of pristine graphene connected at the CNP become separated. This gap opening induces a transition from a linear to a parabolic dispersion of the band structure in the vicinity of the gap.
In figure 7.9 the parabolic dispersion scenario is combined with the observed valley splitting in order to illustrate the LL structure and DOS of the GALs. At low magnetic fields, the

activation measurements reveal pure hopping conduction via localized states in the gap. Only for higher magnetic fields the band gap is manifested in the temperature dependent conductivity, with a gap size that increases linearly with magnetic field due to the parabolic dispersion of the lowest LL. Under applied B-field, the charge carrier density condenses into LLs, and the lowest LL splits into an electron level (red arrows) and a hole level (blue arrows) of opposite chirality (dark and light arrows), which corresponds to valley polarization in the lowest LL. The divergence of the Hall resistance in the gap region proves that a valley-first split scenario must apply, whereas the spin degeneracy is preserved as concluded from the absence of plateaus at filling factors $\nu = \pm 1$, which can be ascribed to low quality of the 100 nm spacing GAL sample (figure 7.8(a)). It will be shown in the following that for the highest quality samples an additional, although weaker spin splitting on top of the valley splitting can be observed.
By contrast, the B-field behavior of the higher LLs remains unaffected and mirrors the behavior of pristine graphene. Overall, it follows that only the two levels originating from the $N = 0$ LL reside within this parabolic dispersion region, whereas the higher ($N \neq 0$) LLs remain in the linear dispersion regime.

Additional Spin Splitting in Highest Quality Samples

Besides the valley splitting of the $N = 0$ LL, signatures of additional, weak spin splitting can be detected in the samples of highest quality. Specifically, a $\nu = 1$ plateau appears at h/e^2 in the Hall resistance, as discernable in the fan diagrams for sample 9249_$D2$ (200 nm) and 9139_$D2a$ (100 nm suspended) in figure 7.10a) and b) respectively. For the suspended sample, the spin splitting is most pronounced and already appears above $\approx 6\ T$. Figure 7.10b) shows a zoom into the hole regime of the sample.
This spin splitting can be explained in the framework of the parabolic dispersion close to the gap upon inclusion of a complementary Zeeman term:

$$\pm \frac{1}{2} g^* \mu_B B, \tag{7.14}$$

with g^* as the effective electron g-factor in equation 7.11. The Zeeman energy leads to an additional term $\pm g m_{eff} eB/4\alpha\pi\hbar$ in equation 7.13. The additional splitting is exemplified in figure 7.10, where the red solid lines represent the higher LL with the linear dispersion. The black lines highlight the behavior of the zeroth LL, in which case either a pure valley-split gap (solid lines) or also the Zeeman term (equation 7.14) is included.
For each of the devices, both the fits with the negative and the positive sign of the Zeeman term yield an identical zero-field gap E_g^0 and m_{eff} (see previous section), such that the only remaining fit parameter is the g-factor. Fitting yields a g-factor of $g^* = 6$ for the 200 nm GAL and $g^* = 5$ for the 100 nm suspended sample. These values are appreciably larger than the free electron g-factor ($g = 2$), which might be explained by electron-electron exchange interactions, in analogy to the 2D gas in semiconductor heterojunctions [164,165]:

$$E_{ex}^0 = \left(1 - \frac{g}{g^*}\right) \sqrt{2\pi}\Gamma. \tag{7.15}$$

Furthermore, the spin splitting also has an influence on the determination of the band gap from the LL fans. If spin splitting is included, the LL broadening nominally decreases to $\Gamma = 60\ K$ for the 200 nm spacing sample, and $\Gamma = 20\ K$ in case of the suspended 100 nm spacing sample. These values are derived from the B-field at which the spin splitting becomes comparable to the LL broadening and hence observable. This is the case at $B \approx 6\ T$ (spin splitting $\approx 20\ K$) for the 100 nm suspended sample and $B \approx 15\ T$ (spin splitting $\approx 60\ K$) for the 200 nm sample. From the LL broadening the respective exchange energies of $E_{ex}^0 = 100\ K$ and $E_{ex}^0 = 30\ K$ can be calculated, which are in good agreement with $E_{ex}^0 = 130\ K$ reported for pristine graphene [163].

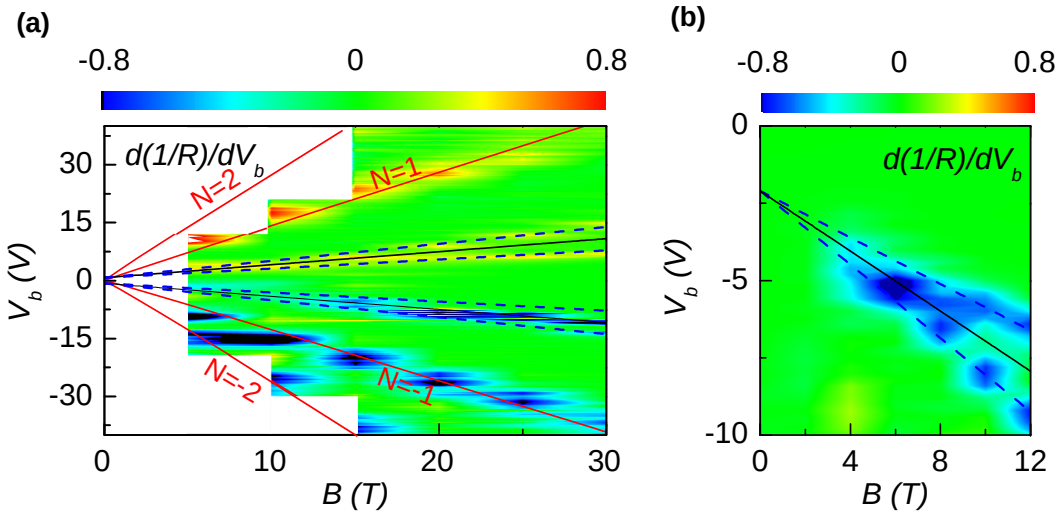

Figure 7.10: Fans diagrams, comprising a plot of $d(1/R)/dV_b$ as a function of magnetic field and gate voltage at $T = 1.4\ K$, for (a) the 200 nm spacing sample 9398_$D4$ and (b) the 100 nm suspended GAL 9139_$D2a$. Both samples were measured in lateral configuration instead of Hall bar, which renders the derivative of the inverse resistance negative (positive) below (above) the CNP.

Chapter 8

Summary and Outlook

8.1 Band gap opening and interaction effects

In summary, two different graphene-based model systems for band gap opening have been studied, namely bilayer graphene in electric and magnetic fields, as well as GALs with different lattice geometries up to high magnetic fields.
In case of bilayer graphene, besides the band gap opening induced by the out-of-plane electric field, also an unexpected spontaneous gap already present at zero magnetic and electric field is found. By comparison, charge transport in the GAL structures at low magnetic fields is governed by different variable range hopping regimes, which arise from the presence of localized states, while a fundamental band gap becomes observable only in the high magnetic field range. However, the data gained under high B-field indicate that already without applied field an energy gap is present, although it is obscured by the localized states. By studying a set of GALs with different geometry it could be shown that similar to graphene nanoribbons, the confinement and thus the GAL geometry plays a crucial role. In contrast to the GAL geometry, no noticeable influence of the geometrical arrangement of the nanoholes (cubic vs. hexagonal) is observed. The localized states in the GALs lead to 2D conduction either via Efros-Shklovskii variable range hopping (ES-VRH) in case of small nanohole spacing or Mott VRH for large nanohole spacing, both of which are operative at low magnetic fields. Which hopping mechanism is dominant depends on the strength of the Coulomb interaction between the localized states. Stronger Coulomb interactions cause the opening of a soft gap in the localized density of states, the so-called Coulomb gap. A more complete picture regarding the localization in the samples could be gained from thermal activation measurements in the VRH regimes, which provide direct access to the degree of localization in the samples. These data reveal that strong localization with short localization lengths, implying short hopping distances and large hopping energies, favors ES-VRH. By contrast, the 2D Mott VRH regime is characterized by weaker localization and correspondingly larger localization lengths. In general, the hopping distance from one localized state to another is found to be 1-2 times larger than the nanohole distance. Thus, charge carriers hop from one nanohole edge to the nearest

or next-nearest neighboring nanohole (assuming that the localized states are located at the nanohole edges). This scenario is consistent with the observation that the localization increases upon decreasing the nanohole separation.

Besides the gap-opening mechanism, the tuneability of the gap differs between the two model systems. For bilayer graphene, the gap size is determined by the strength of the vertical electric field applied to the suspended sheet. With the aid of opposing bottom and top gates, we achieve independent control of the vertical electric field and the charge carrier density in the sheet. In the investigated devices, the gap is largest for zero charge carrier density and the resistance increases exponentially with electric field. Although the maximum observed resistance increase due to the opened band gap is larger than reported for flakes embedded into dielectrics, the experimental gap size is still considerably smaller than predicted by theory. This difference might be assigned to the disorder potential, which is significantly reduced in the suspended vs. substrate-supported graphene bilayers, albeit it does not reach the intrinsic mobility limit. Another contributing factor could be the random edge termination of the flakes. Tuning of the carrier density by the electric field is limited by the break-through voltage of the dielectric, and for the suspended sheets also by their mechanical stability, as they are bent toward the gates at high vertical fields. For the GALs, it could be demonstrated that in addition to the nanohole separation also the doping level influences the gap. In particular, the size of the Coulomb gap increases linearly with decreasing charge carrier concentration. With increasing carrier density, first a transition occurs from ES VRH to 2D Mott VRH, followed by a transition to a weak localization regime. The latter regime lacks an exponential temperature dependence of the resistance, and also the phase coherence length is notably reduced compared to the VRH regime. A third possibility to tune the gap, besides adjusting the nanohole separation and carrier density, is to apply an external magnetic field. In GALs with small nanohole spacing, which without applied B-field feature ES VRH, this hopping mechanism prevails up to moderate magnetic fields, above which a transition to Mott VRH takes place. The B-field, at which this transition occurs due to decreased Coulomb interactions between the carriers of the localized states, decreases with increasing nanohole separation. The reason why an applied B-field reduces these interactions is shrinking of the wave functions and the resulting reduced overlap between them. Conduction via ES-VRH at moderate magnetic fields could be observed in the present thesis for the first time, most likely because in previous studies the interactions have been suppressed by the magnetic field, such that Mott VRH dominated. The existence of ES-VRH under these conditions had been expected by percolation theory. Upon further increasing the magnetic field, the transport mechanism changes from Mott VRH to activated transport with a gap, whose size depends linearly on the B-field. The transition between the two regimes is continuous, since the VRH regime is dominant in the low temperature range, while the opposite holds in the high temperatures range. Accordingly, even at moderate magnetic fields, almost the entire accessible temperature range can be described by activated transport.

The device quality, as expressed by the carrier mobility, proved to play a crucial role,

as reflected by its significant influence on the measured gap size in both systems, i.e., bilayer graphene as well as the GALs. Improvement of carrier mobility is of particular importance for bilayer graphene which is more sensitive against adsorbates and surface contaminants than monolayer graphene. Here, such improvement was achieved by suspension and subsequent current annealing of the flake. In contrast to bilayer graphene embedded in bottom and top gate dielectrics, which deteriorate the carrier mobility, the suspended sheets displayed the expected exponential resistance increase with electric field. Another benefit of the increased carrier mobility is that interaction effects of the involved charge carriers become visible already at low magnetic fields. In bilayer graphene, electron-electron exchange interaction is enhanced compared to monolayer graphene, which leads to a degeneracy lifting in the Landau level structure. As a consequence, the unique nature of the charge carriers becomes directly observable, particularly in the form of a LL splitting that increases with rising B-field. Similar to monolayer graphene, the splitting hierarchy in bilayer graphene most likely involves first the spin, followed by the valley, and - for bilayer graphene - additionally the orbital degree of freedom. Along with the magnetic field, also the electric field influences the LL spectrum of bilayer graphene. In fact, the electric field-induced band gap opening is associated with valley polarization, since the upper and lower graphene layers are directly correlated to the valley degree of freedom in the lowest LL, wherein electrons and holes possess opposite chirality. Moreover, the different slopes of the LL energies in electric field for the two valley polarizations lead to crossing of the LLs, with a canted antiferromagnetic or spin-polarized phase dominating for high magnetic fields and a layer (valley)-polarized phase under high electric fields. Surprisingly, at low magnetic and electric fields another high resistance phase could be detected, which even persists down to zero fields. The origin of this "spontaneous" gap is still subject to debate. One plausible explanation might be breaking of the time reversal or rotational symmetry. In general, symmetry breaking in bilayer graphene is facilitated due to the enhanced exchange interactions of its charge carriers.
Like for bilayer graphene, also in GALs exchange interactions affect the charge transport mechanism. In this case, the effect of carrier mobility is evidenced by comparing devices with different doping levels, as controlled either by suspension and subsequent current annealing of the flake, or by in-situ annealing of the finished device. These methods also allow comparing the same device before and after annealing, which demonstrates that an increased device quality leads to stronger localization with an increased Coulomb gap. The GAL devices of highest carrier mobility were found to clearly display the Aharanov-Bohm effect that arises to due quantum interference when the devices are brought into the quantum Hall regime. The opening of fundamental band gap under high magnetic fields hints back to the presence of a zero-field gap that is introduced by the spatial confinement. The resulting separation of electrons and holes induces a polarization of the valley degree of freedom for the lowest LL. Since valley splitting occurs before spin splitting, the splitting sequence is reverse compared to that in pristine graphene. Such valley-first splitting of the zero energy LL, as consolidated by the observed divergence of the Hall resistance around the CNP, could be detected in this thesis for the first time. The size of the valley-polarized band gap was found to scale linearly with magnetic field. We explain this magnetic field

dependence, as well as the zeroth LL splitting, by a transformation of the band structure around the Dirac point. While in bilayer graphene, the parabolic dispersion is transformed into a Mexican hat-shaped dispersion, in the GALs, the originally linear dispersion changes to a parabolic one. The latter transformation is accompanied by a change of the nature of the charge carriers, whereupon they assume a mass. In comparison, the higher LLs remain unaffected and preserve the typical spacing and position like in pristine graphene. As expected, the determined LL broadening is smallest for the suspended GALs devices owing to their high carrier mobility. Analogous to the high quality bilayers, a complete degeneracy lifting can be observed in such samples, together with a weaker spin splitting on top of the valley-first splitting.

8.2 Outlook

The present findings demonstrate the opening of a tuneable band gap in both, bilayer graphene subjected to a vertical electric field as well as GAL devices placed within a magnetic field. From an application perspective, an ideal field-effect transistor would be operated at room temperature with high charge carrier conductance in the "on" state and negligible conductance in the "off" state. Due to its extraordinary charge carrier mobility which is almost independent of carrier concentration and only weakly decreases with rising temperature, graphene is a promising component for such devices. The measurements performed in this thesis reveal that enhancing the mobility, for instance by suspending and/or annealing of the sheet, enhances the opened gap. Especially in the case of bilayer graphene, where the band gap scales with the external magnetic field, further improvement may be achieved in the future by implementation of a sandwich structure, wherein the flake is embedded between two insulating hBN layers. Indeed, it has been shown that graphene on hBN as underlying substrate can exhibit equally high mobility as suspended flakes which approach the intrinsic limit given by phonon-scattering [78, 79]. As a further advantage, such structures offer higher device stability and thus the possibility to apply high gate voltages and electric fields. Research in this direction is carried out intensively [104, 166, 167], although device fabrication becomes increasingly complicated. Another challenging goal is to gain better control over the confinement-induced gap in the GALs. In particular, structuring on the nm scale poses a serious challenge especially with regard to large scale device fabrication and integration. The top-down patterning of narrow structures is notoriously accompanied by the introduction of defects and edge roughness, both of which reduce the mobility. Bottom-up strategies in principle promise well-defined edges and strong spatial confinement [168], however, they are still in the very early stage of fundamental research and hence not yet available for integration into devices.
Ideally, switching of the devices should be achievable with only a small energy cost rather than the need to apply high fields and voltages. Also in this respect graphene is highly promising since due to the chiral nature of its charge carriers, ballistic edge channel conduction is protected and persists up to room temperature. As a consequence, LL formation becomes accessible even at elevated temperatures. Provided that the device mobility is

sufficiently high, it should principally also be possible to gain access to the additional degrees of freedom of graphene's charge carriers under ambient conditions. This perspective expands the current fundamental research interest in different symmetries, phases and quasi-particle character toward exploiting the LL splitting not only for conductance switching, but also to achieve device operation based upon the quasi-particle polarizations, most prominently in the form of graphene-based spintronic or valleytronic devices such as gate tuned spin- or valley filters or beam splitters [169–171]. Graphene's large spin coherence length renders it into a close-to-ideal component of such devices. Thus, the findings of this thesis may not only open new avenues towards graphene-based devices, but especially the observed band-structure transformation and alteration of the quasi-particle character in the GALs might have important implications for the realization of all-graphene semiconductor devices that rely upon a band gap introduced by spatial confinement.
Another issue for the implementation of graphene into technologically useful devices, which has not yet been addressed in this work, is device scalability. While devices based on mechanically exfoliated graphene are the first choice for exploring fundamental aspects and fabricating proof-of-principle devices as investigated in this work, alternative synthesis methods for graphene synthesis are needed for large scale production. Especially promising in this respect is epitaxial graphene on SiC, which reaches mobilities of the order of $20,000\ cm^2V^{-1}s^{-1}$ [55]. Gap opening in such type of graphene can be achieved on a large scale by hydrogenation [172–174]. Additionally to gap opening, covalent functionalization by hydrogenation has been predicted to induce ferromagnetism in graphene [175]. Since the underlying SiC does not allow for electrostatic gating, we have carried out first test measurements by magnetic force microscopy in order to locally probe possible spin alignment in hydrogenated epitaxial graphene.

8.2.1 Hydrogenated Epitaxial Graphene on SiC

Hydrogenation

Graphene can be produced by thermal decomposition of SiC (at $\approx 1600°C$) under UHV or inert gas conditions, where the silicon sublimes and carbon-rich regions form that increase in size and finally merge into the graphene layer [57]. Although graphene sheets of reasonable quality can be obtained in this way, it has proven difficult to grow homogeneous layers of controllable thickness. Figure 8.1 shows an AFM image of epitaxial graphene grown on an insulating 6H-SiC substrate following the method in [57]. Several few micrometer wide terraces are visible due to a slight miss-cut of the SiC substrate [176,177]. At the step edges a second layer is formed, resulting in a narrow stripe of bilayer graphene [57]. Below the graphene layer a carbon-rich phase, the insulating, so-called buffer layer [178, 179], is located which decouples the layers from the SiC substrate [180]. After growth, the graphene film in figure 8.1 is subjected to hydrogen exposure in an UHV chamber. The resulting hydrogen coverage of the graphene film depends on the hydrogenation time, and might differ between the monolayer and bilayer graphene regions.

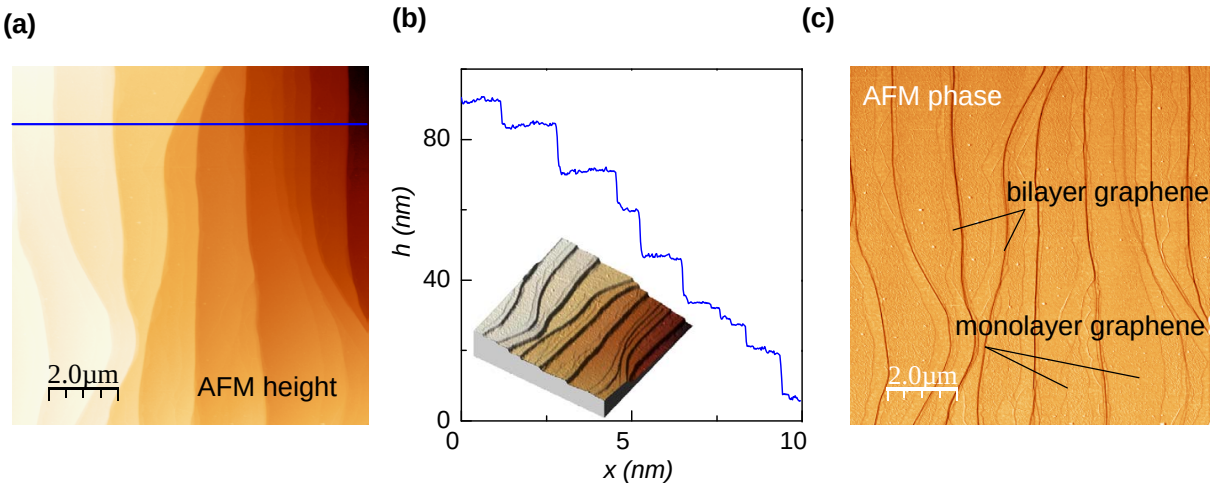

Figure 8.1: Formation of partially hydrogenated graphene on SiC, probed by tapping mode AFM. (a) Topographic image revealing a terrace structure with $\approx 10\ nm$ step height. (b) Line cut along the line in panel (a) and three-dimensional view of the terrace steps. (c) In the phase image, the areas covered by monolayer and bilayer graphene at the terrace edges can be distinguished.

Magnetic Properties

Figure 8.2 shows regions of monolayer and bilayer graphene (at the terrace edges of the SiC substrate) after 30 *min* of hydrogen treatment. Magnetic force microscopy (MFM) measurements are performed at a constant lift height of 50 *nm* using a magnetic Co-Cr coated tip with force constant $k = 2.8\ N/m$ under ambient conditions. The quality factor of the tip is around 230. The MFM data can be directly correlated with the topography data taken in tapping mode (figure 8.2(a)). In the phase shift of the MFM signal (see figure 8.2(b) and (c)), the monolayer (ML) and bilayer (BL) graphene areas show a different contrast, which indicates a different magnetization of the two regions. This might arise from different hydrogen coverage [181, 182]. The sample can be magnetized by placing it on the north ($+B$) or south pole ($-B$) of a permanent magnet before putting it back into the MFM setup. This leads to inversion of the MFM signal ($-14.375 \pm 0.175\ deg$), with the monolayer always exhibiting larger magnetization than the bilayer regions. Magnetizing the sample in the opposite direction ($+B$) re-establishes the original MFM signal ($+3.225 \pm 0.175\ deg$). The line cuts of the MFM scans are obtained by averaging over the lines in the indicated region. The dirt particle (circled area) in the center of the images serves as reference point in the scans. Similar to the step edges, it is also visible in the MFM scans and does not change sign upon sample magnetization in different directions, indicating that it most likely arises due to crosstalk with the topography signal.
These first test measurements indeed confirm a magnetic moment of the hydrogenated graphene on SiC. Furthermore, they reveal a different magnetization for the graphene monolayer and bilayer regions.

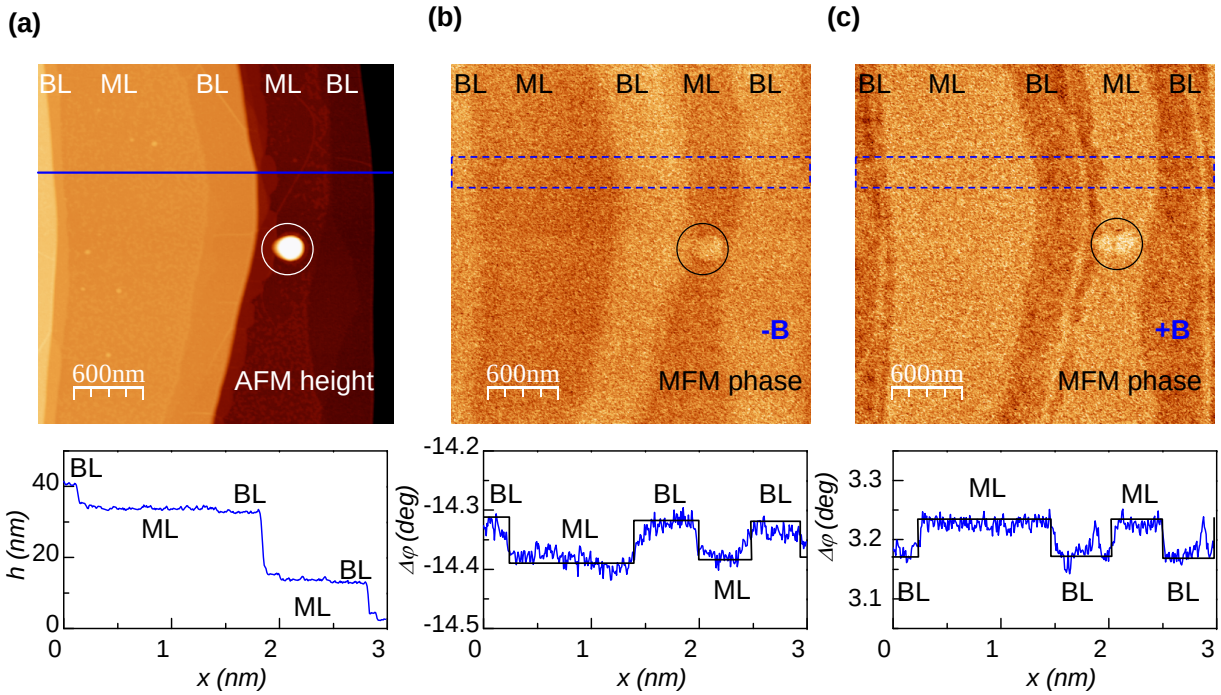

Figure 8.2: Magnetic force microscopy images of hydrogenated graphene on SiC (sample $GM16$) (a) AFM scan in tapping mode, taken before the MFM scan. (b) MFM phase image recorded after magnetizing the sample by placing it on the south pole of a permanent magnet ($-B \approx -300\ mT$). (c) MFM phase image acquired after reversing the magnetization on the north pole of a permanent magnet ($+B \approx 300\ mT$).

8.2.2 Scanning Photocurrent Microscopy (SPCM) at Low Temperatures

Visualization of the local potential distribution is an important task, since the performance of graphene devices depends sensitively on the potential distribution as well as edge effects (e.g., their chemical termination or edge channel conduction). To explore these effects in future experiments, the method of scanning photocurrent microscopy (SPCM) is expanded to low temperatures by combining scanning confocal microscopy with low-temperature magnetotransport measurements. At room temperature and zero B-field, SPCM has already been used to study contact and edge effects in graphene transistor devices [183]. At liquid He temperatures, the technique has proved to be able to spatially resolve the LL structure [184], as well as hot carrier effects (i.e., the Seebeck effect) in pristine graphene [185]. Figure 8.3 shows first test SPCM measurements performed at low temperature on a 100 nm spacing GAL contacted in 4-probe configuration. The reflection signal (RS) is recorded simultaneously with the photocurrent I_{photo}, such that the scanning position can be directly correlated with the photocurrent signal generated. In the measurement, no source-drain bias and zero magnetic field is applied. The photocurrent image displays two main pho-

tocurrent lobes of opposite sign. Similar signals observed at room temperature have been attributed to potential steps at the contacts.

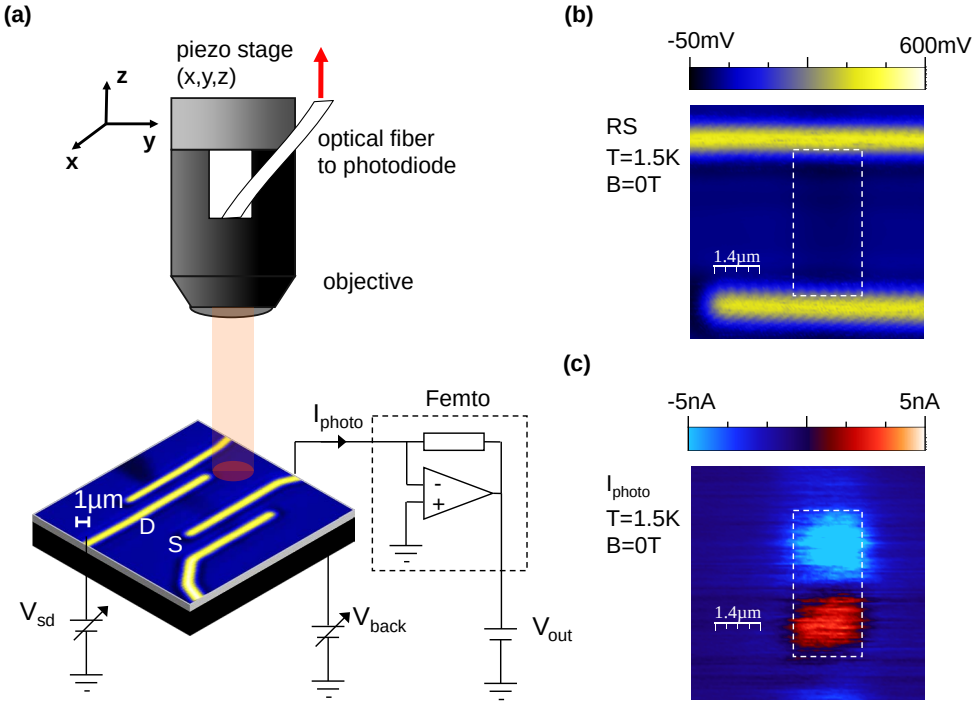

Figure 8.3: Scanning photocurrent microscopy at low temperatures ($T = 1.5\ K$, $B = 0\ T$, $V_{back} = 0\ V$, nominal laser power $P = 0.04\ mW$, sample time $t = 25\ ms$) on a 100 nm spacing GAL (sample 0216_D4) highlighted by the white dashed line. (a) Schematic illustration of the measurement setup allowing for simultaneous capturing of the reflection signal (RS) and the photocurrent signal (I_{photo}). (b) Reflection image of the inner contacts. (c) Photocurrent image of the same area as in panel (b).

The first SPCM measurements shown here confirm the proper function of the setup and underline the potential of this technique for future measurements on graphene devices.

Appendix A

Sample Catalogue

A.1 List of Samples

The following table lists all samples of which data is shown in this work. The list includes the sample names, their composition and/or treatment, as well as their charge neutrality point (CNP) position if applicable.

sample name	type	description	CNP
8855_$D2a$	graphene on Si/SiO_2	non-structured	$V_{CNP} = 8.0\ V$
9139_$D2b$	suspended graphene current annealed	non-structured	$V_{CNP} = 0.0\ V$
9001_$D3$	suspended graphene current annealed	non-structured	$V_{CNP} = 0.0\ V$
10268_$D2$	graphene on Si/SiO_2	Hall bar	$V_{CNP} = 15.5\ V$
10265_$D1$	graphene on Si/SiO_2	Hall bar	$V_{CNP} = 30.0\ V$
10265_$D2$	graphene on Si/SiO_2	Hall bar	$V_{CNP} = 33.0\ V$
8818_$D3$	graphene on Si/SiO_2	Corbino disk Outer diameter $d_o = 2.5\ \mu m$ Inner diameter $d_i = 1.5\ \mu m$	$V_{CNP} = 5.6\ V$
8851_$D1$	graphene on Si/SiO_2	Corbino disk Outer diameter $d_o = 2.5\ \mu m$ Inner diameter $d_i = 1.5\ \mu m$	$V_{CNP} = -1.35\ V$

sample name	type	description	CNP
8851_$D7$	graphene on Si/SiO_2	Corbino disk Outer diameter $d_o = 2.5\ \mu m$ Inner diameter $d_i = 1.5\ \mu m$	$V_{CNP} = -1.35\ V$
8813_$D2$	graphene on Si/SiO_2	Corbino disk Outer diameter $d_o = 2.5\ \mu m$ Inner diameter $d_i = 1.5\ \mu m$	$V_{CNP} = -2.0\ V$
$EP070710a$_$D5$	suspended bilayer graphene current annealed	Hall bar	$V_{CNP} = 0.5\ V\ V$
$EP082910a$_$D6$	suspended bilayer graphene current annealed	Hall bar with top gate	$V_{CNP} = 0.55\ V$
$EP082910a$_$D11$	suspended bilayer graphene current annealed	Hall bar with top gate	$V_{CNP} = 0.0\ V$
8855_$D1$	GAL on Si/SiO_2	100 nm spacing square lattice	$V_{CNP} = 10.6\ V$
8855_$D4$	GAL on Si/SiO_2	100 nm spacing square lattice	$V_{CNP} = 13.8\ V$
8855_$D2b$	GAL on Si/SiO_2	200 nm spacing square lattice	$V_{CNP} = 10.0\ V$
8854_$D3a$	GAL on Si/SiO_2	80 nm spacing square lattice	$V_{CNP} = 11.5\ V$
8854_$D1$	GAL on Si/SiO_2	100 nm spacing hexagonal lattice	$V_{CNP} = 12.0\ V$
8817_$D5$	GAL on Si/SiO_2	100 nm spacing hexagonal lattice	$V_{CNP} = 16.5\ V$
8817_$D4$	GAL on Si/SiO_2	100 nm spacing square lattice	$V_{CNP} = 18.0\ V$
9249_$D2$	GAL on Si/SiO_2	200 nm spacing square lattice	$V_{CNP} = 8.5\ V$
9249_$D3a$	GAL on Si/SiO_2	100 nm spacing square lattice	$V_{CNP} = 12.5\ V$
9249_$aD2$	GAL on Si/SiO_2	200 nm spacing square lattice annealed	$V_{CNP} = 5.5\ V$

sample name	type	description	CNP
9249_$aD3a$	GAL on Si/SiO_2	100 nm spacing square lattice annealed	$V_{CNP} = 5.5\ V$
9139_$D2a$	suspended GAL current annealed	100 nm spacing square lattice	$V_{CNP} = -1.0\ V$
9398_$D2$	GAL on Si/SiO_2	100 nm spacing square lattice Hall bar geometry	$V_{CNP} = 16.0\ V$
9398_$D4$	GAL on Si/SiO_2	200 nm spacing square lattice	$V_{CNP} = 16.0\ V$
$GM16$	mono- and bilayer graphene on SiC	hydrogenated 30 min	-
$GN05$	mono- and bilayer graphene on SiC	hydrogenated 30 min	-
0216_$D4$	GAL on Si/SiO_2	100 nm spacing square lattice	$V_{CNP} = 11.0\ V$

Table A.1: Sample catalog. The samples are listed according to the order in which they appear in this work.

Appendix B

Combined Heliox VL/ Attocube CFM Setup Specifications

Cool down from room temperature to liquid He temperature

Cool down of the Dewar involves the following steps (see also [186]):

1. Evacuating the OVC with an oil-free roughing pump and subsequent pumping with a turbomolecular pump to a pressure of $p < 1 \cdot 10^{-5}\ mbar$, and leakage rate $< 1 \cdot 10^{-8}\ mbar \cdot l/s$.

2. Filling of main bath with liquid nitrogen (maintain $p \approx 0.1\ bar$).

3. Pump liquid nitrogen from the main bath to the nitrogen shield reservoir by connecting the main bath with the nitrogen shield, while simultaneously pressurizing the main bath from the exhaust.

4. Flush the main bath with helium gas when all nitrogen is transferred to the shield by filling He up to a pressure of 1000 $mbar$ and subsequent pumping to 500 $mbar$. Repeat the flushing, with reducing the end pressure to 200 $mbar$, 100 $mbar$, and $\approx 0\ mbar$, respectively, in the following flushing cycles. Repeat the flushing a few times with the lambda fridge needle valve open, and close it after the flushing at 1000 $mbar$.

5. Fit the main bath exhaust with an 1 bar overpressure valve and then fill the liquid nitrogen shield with liquid nitrogen and the main bath with liquid helium.

6. Connect the recovery line.

The helium level in the main bath can be checked by monitoring the resistances at the 12 pin Fischer connector located at the lambda fridge pumping exit. The important resistances are summarized in table B.1:

measured resistance	pins	@ room temperature	@ 77 K	@ 4.2 K
magnet	magnet leads	49 Ω	39.8 Ω	-
magnet isolation	magnet to ground	∞	∞	∞
switch heater	pin 9,10	120.2 Ω	118.4 Ω	-
spare switch heater	pin 8,10	120.2 Ω	118.4 Ω	-
switch heater isolation	pins 8,9,10 to ground	∞	∞	∞
R1 ($\approx$ 10 cm above lambda fridge coil)	pin 3,4	189.7 Ω	217.2 Ω	1270 Ω
R2 (at lambda fridge coil)	pin 3,5	192.5 Ω	220.2 Ω	1314 Ω
R3 (top of magnet)	pin 3,6	187.4 Ω	215 Ω	1300 Ω

Table B.1: Resistances measured at the magnet or the 12 pin fisher connector located at the lambda fridge pumping exit, measured at three different temperatures.

Temperature Sensors for the two inserts

The different temperature sensors common to the two inserts including their location and range are given in the following table B.2. Additional temperature sensors of the CFM insert are listed in table B.3.

location	sensor type	sensor range
Sorb	Allen-Bradley	1.2 K - 240 K
1 K-pot	RuO	< 7 K
^3He pot	RuO	< 7 K
^3He pot	Cernox	1.4 K - 300 K

Table B.2: Properties of the temperature sensors of the cryostat inserts.

location	sensor type	sensor range
cold plate (sample)	RuO	< 7 K
cold plate (sample)	$PT1000$	300 K - 400 K

Table B.3: Specifications for the additional temperature sensors of the CFM insert.

Calibration of the Cernox sensor

The calibration of the Cernox sensor has to be adapted to the respective insert in use (for a complete description see also The ITC503 RAM SETUP DIALOG in [187]). In principle the calibration of the sorb sensor (115 Ω and 110 Ω correspond to 240.9 K for the rotator and the CFM insert, respectively, whereas 1100 Ω is the low temperature reference point at

4.4 K) should also be adapted to the respective insert used. However, since the latter sensor is not used for accurate temperature sensing this step is not crucial. A recalibration for the RuO sensors is not necessary since the CFM insert possesses an additional RuO sensor near the sample space, which is read out via a Lakeshore temperature controller. The calibration is done with the ITC503 control using the MMS program . The temperature/resistance conversion files for the two inserts are already stored in the ITC. After loading the files, the calibration is performed via the following steps:

1. Setup→memory→get→load from table file (C070 for the rotator insert and C439 for the CFM insert). Assign range→channel3→ok→put.

2. Storing the settings on the ITC is done in local mode: local→Limit+LOC/REM. Then switch of the ITC. Change the hardware configuration of the ITC switches by removing the top cover and setting the black switch of sensor 3 into the up-position for the CFM insert, and the down-position for the rotator insert.

3. Switch the ITC back on and use a decade box connected to sensor 3 on the ITC to adjust the temperature when providing the respective resistance (see X75439.dat for the CFM insert and X76070.dat for the rotator insert). This should be done for one low and one high temperature (e.g. 4 K and 300 K) by pressing Calc+Raise/Lower.

4. Store the settings by pressing Limit+LOC/REM and check whether another resistance is consistent with the temperature given in the respective table.

B.1 Rotator Insert

Angle accuracy

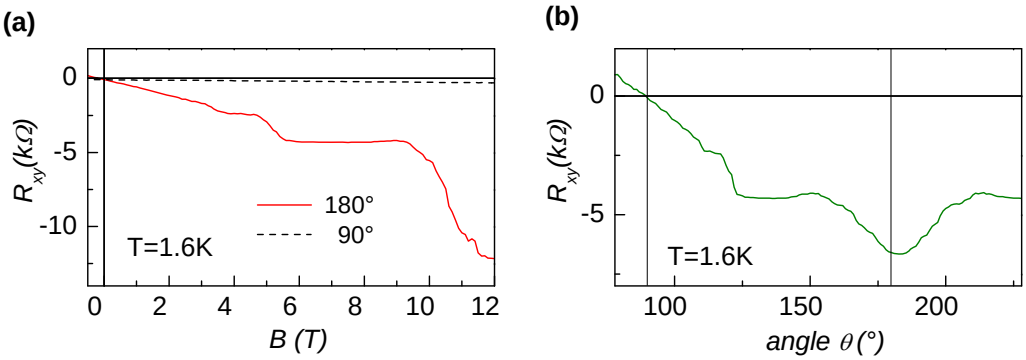

Figure B.1: Hall resistance of graphene Hall bar sample 10265_$D1$ at $T = 1.6\ K$ and $q = 1.08 \cdot 10^{12}\ cm^{-2}$. (a) Hall resistance at angles 90° and 180°. (b) Hall resistance as a function of angle at $q = 1.08 \cdot 10^{12}\ cm^{-2}$ and $B = 10.5\ T$.

The angle accuracy can be checked by plotting the Hall resistance of the Hall bar versus the angle between surface normal of the substrate and the B-field direction. In figure B.1 this is exemplified for a carrier concentration of $q = 1.08 \cdot 10^{12}\ cm^{-2}$. The maximum absolute Hall resistance occurs at 182.2° and the minimum at 89.4°, indicating angle errors of 2.2° and 0.6°, respectively.

B.2 CFM Insert

Laser Intensity

In table B.4 the nominal power (NP) at the laser module is compared to the measured laser power (MP) at the objective and the measured reflection signal (RS).

NP (ACC100) (mW)	MP (nW)	RS gold marker (mV)	RS SiO_2 surface (mV)
0	15	-52	-52
0.01	90	-44	-50
0.02	272	-24	-46
0.03	828	23	-36
0.04	2020	139	-10
0.05	4070	346	36
0.06	7700	618	92
0.07	10800	924	148

Table B.4: Laser calibration of the diode laser (635 nm) with a Si/SiO_2 marker sample. The offset is $-52.7\ mV$.

Navigation

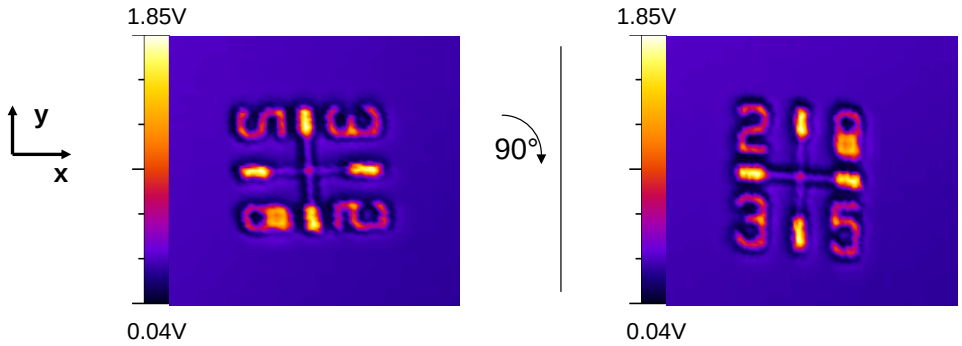

Figure B.2: Low temperature scan of a marker performed at $T = 1.5\ K$. The cross size is $9\ \mu m \times 9\ \mu m$ (sample 0216).

For the navigation from one device to the next on the same substrate a marker system based on numbers is used. The markers are positioned at a distance of 50 μm. The upper number counts the markers in the x-direction and the lower number in the y-direction, with the origin in the upper left corner of the substrate. Figure B.2 shows a scan of an individual marker acquired at $T = 1.6\ K$. To read out the marker correctly, it has to be rotated by 90° and mirrored. Table B.5 correlates the lever movement of the piezo control unit with the movement of a scanned feature and the objective.

axis	direction1		direction2	
x	lever	↑	lever	↓
	feature	←	feature	→
y	lever	↑	lever	↓
	feature	↓	feature	↑
z	lever	↑	lever	↓
	feature	↓	feature	↑

Table B.5: Lever movement of the piezo control unit, and corresponding movement of the scanned feature (x and y axis) or the objective (z-axis).

Measurement wiring at connector

Figure B.3 shows a schematic top view of the configuration at the connector for the sample wiring. The labels (as shown in panel (b)) have been removed to reach a lower pressure in the IVC. The pins for the measurement wiring are numbered. The pins for the positioners are labeled $P_{x,y,z}$, for the scanners $S_{x,y,z}$. While H denotes the heater wiring, TI, TV and S_2, S_3 represent the respective sample temperature sensors (PT1000 and RuO).

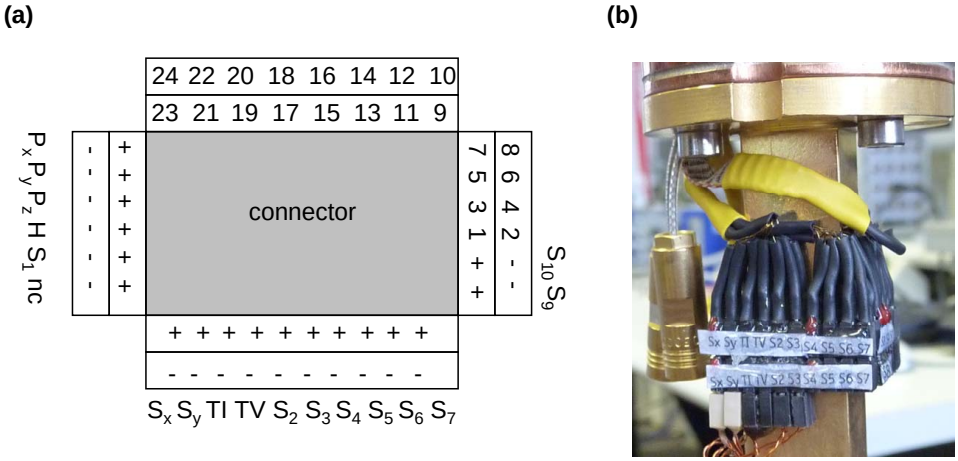

Figure B.3: Sample measurement wiring at connector. (a) Schematic sketch of the configuration of the pins. (b) Photograph of the connector part.

Bibliography

[1] M. Planck. The Nobel Prize in Physics, 1918.

[2] A. Einstein. The Nobel Prize in Physics, 1921.

[3] N. Bohr. The Nobel Prize in Physics, 1922.

[4] L. de Broglie. The Nobel Prize in Physics, 1929.

[5] W. Heisenberg. The Nobel Prize in Physics, 1932.

[6] E. Schrödinger and P.A.M. Dirac. The Nobel Prize in Physics, 1933.

[7] W. B. Shockley, J. Bardeen, and W. H. Brattain. The Nobel Prize in Physics, 1956.

[8] A. Y. Cho and J. R. Arthur. Molecular beam epitaxy. *Progress in Solid State Chemistry*, 10, Part 3(0):157–191, 1975.

[9] K. v. Klitzing, G. Dorda, and M. Pepper. New method for high-accuracy determination of the fine-structure constant based on quantized hall resistance. *Phys. Rev. Lett.*, 45:494–497, 1980.

[10] K. von Klitzing. The Nobel Prize in Physics, 1985.

[11] P. R. Wallace. The band theory of graphite. *Phys. Rev.*, 71:622–634, 1947.

[12] K. S. Novoselov, A. K. Geim, S. V. Morozov, D. Jiang, Y. Zhang, S. V. Dubonos, I. V. Grigorieva, and A. A. Firsov. Electric field effect in atomically thin carbon films. *Science*, 306(5696):666–669, 2004.

[13] K. S. Novoselov, D. Jiang, F. Schedin, T. J. Booth, V. V. Khotkevich, S. V. Morozov, and A. K. Geim. Two-dimensional atomic crystals. *Proceedings of the National Academy of Sciences of the United States of America*, 102(30):10451–10453, 2005.

[14] A. K. Geim and K. S. Novoselov. The Nobel Prize in Physics, 2010.

[15] H. W. Kroto, J. R. Heath, S. C. O'Brien, R. F. Curl, and R. E. Smalley. C60: Buckminsterfullerene. *Nature*, 318(6042):162–163, 1985.

[16] S. Iijima. Helical microtubules of graphitic carbon. *Nature*, 354(6348):56–58, 1991.

[17] F. D. M. Haldane. Model for a quantum Hall effect without Landau levels: Condensed-matter realization of the "parity anomaly". *Phys. Rev. Lett.*, 61:2015–2018, 1988.

[18] K. S. Novoselov, Z. Jiang, Y. Zhang, S. V. Morozov, H. L. Stormer, U. Zeitler, J. C. Maan, G. S. Boebinger, P. Kim, and A. K. Geim. Room-temperature quantum Hall effect in graphene. *Science*, 315(5817):1379, 2007.

[19] S. V. Morozov, K. S. Novoselov, M. I. Katsnelson, F. Schedin, D. C. Elias, J. A. Jaszczak, and A. K. Geim. Giant intrinsic carrier mobilities in graphene and its bilayer. *Phys. Rev. Lett.*, 100:016602, 2008.

[20] E. McCann. Asymmetry gap in the electronic band structure of bilayer graphene. *Phys. Rev. B*, 74:161403, 2006.

[21] J. B. Oostinga, H. B. Heersche, X. Liu, A. F. Morpurgo, and L. M. K. Vandersypen. Gate-induced insulating state in bilayer graphene devices. *Nat. Mater.*, 7(2):151–157, 2008.

[22] R. T. Weitz, M. T. Allen, B. E. Feldman, J. Martin, and A. Yacoby. Broken-symmetry states in doubly gated suspended bilayer graphene. *Science*, 330(6005):812–816, 2010.

[23] J. A. Fürst, T. G. Pedersen, M. Brandbyge, and A.-P. Jauho. Density functional study of graphene antidot lattices: Roles of geometrical relaxation and spin. *Phys. Rev. B*, 80:115117, 2009.

[24] Y.-W. Son, M. L. Cohen, and S. G. Louie. Energy gaps in graphene nanoribbons. *Phys. Rev. Lett.*, 97:216803, 2006.

[25] J. Eroms and D. Weiss. Weak localization and transport gap in graphene antidot lattices. *New J. Phys.*, 11:095021, 2009.

[26] A. K. Geim and K. S. Novoselov. The rise of graphene. *Nat. Mater.*, 6(3):183–191, 2007.

[27] A. H. Castro Neto, F. Guinea, N. M. R. Peres, K. S. Novoselov, and A. K. Geim. The electronic properties of graphene. *Rev. Mod. Phys.*, 81:109–162, 2009.

[28] A. K. Geim. Graphene: Status and prospects. *Science*, 324(5934):1530–1534, 2009.

[29] K. S. Novoselov, A. K. Geim, S. V. Morozov, D. Jiang, M. I. Katsnelson, I. V. Grigorieva, S. V. Dubonos, and A. A. Firsov. Two-dimensional gas of massless Dirac fermions in graphene. *Nature*, 438(7065):197–200, 2005.

[30] Y. Zhang, Y.-W. Tan, H. L. Stormer, and P. Kim. Experimental observation of the quantum Hall effect and Berry's phase in graphene. *Nature*, 438(7065):201–204, 2005.

[31] V. P. Gusynin and S. G. Sharapov. Unconventional integer quantum Hall effect in graphene. *Phys. Rev. Lett.*, 95:146801, 2005.

[32] D. P. DiVincenzo and E. J. Mele. Self-consistent effective-mass theory for intralayer screening in graphite intercalation compounds. *Phys. Rev. B*, 29:1685–1694, 1984.

[33] R. Saito, M. Fujita, G. Dresselhaus, and M. S. Dresselhaus. Electronic structure of graphene tubules based on C_{60}. *Phys. Rev. B*, 46:1804–1811, 1992.

[34] J. González, F. Guinea, and M. A. H. Vozmediano. Continuum approximation to fullerene molecules. *Phys. Rev. Lett.*, 69:172–175, 1992.

[35] N. Hamada, S.-I. Sawada, and A. Oshiyama. New one-dimensional conductors: Graphitic microtubules. *Phys. Rev. Lett.*, 68:1579–1581, 1992.

[36] H. Ajiki and T. Ando. Electronic states of carbon nanotubes. *Journal of the Physical Society of Japan*, 62(4):1255–1266, 1993.

[37] N. D. Mermin. Crystalline order in two dimensions. *Phys. Rev.*, 176:250–254, 1968.

[38] A. Fasolino, J. H. Los, and M. I. Katsnelson. Intrinsic ripples in graphene. *Nat. Mater.*, 6(11):858–861, 2007.

[39] P. Blake, E. W. Hill, A. H. Castro Neto, K. S. Novoselov, D. Jiang, R. Yang, T. J. Booth, and A. K. Geim. Making graphene visible. *Applied Physics Letters*, 91(6):063124, 2007.

[40] K. v. Klitzing, G. Dorda, and M. Pepper. New method for high-accuracy determination of the fine-structure constant based on quantized Hall resistance. *Phys. Rev. Lett.*, 45:494–497, 1980.

[41] K. v. Klitzing. The quantized Hall effect. *Physica B+C*, 126:242–249, 1984.

[42] B. I. Halperin. Quantized Hall conductance, current-carrying edge states, and the existence of extended states in a two-dimensional disordered potential. *Phys. Rev. B*, 25:2185–2190, 1982.

[43] M. Büttiker. Absence of backscattering in the quantum Hall effect in multiprobe conductors. *Phys. Rev. B*, 38:9375–9389, 1988.

[44] C. W. J. Beenakker. Colloquium: Andreev reflection and Klein tunneling in graphene. *Rev. Mod. Phys.*, 80:1337–1354, 2008.

[45] G. W. Semenoff. Condensed-matter simulation of a three-dimensional anomaly. *Phys. Rev. Lett.*, 53:2449–2452, 1984.

[46] K. S. Novoselov, E. McCann, S. V. Morozov, V. I. Fal'ko, M. I. Katsnelson, U. Zeitler, D. Jiang, F. Schedin, and A. K. Geim. Unconventional quantum Hall effect and Berry's phase of 2π in bilayer graphene. *Nat Phys*, 2(3):177–180, 2006.

[47] M. I. Katsnelson, K. S. Novoselov, and A. K. Geim. Chiral tunnelling and the Klein paradox in graphene. *Nat. Phys.*, 2(9):620–625, 2006.

[48] Y. Hernandez, V. Nicolosi, M. Lotya, F. M. Blighe, Z. Sun, S. De, I. T. T., McGovern, B. Holland, M. Byrne, Y. K. Gun'Ko, J. J. Boland, P. Niraj, G. Duesberg, S. Krishnamurthy, R. Goodhue, J. Hutchison, V. Scardaci, A. C. Ferrari, and J. N. Coleman. High-yield production of graphene by liquid-phase exfoliation of graphite. *Nat. Nano.*, 3(9):563–568, 2008.

[49] X. Li, G. Zhang, X. Bai, X. Sun, X. Wang, E. Wang, and H. Dai. Highly conducting graphene sheets and Langmuir-Blodgett films. *Nat. Nano.*, 3(9):538–542, 2008.

[50] A. T. N'Diaye, J. Coraux, T. N. Plasa, C. Busse, and T. Michely. Structure of epitaxial graphene on Ir(111). *New Journal of Physics*, 10(4):043033, 2008.

[51] P. W. Sutter, J.-I. Flege, and E. A. Sutter. Epitaxial graphene on Ruthenium. *Nat. Mater.*, 7(5):406–411, 2008.

[52] K. S. Kim, Y. Zhao, H. Jang, S. Y. Lee, J. M. Kim, K. S. Kim, J.-H. Ahn, P. Kim, J.-Y. Choi, and B. H. Hong. Large-scale pattern growth of graphene films for stretchable transparent electrodes. *Nature*, 457(7230):706–710, 2009.

[53] A. Reina, X. Jia, J. Ho, D. Nezich, H. Son, V. Bulovic, M. S. Dresselhaus, and J. Kong. Large area, few-layer graphene films on arbitrary substrates by chemical vapor deposition. *Nano Letters*, 9(1):30–35, 2009.

[54] X. Li, W. Cai, J. An, S. Kim, J. Nah, D. Yang, R. Piner, A. Velamakanni, I. Jung, E. Tutuc, S. K. Banerjee, L. Colombo, and R. S. Ruoff. Large-area synthesis of high-quality and uniform graphene films on copper foils. *Science*, 324(5932):1312–1314, 2009.

[55] C. Berger, Z. Song, X. Li, X. Wu, N. Brown, C. Naud, D. Mayou, T. Li, J. Hass, A. N. Marchenkov, E. H. Conrad, P. N. First, and W. A. de Heer. Electronic confinement and coherence in patterned epitaxial graphene. *Science*, 312(5777):1191–1196, 2006.

[56] W. A. de Heer, C. Berger, X. Wu, P. N. First, E. H. Conrad, X. Li, T. Li, M. Sprinkle, J. Hass, M. L. Sadowski, M. Potemski, and G. Martinez. Epitaxial graphene. *Solid State Communications*, 143:92–100, 2007.

[57] K. V. Emtsev, A. Bostwick, K. Horn, J. Jobst, G. L. Kellogg, L. Ley, J. L. McChesney, T. Ohta, S. A. Reshanov, J. Rohrl, E. Rotenberg, A. K. Schmid, D. Waldmann, H. B. Weber, and T. Seyller. Towards wafer-size graphene layers by atmospheric pressure graphitization of silicon carbide. *Nat. Mater.*, 8(3):203–207, 2009.

[58] A. C. Ferrari, J. C. Meyer, V. Scardaci, C. Casiraghi, M. Lazzeri, F. Mauri, S. Piscanec, D. Jiang, K. S. Novoselov, S. Roth, and A. K. Geim. Raman spectrum of graphene and graphene layers. *Phys. Rev. Lett.*, 97:187401, 2006.

[59] A. C. Ferrari. Raman spectroscopy of graphene and graphite: Disorder, electron-phonon coupling, doping and nonadiabatic effects. *Solid State Communications*, 143:47–57, 2007.

[60] C. Casiraghi. Doping dependence of the Raman peaks intensity of graphene close to the Dirac point. *Phys. Rev. B*, 80:233407, 2009.

[61] Y. Hao, Y. Wang, L. Wang, Z. Ni, Z. Wang, R. Wang, C. K. Koo, Z. Shen, and J. T. L. Thong. Probing layer number and stacking order of few-layer graphene by Raman spectroscopy. *Small*, 6(2):195–200, 2010.

[62] J. Martin, N. Akerman, G. Ulbricht, T. Lohmann, J. H. Smet, K. von Klitzing, and A. Yacoby. Observation of electron-hole puddles in graphene using a scanning single-electron transistor. *Nat. Phys.*, 4(2):144–148, 2008.

[63] E. Fradkin. Critical behavior of disordered degenerate semiconductors. *Phys. Rev. B*, 33:3263–3268, 1986.

[64] M. I. Katsnelson. Zitterbewegung, chirality, and minimal conductivity in graphene. *Eur. Phys. J. B*, 51:157–160, 2006.

[65] P. M. Ostrovsky, I. V. Gornyi, and A. D. Mirlin. Electron transport in disordered graphene. *Phys. Rev. B*, 74:235443, 2006.

[66] K. I. Bolotin, K. J. Sikes, Z. Jiang, M. Klima, G. Fudenberg, J. Hone, P. Kim, and H. L. Stormer. Ultrahigh electron mobility in suspended graphene. *Solid State Communications*, 146:351–355, 2008.

[67] E. H. Hwang, S. Adam, and S. Das Sarma. Carrier transport in two-dimensional graphene layers. *Phys. Rev. Lett.*, 98:186806, 2007.

[68] M. Ishigami, J. H. Chen, W. G. Cullen, M. S. Fuhrer, and E. D. Williams. Atomic structure of graphene on SiO_2. *Nano Letters*, 7(6):1643–1648, 2007.

[69] J. Moser, A. Barreiro, and A. Bachtold. Current-induced cleaning of graphene. *Applied Physics Letters*, 91(16):163513, 2007.

[70] S. Tanaka, H. Goto, H. Tomori, Y. Ootuka, K. Tsukagoshi, and A. Kanda. Effect of current annealing on electronic properties of multilayer graphene. *Journal of Physics: Conference Series*, 232(1):012015, 2010.

[71] X. Du, I. Skachko, A. Barker, and E. Y. Andrei. Approaching ballistic transport in suspended graphene. *Nat. Nano.*, 3(8):491–495, 2008.

[72] T. Ando. Screening effect and impurity scattering in monolayer graphene. *J. Phys. Soc. Jpn*, 75:074716–, 2006.

[73] K. Nomura and A. H. MacDonald. Quantum transport of massless Dirac fermions. *Phys. Rev. Lett.*, 98:076602, 2007.

[74] M. I. Katsnelson and A. K. Geim. Electron scattering on microscopic corrugations in graphene. *Phil. Trans. R. Soc. A*, 366:195–204, 2007.

[75] S. Fratini and F. Guinea. Substrate-limited electron dynamics in graphene. *Phys. Rev. B*, 77:195415, 2008.

[76] J.-H. Chen, C. Jang, S. Xiao, M. Ishigami, and M. S. Fuhrer. Intrinsic and extrinsic performance limits of graphene devices on SiO_2. *Nat. Nano.*, 3:206–209, 2008.

[77] E. H. Hwang, S. Adam, and S. Das Sarma. Carrier transport in two-dimensional graphene layers. *Phys. Rev. Lett.*, 98:18392–18397, 2007.

[78] C.R. Dean, A.F. Young, I. Meric, C. Lee, L. Wang, S. Sorgenfrei, K. Watanabe, T. Taniguchi, P. Kim, K. L. Shepard, and J. Hone. Boron nitride substrates for high-quality graphene electronics. *Nat. Nano.*, 5(10):722–726, 2010.

[79] C. R. Dean, A. F. Young, P. Cadden-Zimansky, L. Wang, H. Ren, K. Watanabe, T. Taniguchi, P. Kim, J. Hone, and K. L. Shepard. Multicomponent fractional quantum Hall effect in graphene. *Nat. Phys.*, 7(9):693–696, 2011.

[80] W. H. Haydl, R. J. Bojko, and L. F. Eastman. Air-bridge electron-beam lithography for coplanar millimeter wave circuits. *MRS Online Proceedings Library*, 260, 1992.

[81] M. A. Gritz, M. Metzler, J. Moser, D. Spencer, and G. D. Boreman. Fabrication of air bridges using electron beam lithography. *Journal of Vacuum Science & Technology B: Microelectronics and Nanometer Structures*, 21(1):332–334, 2003.

[82] E. Girgis, J. Liu, and M. L. Benkhedar. Fabrication of metallic air bridges using multiple-dose electron beam lithography. *Applied Physics Letters*, 88(20):202103, 2006.

[83] L. J. Van der Pauw. A method of measuring specific resistivity and Hall effect of discs of arbitrary shapes. *Philips. Res. Repts.*, 13:1–9, 1958.

[84] L. J. Van der Pauw. A method of measuring the resistivity and Hall coefficient of lammellae of arbitrary shape. *Philips Tech. Rev.*, 20:220–224, 1958.

[85] H. K. Min, B. Sahu, S. K. Banerjee, and A. H. MacDonald. Ab initio theory of gate induced gaps in graphene bilayers. *Phys. Rev. B*, 75:155115, 2007.

[86] L.A. Falkovsky. Gate-tunable bandgap in bilayer graphene. *Journal of Experimental and Theoretical Physics*, 110(2):319–324, 2010.

[87] T. Ohta, A. Bostwick, T. Seyller, K. Horn, and E. Rotenberg. Controlling the electronic structure of bilayer graphene. *Science*, 313(5789):951–954, 2006.

[88] Y. Zhang, T.-T. Tang, C. Girit, Z. Hao, M. C. Martin, A. Zettl, M. F. Crommie, Y. R. Shen, and F. Wang. Direct observation of a widely tunable bandgap in bilayer graphene. *Nature*, 459(7248):820–823, 2009.

[89] Kin Fai Mak, Chun Hung Lui, Jie Shan, and Tony F. Heinz. Observation of an electric-field-induced band gap in bilayer graphene by infrared spectroscopy. *Phys. Rev. Lett.*, 102:256405, 2009.

[90] Z. Q. Li, E. A. Henriksen, Z. Jiang, Z. Hao, M. C. Martin, P. Kim, H. L. Stormer, and D. N. Basov. Band structure asymmetry of bilayer graphene revealed by infrared spectroscopy. *Phys. Rev. Lett.*, 102:037403, 2009.

[91] K. S. Novoselov. Graphene: Cracking bilayers. *Nat. Phys.*, 5(12):862–863, 2009.

[92] U. Klaß, W. Dietsche, K. Klitzing, and K. Ploog. Imaging of the dissipation in quantum-Hall-effect experiments. *Zeitschrift für Physik B Condensed Matter*, 82(3):351–354, 1991.

[93] G. Nachtwei. Breakdown of the quantum Hall effect. *Physica E: Low-dimensional Systems and Nanostructures*, 4(2):79–101, 1999.

[94] B. E. Feldman, J. Martin, and A. Yacoby. Broken-symmetry states and divergent resistance in suspended bilayer graphene. *Nat. Phys.*, 5:889–893, 2009.

[95] Y. Zhao. Symmetry breaking in the zero-energy Landau level in bilayer graphene. *Phys. Rev. Lett.*, 104:066801, 2010.

[96] Y. Zhang, Z. Jiang, J. P. Small, M. S. Purewal, Y.-W. Tan, M. Fazlollahi, J. D. Chudow, J. A. Jaszczak, H. L. Stormer, and P. Kim. Landau-level splitting in graphene in high magnetic fields. *Phys. Rev. Lett.*, 96:136806, 2006.

[97] Z. Jiang, Y. Zhang, H. L. Stormer, and P. Kim. Quantum Hall states near the charge-neutral Dirac point in graphene. *Phys. Rev. Lett.*, 99:106802, 2007.

[98] A. J. M. Giesbers, L. A. Ponomarenko, K. S. Novoselov, A. K. Geim, M. I. Katsnelson, J. C. Maan, and U. Zeitler. Gap opening in the zeroth Landau level of graphene. *Phys. Rev. B*, 80:201403, 2009.

[99] Edward McCann and Vladimir I. Fal'ko. Landau-level degeneracy and quantum Hall effect in a graphite bilayer. *Phys. Rev. Lett.*, 96:086805, 2006.

[100] Y. Barlas, R. Côté, K. Nomura, and A. H. MacDonald. Intra-Landau-level cyclotron resonance in bilayer graphene. *Phys. Rev. Lett.*, 101:097601, 2008.

[101] R. Nandkishore and L. S. Levitov. Flavor symmetry and competing orders in bilayer graphene. *http://arxiv.org/abs/1002.1966*, 2010.

[102] M. Ezawa. Intrinsic Zeeman effect in graphene. *J. Phys. Soc. Jpn.*, 76(9):094701, 2007.

[103] E. V. Gorbar, V. P. Gusynin, and V. A. Miransky. Dynamics and phase diagram of the $\nu = 0$ quantum Hall state in bilayer graphene. *Phys. Rev. B*, 81:155451, 2010.

[104] P. Maher, C. R. Dean, A. F. Young, T. Taniguchi, K. Watanabe, K. L. Shepard, J. Hone, and P. Kim. Evidence for a spin phase transition at charge neutrality in bilayer graphene. *Nat. Phys.*, 9(3):154–158, 2013.

[105] S. Raghu, X.-L. Qi, C. Honerkamp, and S.-C. Zhang. Topological Mott insulators. *Phys. Rev. Lett.*, 100:156401, 2008.

[106] Hongki Min, Giovanni Borghi, Marco Polini, and A. H. MacDonald. Pseudospin magnetism in graphene. *Phys. Rev. B*, 77:041407, 2008.

[107] Rahul Nandkishore and Leonid Levitov. Quantum anomalous Hall state in bilayer graphene. *Phys. Rev. B*, 82:115124, 2010.

[108] F. Zhang, H. Min, M. Polini, and A. H. MacDonald. Spontaneous inversion symmetry breaking in graphene bilayers. *Phys. Rev. B*, 81:041402, 2010.

[109] O. Vafek and K. Yang. Many-body instability of Coulomb interacting bilayer graphene: Renormalization group approach. *Phys. Rev. B*, 81:041401, 2010.

[110] Y. Lemonik, I. L. Aleiner, C. Toke, and V. I. Fal'ko. Spontaneous symmetry breaking and Lifshitz transition in bilayer graphene. *Phys. Rev. B*, 82:201408, 2010.

[111] Rahul Nandkishore and Leonid Levitov. Polar kerr effect and time reversal symmetry breaking in bilayer graphene. *Phys. Rev. Lett.*, 107:097402, 2011.

[112] Mitsutaka Fujita, Katsunori Wakabayashi, Kyoko Nakada, and Koichi Kusakabe. Peculiar localized state at zigzag graphite edge. *J. Phys. Soc. Jpn.*, 65:1920–1923, 1996.

[113] M. Ezawa. Peculiar width dependence of the electronic properties of carbon nanoribbons. *Phys. Rev. B*, 73:045432, 2006.

[114] J. A. Fürst, J. G. Pedersen, C. Flindt, N. A. Mortensen, M. Brandbyge, T. G. Pedersen, and A.-P. Jauho. Electronic properties of graphene antidot lattices. *New J. Phys.*, 11:095020, 2009.

[115] M. Vanević, V. M. Stojanović, and M. Kindermann. Character of electronic states in graphene antidot lattices: Flat bands and spatial localization. *Phys. Rev. B*, 80:045410, 2009.

[116] H. Jippo, M. Ohfuchi, and C. Kaneta. Theoretical study on electron transport properties of graphene sheets with two- and one-dimensional periodic nanoholes. *Phys. Rev. B*, 84:075467, 2011.

[117] M. Y. Han, B. Özyilmaz, Y. Zhang, and P. Kim. Energy band-gap engineering of graphene nanoribbons. *Phys. Rev. Lett.*, 98:206805, 2007.

[118] X. Wang, Y. Ouyang, X. Li, H. Wang, J. Guo, and H. Dai. Room-temperature all-semiconducting sub-10-nm graphene nanoribbon field-effect transistors. *Phys. Rev. Lett.*, 100:206803, 2008.

[119] J. Bai, R. Cheng, F. Xiu, L. Liao, M. Wang, A. Shailos, K. L. Wang, Y. Huang, and X. Duan. Very large magnetoresistance in graphene nanoribbons. *Nat. Nano.*, 5(9):655–659, 2010.

[120] F. Sols, F. Guinea, and A. H. Castro Neto. Coulomb blockade in graphene nanoribbons. *Phys. Rev. Lett.*, 99:166803, 2007.

[121] B. I. Shklovskii and A. L. Efros. *Electronic properties of doped semiconductors.* Springer-Verlag, Berlin, 1984.

[122] S. J. Lee, J. B. Ketterson, and N. Trivedi. Metal-insulator transition in quasi-two-dimensional Mo-C films. *Phys. Rev. B*, 46:12695–12700, 1992.

[123] R. Rosenbaum. Crossover from Mott to Efros-Shklovskii variable-range-hopping conductivity in In_xO_y films. *Phys. Rev. B*, 44:3599–3603, 1991.

[124] K. W. K. Shung. Dielectric function and plasmon structure of stage-1 intercalated graphite. *Phys. Rev. B*, 34:979–993, 1986.

[125] F. Withers, S. Russo, M. Dubois, and M. F. Craciun. Tuning the electronic transport properties of graphene through functionalisation with fluorine. *Nanoscale Research Letters*, 6:526, 2011.

[126] C. J. Adkins. Conduction in granular metals-variable-range hopping in a Coulomb gap? *Journal of Physics: Condensed Matter*, 1(7):1253, 1989.

[127] B. Kramer and A. MacKinnon. Localization: theory and experiment. *Reports on Progress in Physics*, 56(12):1469, 1993.

[128] J. Jobst, D. Waldmann, I. V. Gornyi, A. D. Mirlin, and H. B. Weber. Electron-electron interaction in the magnetoresistance of graphene. *Phys. Rev. Lett.*, 108:106601, 2012.

[129] S. V. Morozov, K. S. Novoselov, M. I. Katsnelson, F. Schedin, L. A. Ponomarenko, D. Jiang, and A. K. Geim. Strong suppression of weak localization in graphene. *Phys. Rev. Lett.*, 97:016801, 2006.

[130] S. Cho and M. S. Fuhrer. Charge transport and inhomogeneity near the minimum conductivity point in graphene. *Phys. Rev. B*, 77:081402(R), 2008.

[131] Ernesto Medina and Mehran Kardar. Quantum interference effects for strongly localized electrons. *Phys. Rev. B*, 46:9984–10006, 1992.

[132] B. L. Altshuler, D. Khmel'nitzkii, A. I. Larkin, and P. A. Lee. Magnetoresistance and Hall effect in a disordered two-dimensional electron gas. *Phys. Rev. B*, 22:5142–5153, 1980.

[133] U. Sivan, O. Entin-Wohlman, and Y. Imry. Orbital magnetoconductance in the variable-range – hopping regime. *Phys. Rev. Lett.*, 60:1566–1569, 1988.

[134] W. Schirmacher. Quantum-interference magnetoconductivity in the variable-range-hopping regime. *Phys. Rev. B*, 41:2461–2468, 1990.

[135] S. Russo, J. B. Oostinga, D. Wehenkel, H. B. Heersche, S. S. Sobhani, L. M. K. Vandersypen, and A. F. Morpurgo. Observation of Aharonov-Bohm conductance oscillations in a graphene ring. *Phys. Rev. B*, 77:085413, 2008.

[136] T. Shen, Y. Q. Wu, M. A. Capano, L. P. Rokhinson, L. W. Engel, and P. D. Ye. Magnetoconductance oscillations in graphene antidot arrays. *Applied Physics Letters*, 93(12):122102, 2008.

[137] D. Weiss, M. L. Roukes, A. Menschig, P. Grambow, K. von Klitzing, and G. Weimann. Electron pinball and commensurate orbits in a periodic array of scatterers. *Phys. Rev. Lett.*, 66:2790–2793, 1991.

[138] V. L. Nguyen. Crossovers in two-dimensional variable range hopping. *Physics Letters A*, 207(6):379–384, 1995.

[139] B. Capoen, G. Biskupski, and A. Briggs. Crossover phenomenon for variable range hopping conduction in strong magnetic field. *Solid State Communications*, 113(3):135–139, 1999.

[140] M. Iqbal, J. Galibert, J. Léotin, S. Waffenschmidt, and H. v. Löhneysen. Magnetic-field induced crossover from Efros-Shklovskii to Mott variable range hopping in Si:(P, B). *Philosophical Magazine Part B*, 79(10):1591–1601, 1999.

[141] V. I. Nguyen, B. Z. Spivak, and B. I. Shlovskii. Aharanov-Bohm oscillations with normal and superconductive flux-quanta in hopping conduction. *Sov. Phys. JEPT*, 62:1021, 1985.

[142] D. Weiss, K. Richter, A. Menschig, R. Bergmann, H. Schweizer, K. von Klitzing, and G. Weimann. Quantized periodic orbits in large antidot arrays. *Phys. Rev. Lett.*, 70:4118–4121, 1993.

[143] J. G. Checkelsky, L. Li, and N. P. Ong. Zero-energy state in graphene in a high magnetic field. *Phys. Rev. Lett.*, 100:206801, 2008.

[144] M. O. Goerbig, R. Moessner, and B. Douçot. Electron interactions in graphene in a strong magnetic field. *Phys. Rev. B*, 74:161407, 2006.

[145] D. A. Abanin, K. S. Novoselov, U. Zeitler, P. A. Lee, A. K. Geim, and L. S. Levitov. Dissipative quantum Hall effect in graphene near the Dirac point. *Phys. Rev. Lett.*, 98:196806, 2007.

[146] E. Shimshoni, H. A. Fertig, and G. Venketeswara Pai. Onset of an insulating zero-plateau quantum Hall state in graphene. *Phys. Rev. Lett.*, 102:206408, 2009.

[147] A. F. Young, C. R. Dean, L. Wang, H. Ren, P. Cadden-Zimansky, K. Watanabe, T. Taniguchi, J. Hone, K. L. Shepard, and P. Kim. Spin and valley quantum Hall ferromagnetism in graphene. *Nat. Phys.*, 8(7):550–556, 2012.

[148] L. Jiang, Y. Zheng, H. Li, and H. Shen. Magneto-transport properties of gapped graphene. *Nanotechnology*, 21(14):145703, 2010.

[149] J. G. Pedersen and T. G. Pedersen. Tight-binding study of the magneto-optical properties of gapped graphene. *Phys. Rev. B*, 84:115424, 2011.

[150] J. G. Pedersen and T. G. Pedersen. Dirac model of an isolated graphene antidot in a magnetic field. *Phys. Rev. B*, 85:035413, 2012.

[151] J. G. Checkelsky, L. Li, and N. P. Ong. Divergent resistance at the Dirac point in graphene: Evidence for a transition in a high magnetic field. *Phys. Rev. B*, 79:115434, 2009.

[152] S. Wiedmann, H. J. van Elferen, E. V. Kurganova, M. I. Katsnelson, A. J. M. Giesbers, A. Veligura, B. J. van Wees, R. V. Gorbachev, K. S. Novoselov, J. C. Maan, and U. Zeitler. Coexistence of electron and hole transport in graphene. *Phys. Rev. B*, 84:115314, 2011.

[153] K. Seeger. *Semiconductor Physics, an Introduction.* Springer, Berlin, 1997.

[154] S. O. Kasap. Hall effect in semiconductors. Electronic Booklet, 2001.

[155] R. Kubo. A general expression for the conductivity tensor. *Canadian Journal of Physics*, 34:1274–1277, 1956.

[156] D. A. Greenwood. The Boltzmann equation in the theory of electrical conduction in metals. *Proceedings of the Physical Society*, 71(4):585, 1958.

[157] P. Streda. Theory of quantised Hall conductivity in two dimensions. *Journal of Physics C: Solid State Physics*, 15(22):L717, 1982.

[158] Z. Jiang, Y. Zhang, H. L. Stormer, and P. Kim. Quantum Hall states near the charge-neutral Dirac point in graphene. *Phys. Rev. Lett.*, 99:106802, 2007.

[159] F. Ouyang, S. Peng, Z. Liu, and Z. Liu. Bandgap opening in graphene antidot lattices: The missing half. *ACS Nano*, 5(5):4023–4030, 2011.

[160] A. Behnam, A.S. Lyons, M.H. Bae, E.K. Chow, S. Islam, C.M. Neumann, and E. Pop. Transport in nanoribbon interconnects obtained from graphene grown by chemical vapor deposition. *Nano Lett.*, 12:4424, 2012.

[161] A. J. M. Giesbers, U. Zeitler, M. I. Katsnelson, L. A. Ponomarenko, T.M. Mohiuddin, and J. C. Maan. Quantum-Hall activation gaps in graphene. *Phys. Rev. Lett.*, 99:206803, 2007.

[162] C. H. Yang, F. M. Peeters, and W. Xu. Landau-level broadening due to electron-impurity interaction in graphene in strong magnetic fields. *Phys. Rev. B*, 82:075401, 2010.

[163] E. V. Kurganova, H. J. van Elferen, A. McCollam, L. A. Ponomarenko, K. S. Novoselov, A. Veligura, B. J. van Wees, J. C. Maan, and U. Zeitler. Spin splitting in graphene studied by means of tilted magnetic-field experiments. *Phys. Rev. B*, 84:121407, 2011.

[164] T. Englert, D.C. Tsui, A.C. Gossard, and Ch. Uihlein. g-factor enhancement in the 2D electron gas in gaas/algaas heterojunctions. *Surface Science*, 113:295–300, 1982.

[165] R. J. Nicholas, R. J. Haug, K. v. Klitzing, and G. Weimann. Exchange enhancement of the spin splitting in a GaAs-$Ga_xAl_{1-x}As$ heterojunction. *Phys. Rev. B*, 37:1294–1302, 1988.

[166] C. Dean, A.F. Young, L. Wang, I. Meric, G.-H. Lee, K. Watanabe, T. Taniguchi, K. Shepard, P. Kim, and J. Hone. Graphene based heterostructures. *Solid State Communications*, 152:1275–1282, 2012.

[167] L. Britnell, R. V. Gorbachev, R. Jalil, B. D. Belle, F. Schedin, A. Mishchenko, T. Georgiou, M. I. Katsnelson, L. Eaves, S. V. Morozov, N. M. R. Peres, J. Leist, A. K. Geim, K. S. Novoselov, and L. A. Ponomarenko. Field-effect tunneling transistor based on vertical graphene heterostructures. *Science*, 335(6071):947–950, 2012.

[168] J. Cai, P. Ruffieux, R. Jaafar, M. Bieri, T. Braun, S. Blankenburg, M. Muoth, A. P. Seitsonen, M. Saleh, X. Feng, K. Mullen, and R. Fasel. Atomically precise bottom-up fabrication of graphene nanoribbons. *Nature*, 466:470–473, 2010.

[169] N. Tombros, C. Jozsa, M. Popinciuc, H. T. Jonkman, and B. J. van Wees. Electronic spin transport and spin precession in single graphene layers at room temperature. *Nature*, 448(7153):571–574, 2007.

[170] A. Rycerz, J. Tworzydlo, and C. W. J. Beenakker. Valley filter and valley valve in graphene. *Nat. Phys.*, 3(3):172–175, 2007.

[171] J. L. Garcia-Pomar, A. Cortijo, and M. Nieto-Vesperinas. Fully valley-polarized electron beams in graphene. *Phys. Rev. Lett.*, 100:236801, 2008.

[172] R. Balog, B. Jorgensen, L. Nilsson, M. Andersen, E. Rienks, M. Bianchi, M. Fanetti, E. Laegsgaard, A. Baraldi, S. Lizzit, Z. Sljivancanin, F. Besenbacher, B. Hammer, T. G. Pedersen, P. Hofmann, and L. Hornekaer. Bandgap opening in graphene induced by patterned hydrogen adsorption. *Nat. Mater.*, 9(4):315–319, 2010.

[173] H. Gao, L. Wang, J. Zhao, F. Ding, and J. Lu. Band gap tuning of hydrogenated graphene: H coverage and configuration dependence. *The Journal of Physical Chemistry C*, 115(8):3236–3242, 2011.

[174] Bernard R. Matis, James S. Burgess, Felipe A. Bulat, Adam L. Friedman, Brian H. Houston, and Jeffrey W. Baldwin. Surface doping and band gap tunability in hydrogenated graphene. *ACS Nano*, 6(1):17–22, 2012.

[175] J. Zhou, Q. Wang, Q. Sun, X. S. Chen, Y. Kawazoe, and P. Jena. Ferromagnetism in semihydrogenated graphene sheet. *Nano Letters*, 9(11):3867–3870, 2009. PMID: 19719081.

[176] W. Norimatsu and M. Kusunoki. Formation process of graphene on SiC (0001). *Physica E: Low-dimensional Systems and Nanostructures*, 42(4):691–694, 2010.

[177] S. W. Poon, W. Chen, A. T. S. Wee, and E. S. Tok. Growth dynamics and kinetics of monolayer and multilayer graphene on a 6H-SiC(0001) substrate. *Phys. Chem. Chem. Phys.*, 12:13522–13533, 2010.

[178] G. M. Rutter, N. P. Guisinger, J. N. Crain, E. A. A. Jarvis, M. D. Stiles, T. Li, P. N. First, and J. A. Stroscio. Imaging the interface of epitaxial graphene with silicon carbide via scanning tunneling microscopy. *Phys. Rev. B*, 76:235416, 2007.

[179] J. B. Hannon and R. M. Tromp. Pit formation during graphene synthesis on SiC (0001): In situ electron microscopy. *Phys. Rev. B*, 77:241404, 2008.

[180] J. Hass, R. Feng, J. E. Millán-Otoya, X. Li, M. Sprinkle, P. N. First, W. A. de Heer, E. H. Conrad, and C. Berger. Structural properties of the multilayer graphene/4H-SiC(000$\bar{1}$) system as determined by surface x-ray diffraction. *Phys. Rev. B*, 75:214109, 2007.

[181] S. Ryu, M. Y. Han, J. Maultzsch, T. F. Heinz, P. Kim, M. L. Steigerwald, and L. E. Brus. Reversible basal plane hydrogenation of graphene. *Nano Letters*, 8(12):4597–4602, 2008.

[182] Zhiqiang Luo, Ting Yu, Ki-jeong Kim, Zhenhua Ni, Yumeng You, Sanhua Lim, Zexiang Shen, Shanzhong Wang, and Jianyi Lin. Thickness-dependent reversible hydrogenation of graphene layers. *ACS Nano*, 3(7):1781–1788, 2009.

[183] E. J. H. Lee, K. Balasubramanian, R. T. Weitz, M. Burghard, and K. Kern. Contact and edge effects in graphene devices. *Nat. Nano.*, 3(8):486–490, 2008.

[184] G. Nazin, Y. Zhang, L. Zhang, E. Sutter, and P. Sutter. Visualization of charge transport through Landau levels in graphene. *Nat. Phys.*, 6(11):870–874, 2010.

[185] N. M. Gabor, J. C. W. Song, Q. Ma, N. L. Nair, T. Taychatanapat, K. Watanabe, T. Taniguchi, L. S. Levitov, and P. Jarillo-Herrero. Hot carrier-assisted intrinsic photoresponse in graphene. *Science*, 334(6056):648–652, 2011.

[186] Oxford Instruments. *Operator's Handbook - Superconducting Magnet System*, 2012.

[187] Oxford Instruments. *MMS v405 Operators Handbook M089*, 2012.

Curriculum Vitae

Personal Information

Date of birth	16.04.1984
Place of birth	Göppingen, Germany
Nationality	German

Scientific Experience

2010-2013 **PhD Thesis**, Max-Planck-Institute for Solid State Research, Stuttgart, Germany, Nanoscale Science department, Prof. Klaus Kern

Magnetotransport in Graphene: Gap-Opening and Interaction Effects

2012 **Supervisor**, DAAD RISE Program, Stuttgart, Germany
Supervisor for a Canadian Bachelor student in an Internship Project at the Max-Planck-Institute for Solid State Research

2010 **Visiting Researcher**, Harvard University, Cambridge, USA
Physics department, Prof. Amir Yacoby

2008-2009 **Diploma Thesis**, Max-Planck-Institute for Solid State Research, Stuttgart, Germany, Nanoscale Science department, Prof. Klaus Kern

Carbon-Based Photovoltaic Nanostructures

Education

2010-2013 **PhD in Physics**, École Polytechnique Fédérale de Lausanne, Lausanne, Switzerland

2007-2008 **Exchange Year**, University of Adelaide, Adelaide, Australia

2003-2009 **Diploma in Physics**, University of Stuttgart, Stuttgart, Germany

2003 **Abitur**, Helfensteingymnasium, Geislingen an der Steige, Germany

Publications

- E. C. Peters, E. J. H. Lee, M. Burghard and K. Kern
  "Gate dependent photocurrents at a graphene p-n junction"
  Appl. Phys. Lett. **97**, 193102 (2010)

- A. J. M. Giesbers, E. C. Peters, M. Burghard and K. Kern
  "Charge transport gap in graphene antidot lattices"
  Phys. Rev. B **86**, 045445 (2012)

- E. C. Peters, A. J. M. Giesbers and M. Burghard
  "Variable range hopping in graphene antidot lattices"
  Phys. Status Solidi B **249**, 2522 (2012)

- E. C. Peters, A. J. M. Giesbers, U. Zeitler, M. Burghard and K. Kern
  "Valley-polarized massive charge carriers in gapped graphene"
  Phys. Rev. B **87**, 201403(R) (2013)

- A. J. M. Giesbers, K. Uhlířová, M. Konečný, E. C. Peters,
  M. Burghard, J. Aarts and C.F.J. Flipse
  "Interface induced room-temperature ferromagnetism
  in hydrogenated epitaxial graphene"
  http://arxiv.org/abs/1305.3158 (2013)

Acknowledgments

Many people contributed to the success of this thesis. I am thankful to

Prof. Klaus Kern for giving me the opportunity to work as a PhD student in his department at the Max Planck Institute (MPI) for Solid State Research in Stuttgart as well as in collaboration projects in the US and the Netherlands.

Dr. Marko Burghard, my direct advisor, for supervising my work, for his advice, many fruitful discussions and the freedom I could enjoy during my work.

Prof. Amir Yacoby as well as the group and especially the graphene team Dr. Jens Martin, Dr. Thomas Weitz, Ben Feldman and Monica Allen for their support during my time in the Yacoby group.

Dr. Jos Giesbers for sharing his knowledge, his advice and support at the MPI as well as during measurements at the high field magnet laboratory (HFML) in Nijmegen and in later collaborations on epitaxial graphene.

Dr. Uli Zeitler for his support during the measurements at the HFML.

Alexander Hoyer for sharing the challenging work of making a new setup work and eliminating bucks that occur or reoccur.

Martin Siemers for his practical support with any electronic parts and Dr. Markus Ternes for explaining the theory behind it.

The Kern group technicians Peter Andler, Wolfgang Stiepany and Marko Memmler for their help with any mechanical parts.

The many MPI service groups such as the crystal cutting service, the low temperature service, the mechanical workshop, the electronics service, the clean room team, especially Ulrike Waizmann, Marion Hagel, Thomas Reindl, Achim Güth and the IT group.

Kevin Grykuliak for the internship project he did under my supervision.

The former and present Molecular Electronics (or also Quantum Materials) group members, especially Dr. Bo Gao, Dr. Amit Kumar, Dr. Ravi Sundaram, Dr. Adarsh Sagar, Dr. Eduardo Lee, Dr. Ulrich Stützel, Dr. Thomas Dufaux, Pascal Gehring, Kristina Vaklinova and Roberto Urcuyo for the great working atmosphere.

All of my other fellow PhD students and coworkers in the Kern group but also many others from the other Institute groups for a good time at the MPI.

Finally I also want to thank my family and Roman for their unconditional continuous support.